IMAGE: A MAP OF THE STARS OF THE ORION CONSTELLATION

Print ISSN: 2631-8490 Online ISSN: 2631-8504

JournalPreview

London Journal of Research in Science: Natural and Formal
Volume 20 | Issue 3 | Compilation 1.0

London Journals Press

LONDON JOURANALS OF RESEARCH IN SCIENCE: NATURAL AND FORMAL

Journal Content
In this Issue

London Journals Press

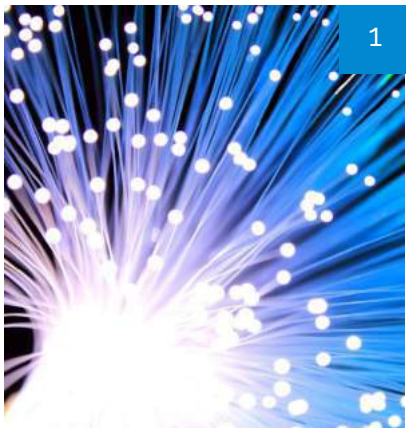

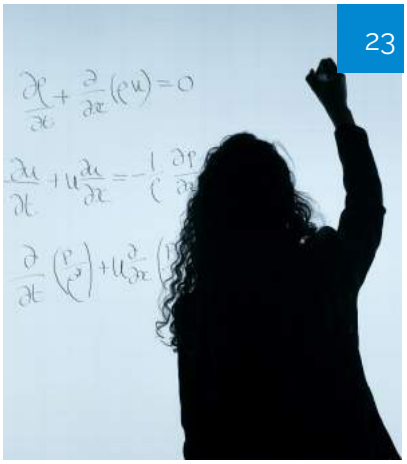

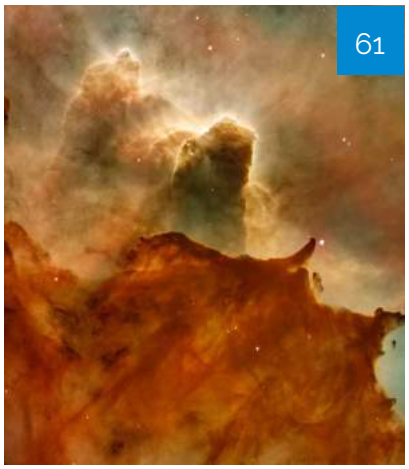

Dichotomy Between Null Results from all Interferometer Experiments versus Special Relativity Expectations

Steven D. Deines

ABSTRACT

The fundamental principle of physics is that all observers of an event must have identical results, especially when the recorded data are transformed to a common inertial frame. The Michelson-Morley experiment demonstrates contradictions with length contraction when three or more independent inertial observers concurrently record the output. Length contraction has never been observed directly despite current technological precision. Special relativity does not explain the constant output of the Michelson-Morley and Kennedy-Thorndike interferometers, since Earth's rotation causes unequal changing velocities for both arms. Displacements, instead of time intervals, for the split beams are analyzed when the interferometer is stationary and moving at a constant velocity. This paper reveals that any interferometer with equal or unequal arms can neither prove nor disprove the existence of a hypothetical medium for light transmission. All interferometer experiments indicate light velocity obeys vector velocity addition involving moving light sources. This property of light explains how measurements of light speed in any moving laboratory are precisely identical when sources and detectors are fixed relative to each other. The universal speed of light is an excellent approximation due to high speed, but not an exact constant when light sources and observers move independently. Many physical concepts will require reexamination.

Keywords: length contraction, time dilation, light speed, michelson-morley experiment, kennedy-thorndike experiment.

Classification: FOR Code: 040401

Language: English

London Journals Press

LJP Copyright ID: 925621
Print ISSN: 2631-8490
Online ISSN: 2631-8504

London Journal of Research in Science: Natural and Formal

Volume 20 | Issue 3 | Compilation 1.0

Dichotomy Between Null Results from all Interferometer Experiments versus Special Relativity Expectations

Steven D. Deines

ABSTRACT

The fundamental principle of physics is that all observers of an event must have identical results, especially when the recorded data are transformed to a common inertial frame. The Michelson-Morley experiment demonstrates contradictions with length contraction when three or more independent inertial observers concurrently record the output. Length contraction has never been observed directly despite current technological precision. Special relativity does not explain the constant output of the Michelson-Morley and Kennedy-Thorndike interferometers, since Earth's rotation causes unequal changing velocities for both arms. Displacements, instead of time intervals, for the split beams are analyzed when the interferometer is stationary and moving at a constant velocity. This paper reveals that any interferometer with equal or unequal arms can neither prove nor disprove the existence of a hypothetical medium for light transmission. All interferometer experiments indicate light velocity obeys vector velocity addition involving moving light sources. This property of light explains how measurements of light speed in any moving laboratory are precisely identical when sources and detectors are fixed relative to each other. The universal speed of light is an excellent approximation due to high speed, but not an exact constant when light sources and observers move independently. Many physical concepts will require reexamination.

Keywords: length contraction, time dilation, light speed, michelson-morley experiment, kennedy-thorndike experiment.

Author: Donatech Corporation, Inc., Fairfield, Iowa USA.

I. BACKGROUND

Hippolyte Fizeau [1, 2] measured the speed of light through moving water and analyzed it theoretically using the concepts of vector addition with c + v and c - v, where c is the speed of light in a vacuum and v is the speed of the moving water. Fizeau used a special interferometer to compare the frequency shift by combining two light beams that went through moving water in different directions. Fizeau's theory grossly overestimated the measured shift. Albert Michelson and Edward Morley replicated Fizeau's water experiment with a more accurate setup and obtained Fizeau's same residual nonzero result. They concluded, "The result of this work is therefore that the result announced by Fizeau is essentially correct; and that *the luminiferous ether is entirely unaffected by the motion of the matter which it permeates*." (original italics)[3] In 1881, Michelson designed and demonstrated an interferometer to split a light beam into two perpendicular beams that traversed equal lengths and that recombined into one output light beam [4]. The analysis was based on Fizeau's theory and predicted that the motion of the interferometer due to Earth's orbital motion alone should cause the light beams to arrive at the recombination point at different times, which would produce destructive interference. It was hoped that rotating the interferometer would align one axis with Earth's orbital velocity and produce a maximum destructive interference to determine the orbital velocity of the laboratory through the hypothetical medium for transmitting an

London Journal of Research in Science: Natural and Formal

electromagnetic wave as expected in Maxwell's equations. With the collaboration of Morley, the updated and much larger interferometer was tested in 1886, and null results were published later in 1889 while using Fizeau's original theory for comparison [5, 6].

Kennedy and Thorndike [7] modified the Michelson-Morley interferometer by making one arm shorter than the other, so that destructive interference was produced. The Kennedy-Thorndike setup photographed interference rings, which were virtually unchanging. The outcome was a static interference, which did not change in any orientation of the apparatus over months of monitoring.

Retests of both interferometer experiments using more precise equipment, laser light sources, and atomic clocks produced the same null results. Jaseva et al. published in 1964 that the frequency shift for the Michelson-Morley test is less than 1/1000 of the effect predicted with the assumption that light has a fixed velocity with respect to the assumed medium [8]. Hils, Deiter and Hall retested the Kennedy-Thorndike experiment in 1990 with a 300-fold improvement and found no variation of destructive interference above $2x10^{-13}$ [9]. Another recent retest of the Michelson-Morley interferometer is the Laser Interferometer Gravitational-Wave Observatory (LIGO).

II. ORIGINAL THEORY APPLIED IN THE EQUAL-ARM INTERFEROMETER

In the laboratory frame, the Michelson-Morley setup [6] has the basic form in Figure 1, where the half-silvered (i.e., partially coated) mirror at A splits the laser beam into two beams, (partial transmission and partial reflection), each reflected off Mirrors B and C that are equally distant from A.

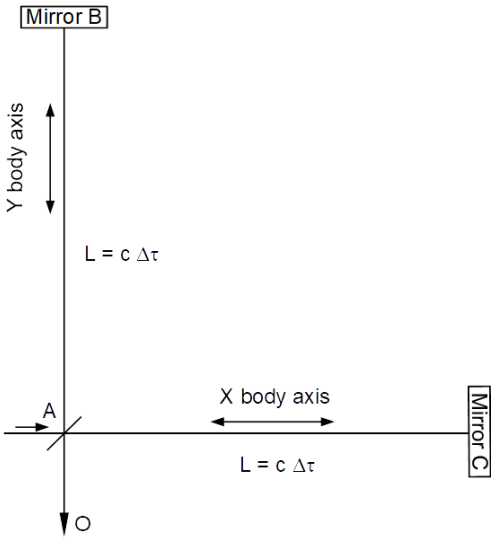

Figure 1: Michelson-Morley apparatus in inertial lab frame.

The reflected beams recombine at A, and output is monitored at O. With equal lengths L=AB=AC, the combined beams produce constructive interference, which indicates the split beams arrive at A at the same time. Except for multiple wavelengths, if the lengths AB or AC changed (as done in the Kennedy-Thorndike version), making arrival times different, destructive interference would have been expected. This was the classic test for the theoretical ether as the medium to propagate light waves. Figure 2 depicts the apparatus moving relative to an external observer, which simulates the apparatus moving at a constant velocity parallel to one arm relative to an absolute, stationary frame.

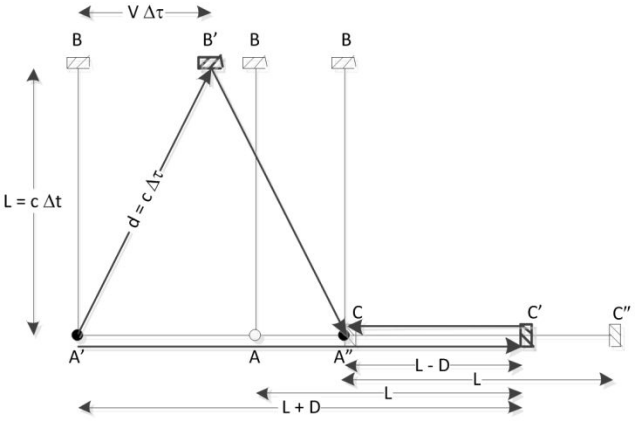

Figure 2: Moving Michelson-Morley experiment relative to inertial observer.

Here, A′ is the point where the beam is split into two beams by Mirror A. One beam travels from A′ to Mirror B at B′, reflects back to Mirror A, and recombines at point A″. A second beam moves from A′ to Mirror C at C′, is reflected to Mirror A, and arrives at point A″. The entire apparatus travels at a uniform velocity v along the X-axis during the test, which is a valid assumption when c » v. For clarity in Figure 2, the output through O is not shown, and the arrows A′C′ and C′A″ are displaced laterally apart. Let Observer 1 be fixed in an inertial frame while the apparatus is moving uniformly to the right at velocity v, and the Laboratory Observer is fixed relative to the apparatus, so the Laboratory Observer has a velocity v compared to Observer 1. The Laboratory Observer would witness the apparatus to operate as in Figure 1, while Observer 1 perceives the apparatus as in Figure 2.

If the apparatus is at rest relative to Observer 1, then 2L = c 2Δt for c the speed of light and Δt for the time interval for light to traverse the distance L. If the apparatus is modified to count intervals of 2Δt, a proper timescale for Observer 1 is defined. For light to travel from A′ to B′ to A″, 2d = c 2Δτ, where Δτ > Δt, since d > L. Letting v Δτ be the distance the moving apparatus is displaced to the right until the beam from A′ touches B′, one gets the following geometric relation between Δt and Δτ.

$$d^2 = (v\,\Delta\tau)^2 + L^2 = (c\,\Delta\tau)^2 = (v\,\Delta\tau)^2 + (c\,\Delta t)^2 = (c\,\Delta\tau)^2$$

$$\Delta\tau = \frac{\Delta t}{\sqrt{1-\frac{v^2}{c^2}}} = \frac{L/c}{\sqrt{1-\frac{v^2}{c^2}}} \qquad (1)$$

If one defines a master time as counting the time span between round trips of light bouncing between Mirror A and Mirror B for either observer, 2Δt is the time unit for Observer 1's time scale, and 2Δτ is the Observer 1's perceived time unit for the Laboratory Observer's proper timescale. Equation (1) is the time dilation equation [6, p. 1200-1203] from special relativity that Observer 1 perceives between Δt and Δτ.

The time interval for light to traverse from A′ to C′ to A″ is assumed longer than Δt in Observer 1's frame. Let D be the distance the apparatus moves until light from A′ touches Mirror C at C′. Light along the X-axis will have traveled L+D to Mirror C. Then, the reflected light will travel L–D back to A″ for a total distance of 2L for the two traverses in the laboratory frame , and

$$c\,\Delta T_2 = L - D \text{ or } \Delta T_2 = \frac{L-D}{c} \quad . \qquad (2)$$

Replace D with v ΔT in the external frame.

$$c\,\Delta T_1 = L + v\,\Delta T_1 \text{ or } \Delta T_1 = \frac{L}{c-v} \qquad (3)$$

$$c\,\Delta T_2 = L - v\,\Delta T_2 \text{ or } \Delta T_2 = \frac{L}{c+v} \qquad (4)$$

$$\Delta T = \Delta T_1 + \Delta T_2 = \frac{L}{c-v} + \frac{L}{c+v} = \frac{L(c+v)+L(c-v)}{c^2-v^2} = \frac{2L/c}{1-\frac{v^2}{c^2}} \qquad (5)$$

Equation (5) implies that the traversing beam parallel to the X-axis takes $1/(1-v^2/c^2)^{0.5}$ longer than the other beam arriving at A″ by (1). The relativistic compensation by length contraction replaces L in (5) with $L(1-v^2/c^2)^{0.5}$, so that the resulting ΔT now equals Δτ in (1) when 2L/c = ΔT. Length contraction is the standard explanation that the parallel split beam must travel a shorter distance so that the merged light beams are synchronous.

Virtually all velocities of the interferometer in the XY plane will not be parallel solely to either the X- or Y-axis, but it is the vector sum of V_x and V_y. Start with L = L_x = L_y initially in the stationary frame. Define $1/(1-v^2/c^2)^{0.5}$ = γ. The component velocity $\mathbf{V_x}$ will cause $L_x = L(1-\frac{V_x^2}{c^2})^{0.5}$ = L/γ < L via length contraction in the laboratory frame. Apply the component velocity $\mathbf{V_y}$ to the interferometer. Length contraction should shorten the Y-axis arm to cause $L_Y = L(1-\frac{V_y^2}{c^2})^{0.5}$ = L/γ < L, but the perpendicular arm is not at the required length L to cause constructive interference, but the shorter arm of L_X. To preserve the null result in the ratio of $\Delta T_x/\Delta T_y$, the Y-axis arm must be shorter by a multiplicative factor of $(1-\frac{V_y^2}{c^2})^{0.5}$. In the original explanation for the null result as given above, the

$\mathbf{V_X}$ component of velocity will cause length contraction only in the X-axis and $\mathbf{V_Y}$ only in the Y-axis. Generally, length contraction affects both arms when **V** is not relegated to being parallel to either the X- or Y-axis. Carry the argument further and examine the X-axis arm again. The shorter arm on the Y-axis as the updated perpendicular arm now forces the X-axis arm to be further shorten by the multiplicative factor of $(1 - \frac{V_Y^2}{c^2})^{0.5}$. Continuing this argument of length contraction shows that both arms approach zero lengths, which is the trivial case to produce null results. Effectively, length contraction is applicable in the general velocity case only if the interferometer has no arm lengths and is a point. Length contraction leads to contradictory results and should be eliminated to explain the null results for the general case.

III. CONTRADICTION OF LENGTH CONTRACTION

Einstein [10, §2] derived the apparent round-trip transport over the length L using (3) and (4), but he did not replace his c – v or c + v with his addition of relativistic velocities that he derived in §3 with c = c – v = c + v. Instead, Einstein followed Fizeau's derivation, since both aberration of light and Fizeau's water experiment were most meaningful to him [11]. Einstein never published any analysis of the Michelson-Morley experiment, even in his book, which he deferred to Lorentz, who "showed that the result obtained at least does not contradict the theory of an aether at rest". [12].

Einstein considered two inertial reference frames K and K′ with a relative velocity **v** between them. His second postulate would imply that observers fixed in either frame would see a spherical shell of light expanding from a flash point with a constant speed of c. The Lorentz transformation and its inverse will convert time and space coordinates between the frames with the X coordinate parallel to **v** by using length contraction and time dilation, which is a straightforward proof [13, p.516; 10, §3]. The perpendicular components to the velocity are unchanged while the parallel coordinate and time are transformed. Length contraction, which is a part of the Lorentz transformation, has never been observed directly since it was proposed over a century ago, despite the high precision now achievable with measurement equipment.

To demonstrate the contradiction with length contraction, the Michelson-Morley apparatus is modified so that 5 inertial observers can witness the results concurrently, as shown in Figure 3 below. To simplify the numerical gamma factors, let Observer 1 and 3 be traveling at 0.6 c and Observers 2 and 4 be moving at 0.8 c. The velocity of Observers 1 and 2 is parallel to the X body axis of the apparatus, and Observers 3 and 4 are moving parallel to the Y body axis. The laser outputs a continuous, monochromatic light.

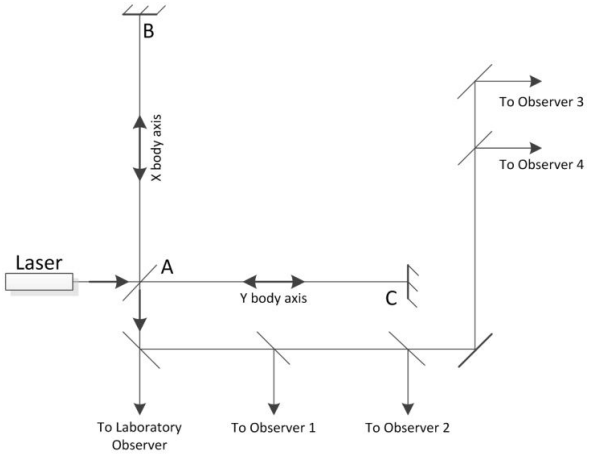

Figure 3: Five inertial observers concurrently viewing output.

Partially silvered mirrors are located at the exit output for the Laboratory Observer and the other Observers 1 through 4. This allows some light to go through those mirrors and reflect other light to be shared with all observers. The merged light beam from A passes through the first partially silvered mirror to the Laboratory Observer, who sees a coherent beam of maximum intensity due to the constructive interference. The core postulate of physical observation requires that all observers witness the maximum energy of the coherent beam, since the same output is shared.

Granted, the moving observers will see a shift in frequency, but the received beam is at maximum intensity for all observers. For calibration of the light sensors, a simple change in AB over one wavelength of the continuous monochromatic laser beam would verify the intensity changed from maximum (full constructive interference) to nothing (full destructive interference) and back to full intensity for all observers when AB is reset.

However, the moving observers have contradictory explanations. Comparing $\Delta T/2$ from Equation (5) to (1) requires that length contraction occurred inside the apparatus for the moving observers to witness the coherent output. Any length contraction applied to the merged beam past the Laboratory Observer would only change the coherent wavelength, but not the intensity. For example, the apparatus must be contracted along the x axis to 0.8L for Observer 1 and concurrently to 0.6L for Observer 2 to observe maximum intensity. Length contraction also requires that the apparatus must be contracted along the y axis to 0.8L for Observer 3 and concurrently to 0.6L for Observer 4. "There is no length contraction perpendicular to the direction of relative motion." [14, p. 872]. The calculations made by Observers 1 and 2 would also prove that no length contraction could be even observed in the perpendicular y axis, which Observers 3 and 4 are moving parallel to the y-axis, while Observers 3 and 4 would make the same claim against Observers 1 and 2 moving parallel to the x-axis. All of this is contradictory, because there is complete disagreement in magnitude and in direction where length contraction could be applied so that all observers recorded a maximum energy of the output laser beam from the experiment.

Length contraction is unnecessary. When light is measured perpendicular to the velocity between inertial frames, the universal speed of light in a nongravitated, vacuum environment is equivalent mathematically to time dilation using this perpendicular velocity. Assume a moving observer transmits a laser pulse perpendicular to the velocity between the moving frame and a stationary frame over the length L marked as AB in Figure 4 with $L = c\Delta t$. In the stationary frame, the laser pulse traverses the hypotenuse A′B where $D = c'\Delta\tau$. The perpendicular length AB moves constantly to the right in Figure 4 to create the triangle AA′B. The laser pulse originates at point A′ and the perpendicular length moves sideways to the right at a constant velocity V. Light reaches the end at B. Light would travel the length AB in the time interval of Δt, but light travels the longer distance of the hypotenuse in $c'\Delta\tau$. Light reaches B when the base A′ is directly below B at point A after the time interval $\Delta\tau$.

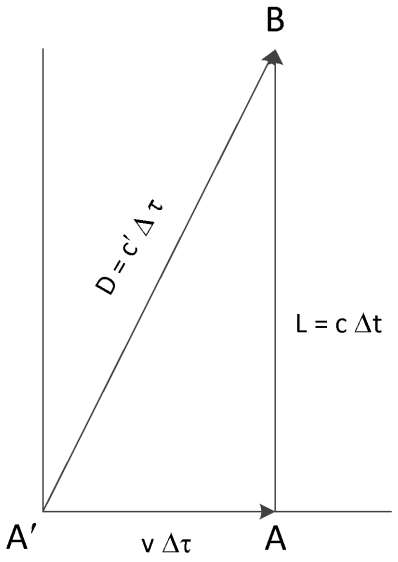

Figure 4: Constancy of light and time dilation.

The Pythagorean theorem [15] leads to the equation:

$$\Delta\tau = \frac{\Delta t}{\sqrt{\left(\frac{c'}{c}\right)^2 - \left(\frac{v}{c}\right)^2}} \qquad (6)$$

Immediately, $c' = c \Leftrightarrow \Delta\tau = \Delta t/\sqrt{1 - v^2/c^2} = \gamma\,\Delta t$. Under special relativity conditions (i.e., no gravity) with inertial frames, the speed of light in a vacuum is a universal constant in all directions if and only if the time dilation equation using this perpendicular velocity is correct. Length contraction is not involved when light is measured perpendicular to the velocity between reference frames.

A real problem surfaces when considering two reference frames with mutually parallel x, y, and z axes, but a general constant velocity V that moves one frame's origin relative to the other. For the general case, velocity V is at angles (θ, φ, ψ) from the respective (x, y, z) axes so that $V\cos(\theta) = v_x$, $V\cos(\varphi) = v_y$ and $V\cos(\psi) = v_z$, but insisting each component velocity differs from the others. Light is measured in the first frame along each axis of length L where $c_x = c_y = c_z$ and the corresponding proper time units, $\Delta\tau = \Delta\tau_x = \Delta\tau_y = \Delta\tau_x$. That numerical value is transformed with the proper time unit Δτ from the first frame into the corresponding time units of the second frame. The above proof states $\Delta\tau = \gamma_x\Delta t = \gamma_y\Delta t = \gamma_z\Delta t$. This states that time dilation $\gamma_x\Delta t$ is applied to the coordinate time units along the y and z axes in the second frame, $\gamma_x\Delta t$ is applied to the coordinate time units along the x and z axes, and $\gamma_z\Delta t$ is applied to the coordinate time units along the x and y axes of the second frame. Time is a scalar unit, but this example shows that time dilation is now directionally oriented based on the different velocity components. The contradiction is that two different coordinate time units for each of the x, y and z axes are designated by the Lorentz time dilation equation. Special relativity is inconsistent, because light speed is transformed from the first frame into different values in the second frame with conflicting time dilation for coordinate time based on different velocity components.

It was proven by Terrell [16] and Penrose [17] that a sphere moving at high velocity would remain visually a sphere [18] that would rotate by an angle $\theta = \sin^{-1}(v/c)$ to the observer [19]. Even a cube centered on the origin that presented only one face when stationary to an observer on the +X-axis would appear to rotate by the same angle θ if the cube moved at a velocity **v** along the Z-axis [19]. This contradicts Einstein's calculation that a moving sphere would appear to be an ellipsoid of revolution [10, §4], because he only analyzed length contraction along the X axis and ignored the Y and Z axes. All diameters of a moving sphere remain the same lengths in three dimensions to the inertial observer. To emphasize this, consider an observer on the positive X axis and a rod that is parallel to the X axis while its center can move on the Y axis. The stationary rod appears to be a point at the origin. When the rod moves at a uniform velocity along the Y axis and crosses the origin, the observer sees the rod of nonzero length along the Y axis. The rod rotates by an angle $\theta = \sin^{-1}(v/c)$ as predicted [16-19]. Such a moving rod exhibits length preservation, not length contraction. The issue is a rigid rod never changes length, regardless how fast it is moving relative to the observer. The moving rod rotates relative to the observer due to the light's finite speed emanated from the end points, but the three-dimensional length is preserved according to the Pythagorean theorem [15] when recording instantly the projection in three dimensions.

Can light speed be a universal constant as assumed by special relativity? Let Observer 1, who is fixed in inertial Frame 1, measure the light speed c. The fixed length span and fixed time interval are divided up into length units of a meter (ΔL_1) and one time unit of a second ($\Delta\tau_1$) to obtain the real number c. Observer 2 has the identical length unit and time unit when at rest in Frame 1. Accelerate Observer 2 until a fixed relative velocity **V** is achieved by moving parallel to the length AB that Observer 1 uses to measure c. Concurrently when Observer 1 conducts the light speed test, Observer 2 measures the moving length AB shortened by length contraction and the time duration that light traveled along AB in Frame 2. Since AB is parallel to the velocity, length contraction should occur. Observer 2 measures the speed of light concurrently with Observer 1 during the test and compares it numerically to Observer 1's value. Defining $\gamma = 1/(1 - v^2/c^2)^{0.5}$, time dilation requires $\gamma\Delta\tau_1 = \Delta\tau_2$ between time units of $\Delta\tau_1$ and $\Delta\tau_2$, respectively, in frames 1 and 2. Length contraction requires $\Delta L_1 = \gamma\Delta L_2$. The transformations show numerically $c_1 \neq c_2$, because the units changed sizes between observers.

$$c_1 = (c)\frac{\text{meter}}{\text{second}} = \left(\frac{\#\text{ length units}}{1\text{ time unit}}\right) \times \frac{\Delta L_1}{\Delta \tau_1} = \cdots$$
$$\left(\frac{\#\text{ length units}}{1\text{ time unit}}\right) \times \frac{\gamma \Delta L_2}{\Delta \tau_2 / \gamma} = (c\,\gamma^2)\frac{\Delta L_2}{\Delta \tau_2} = (c')\frac{\Delta L_2}{\Delta \tau_2} = c_2 \quad (7)$$

Numerically, $c_1 \neq c_2$ as $\gamma > 1$. Einstein proved that a spherical light wave propagated from a point is still a sphere either in a stationary frame fixed at the origin of the expanding sphere or in a moving inertial frame. He also proved the Lorentz transformation for length and time preserves the sphere [10,§3]. Special relativity uses the variable c, which incorporates both a numerical number and units of length and time. If length and time units change in a separate reference frame compared to a standard frame due to a mutual velocity, then the number for light speed must change. For example, light speed is 299792458 m/s that can be converted to yards/minute where a yard < meter (illustrating length contraction) and a minute > second (demonstrating time dilation). Our technology is so precise now that such numerical differences should have been observed, especially with two LIGO observatories (i.e., ultraprecise Michelson-Morley interferometers) at different latitudes. So, how does a laboratory with a fixed light source and fixed light detector measure the same precise value for light speed? How do the retests of the interferometers always produce the same null results regardless how the interferometer is oriented or rotated? A careful reexamination is warranted.

IV. EVALUATION OF INTERFEROMETER TESTS

Runners know that a footrace covers more (or less) ground if the finish line is moved away (or toward) the runners during the race. The same is expected in Zeno's paradox of Achilles and the tortoise. Zeno's paradox relates how the tortoise challenged Achilles to a race with a head start of L, claiming the tortoise would win. Achilles conceded the race without running due to the tortoise's logic that Achilles was always behind the tortoise for an infinite number of time intervals, even though those intervals were approaching zero. Embellish this paradox with two tortoises starting together. The original tortoise is retreating from Achilles at speed v, and the second tortoise approaches Achilles at the same speed v, but Achilles will overtake both with his speed of V > v. These two cases will be solved analytically and applied later to the parallel beam in the equal-arm interferometer.

The tortoises begin at a distance L ahead of Achilles, who runs toward the tortoises at his uniform velocity V. Consider the retreating tortoise first, which Achilles will overtake after running a distance $L_{\rightarrow} > L$. When Achilles runs a distance L over the time L/V, the first tortoise is out of reach by being ξ(1) distance further. When Achilles runs the extra distance ξ(1), the first tortoise has moved a further distance ξ (2) over the same time interval of ξ(1)/V. Over n repetitions of this, the tortoise has moved a distance of L + ξ(1) + ξ(2) + … + ξ(n) where ξ(1) = v × (L/V) and ξ(i+1) = v × ξ(i)/V. Substitute the individual terms with v < V, and the series is:

$$L + v\frac{L}{V} + v\frac{Lv}{V}\frac{1}{V} + \cdots + v\frac{Lv^{n-1}}{V^{n-1}}\frac{1}{V} = \frac{L(1-v^n/V^n)}{1-v/V}$$
$$L_{\rightarrow} = \lim_{n\to\infty} \frac{L(1-v^n/V^n)}{1-v/V} = \frac{L}{1-v/V} \quad (8)$$

Chasing the approaching tortoise, Achilles runs a shorter distance $L_{\leftarrow} < L$ as the second tortoise moves toward Achilles. Note that the velocity of this tortoise is now in the opposite direction of Achilles's velocity, so the ratio of velocities is now negative as -v/V for each term in this series.

$$L\left(1 - \frac{v}{V} + \frac{v^2}{V^2}\cdots\right) = \lim_{n\to\infty} \frac{L(1+(-1)^n v^n/V^n)}{1+v/V} = L\left(\frac{1}{1+v/V}\right) = L_{\leftarrow} \quad (9)$$

Consider a different race. Place the second tortoise beside Achilles at his starting line and place the first tortoise ahead of both at the distance L. A rod of length L could be tied to both tortoises to ensure both crawl at the same slower velocity v and maintain their mutual distance L. Achilles runs after the first tortoise, tags it, turns back, and finally tags the second tortoise. The total distance that Achilles runs in this second race is:

$$L_{\rightarrow} + L_{\leftarrow} = L\left(\frac{1}{1-\frac{v}{V}}\right) + L\left(\frac{1}{1+\frac{v}{V}}\right) = L\left(\frac{2}{1-\frac{v^2}{V^2}}\right) > 2L \quad (10)$$

Algebra can directly verify (8) and (9). Solve for D, the distance the fleeing tortoise moved before Achilles tagged it. In the equation, solve for D in D/v = (L+D)/V with replacement of D in $L_{\rightarrow} = L + D$. Also, solve for d, the distance the approaching tortoise moved before Achilles touched it in d/v = (L-d)/V and replace d in $L_{\leftarrow}$ = L - d.

Transition from the paradox to the Michelson-Morley interferometer where local gravity is perpendicular to the plane containing the two perpendicular arms in the x axis and y axis. At any instant of time, there will be changing velocities of v_x and v_y for each arm moving relative to outer space due to the rotation and orbit of the Earth plus the Milky Way's motions. Michelson and Morley knew the Earth orbited the Sun at approximately 30,000 m/s, but were oblivious that the solar system was in the Milky Way galaxy with additional rotation and movement within the cosmos. They hoped to rotate their platform on a pool of mercury to find the maximum interference when one axis was virtually zero in the projection of Earth's orbital velocity relative to the Sun compared to the maximum projected orbital velocity of the other axis from splitting and merging light beams. Their null result was that maximum intensity was always output from constructive interference regardless of the orientation of the x axis or y axis of the apparatus. The high speed of light would ensure the laboratory frame was effectively inertial, because the apparatus would have no practical change during the few ns to output the merged light.

To illustrate, consider placing the laboratory on Ascension Island or anyplace near the equator. Twice a year, the solar ecliptic will pass through the local plumb line, which is affected by all gravitational sources from the Earth, Moon, Sun, etc. Let the vector **S** to the Sun be directly overhead so the plumb line and body axis z are parallel to **S**, and set up the y axis arm of the interferometer to be parallel with **SxV**, where **V** is the orbital velocity of Earth in the solar barycenter frame. The x axis arm is parallel to **X** = **YxZ**. Vector **V** will be nearly perpendicular to **S**, so v_x will be nearly 30000 m/s and v_y roughly zero. Six hours later, Earth rotation will cause v_x to be nearly zero m/s. The largest that factor γ can be is 1 + 5.0069E-9.

Equation (10) gives the distance that light with velocity V=c traverses a round trip on the x axis arm experiencing a velocity of v_x. That velocity v_x displaces the y axis arm sideways as shown by the isosceles triangle in Figure 2. Divide the isosceles triangle into 2 equal right triangles (e.g., see Figure 4 for one triangle).

The author believes the horizontal axis of Figure 4 is $v_x \Delta t$, where Δt is the time needed for light to traverse the length L_y only, as vector displacements require. In that case, the hypotenuse is $L_y' = L_y(1+v_x^2/c^2)^{0.5}$, and the total distance traveled by the y axis beam in the stationary frame is $2L_y(1+v_x^2/c^2)^{0.5}$ as the v_x velocity moves the interferometer along the x axis. The y axis beam is forced to traverse a longer distance of L_y'. The alternate explanation for the sideway displacement is $v_x \Delta\tau$, where Δτ is the time needed for light to traverse the hypotenuse only, resulting in the hypotenuse to be $L_y' = \gamma_x L_y$ for light to traverse the y axis with a given v_x in the external inertial frame.

In the general case, v_y also exists, so the round trip displacement by the y axis beam along the y axis is (9) with v_y inserted. This also means the x axis beam is displaced sideways due to v_y, forcing the x axis beam to travel along twice the distance of the hypotenuse. That longer distance is either $2\gamma_y L_x$ or $2L_x(1+v_y^2/c^2)^{0.5}$, which both interpretations will be applied to the two interferometers.

For the Kennedy-Thorndike interferometer, the time intervals between splitting and recombining the light beams will be simply the total displacement divided by the light speed c, which is the author's interpretation.

$$\frac{\Delta t_x}{\Delta t_y} = \frac{\frac{2L_x/c}{\left(1-\frac{v_y^2}{c^2}\right)}\sqrt{1+\frac{v_y^2}{c^2}}}{\frac{2L_y/c}{\left(1-\frac{v_x^2}{c^2}\right)}\sqrt{1+\frac{v_x^2}{c^2}}} = \frac{L_x\left(1-\frac{v_y^2}{c^2}\right)}{L_y\left(1-\frac{v_x^2}{c^2}\right)}\frac{\sqrt{1+\frac{v_y^2}{c^2}}}{\sqrt{1+\frac{v_x^2}{c^2}}} \quad (11)$$

Earth's rotation would continually change the speed of the interferometer's body axes relative to the stationary frame (e.g., solar barycentric frame with Earth orbiting the Sun). In the example of placing the laboratory on the equator where Earth rotates at a tangential velocity of 465 m/s, the apparatus's x axis would vary between 30,000 m/s and zero in speed and the y axis would vary between zero and 30,000 sin(23.5°) m/s every six hours. The factor γ_x would vary between 1 and (1+ 5.0069E-9), and the γ_y would vary in the opposite change of γ_x with a smaller maximum. The experimental retests done in 1990 showed no change of destructive interference above 2E-13 [9]. Neither length contraction nor time dilation can explain the output in (11). In terms of the Michelson-Morley interferometer, L_x and L_y would cancel in (11). This ratio must be exactly one as observed, which special relativity still fails to explain.

Using the alternate interpretation for the sideway displacement, the formula of the time ratio with γ factors for the Kennedy-Thorndike interferometer would be:

$$\frac{\Delta t_x}{\Delta t_x} = \frac{2\gamma_x^2\gamma_y L_x/c}{2\gamma_y^2\gamma_x L_y/c} = \frac{\gamma_x L_x}{\gamma_y L_y} \quad (12)$$

Any time dilation inside the moving interferometer should be common to both axes. However, $\gamma_x \neq \gamma_y$ as both factors are continually changing during extended periods of testing as the Earth rotates the interferometer relative to Earth's orbital velocity. The experimental tests showed no change of destructive interference above 2E-13 [9]. In the Michelson-Morley interferometer, the arm lengths cancel, and the ratio in (12) must equal one as observed, forcing $\gamma_x = \gamma_y$, but $v_x \neq v_y$. This contradiction results from assuming light speed is a universal constant. Can light speed vary and still produce the identical precise constant measured in laboratories on Earth?

V. REANALYSIS OF MICHELSON-MORLEY TEST

Without loss of generality of the interferometer experiment, assume the external observer is absolutely stationary. (Another constant velocity could be added to both v and V for the general case and not change the results.) Since there is no net dynamical acceleration or different gravity between frames, special relativity mandates the time units do not change sizes during the test. The laboratory timescale has a time unit that converts precisely to the external observer's time unit by a multiplicative factor. Arbitrary times could be chosen for a common epoch, such as the onset of splitting the light beam at the half-silvered mirror A. The laboratory timescale can be replaced with another timescale defined by a new epoch (t_o = 0 when the beam is split at A) and original time unit divided by the γ scale factor so that the new timescale is identical to the external observer's timescale. So, even if time dilation makes the original time unit different, a conversion is available to create a new laboratory timescale with identical time units of the external observer so that one timescale is needed for both reference frames. It is assumed that both observers have synchronized clocks at the needed locations within the domains of the two reference frames to record coordinate time using this common timescale.

The basic tenant of physics is that observers must witness identical results of the same event when results are transformed to one common inertial frame. The author defines simultaneous to apply only when multiple phenomena or events separate or combine at a point at the same time. When different events occur at separate locations at the same coordinate time, those events are synchronous without being simultaneous. For example, a formation of swimmers performing a synchronous routine are independent of each other as any swimmer can stop moving independently of the other swimmers without interfering. Two novae are synchronous when they explode at the same coordinate time, but if

the transmission times to convey the light to an observer were different, the reception at the observer would be nonsimultaneous. Usually, two novae are not synchronous by exploding at different coordinate times, but simultaneous novae might be recorded serendipity if the two light beams from the stars arrived at the same instant at the observation point.

When light is split at the half-silvered Mirror A, both observers record the same time instant and the respective X coordinates in each frame when a beam moving parallel to the X-axis was created. When the parallel beam touches Mirror C, both observers record the same time instant and the corresponding X coordinate in each frame. (The constant speed of light, V, is slightly slower due to the atmosphere by the index of refraction, but it is nearly c, the light speed in a vacuum.) In this example, the stationary observer records the parallel beam traveled longer than L to overtake the receding Mirror C. Still, the moving laboratory observer makes no compensation for the laboratory's movement through outer space and surmises the parallel beam only traveled a fixed distance L to touch Mirror C in the laboratory frame. However, both observers must record the same identical time interval between the creation of the parallel light beam and the later instant of time when the parallel beam touched Mirror C, since one common timescale was created for both frames.

Referring to Figure 1, the distances between mirrors A and C and between mirrors A and B are both L. When the mirrors A and C move, a light pulse is flashed toward C from A and reflected to A″ as shown in Figure 2. The distances the parallel beam covers between the mirrors in the stationary frame are:

$$L_{AC'} = \frac{L}{1-v/c} = L\left(1+\frac{v/c}{1-\frac{v}{c}}\right) = L\left(\frac{c}{c-v}\right), \text{ and} \qquad (13)$$

$$L_{C'A''} = \frac{L}{1+v/c} = L\left(1-\frac{v/c}{1+\frac{v}{c}}\right) = L\left(\frac{c}{c+v}\right). \qquad (14)$$

The same length L is retained in the moving laboratory frame. In the stationary frame, light traverses a longer, $L_{AC'}$, or shorter, $L_{C'A''}$, than L due to the movement of the apparatus during the test. In (13) and (14), the speed V from (8) and (9) is replaced by c for the speed of light in a vacuum.

A footrace will cover different ground if the finish line moves toward or from the runners during the race. Achilles runs further than L to overtake the receding tortoise by (8) or shorter than L toward the approaching tortoise by (9) with a total footrace > 2L. The external observer witnessing the moving interferometer should encounter the same effects in the parallel beam's displacements.

The laboratory observer makes no compensation for the moving endpoints of either arm in the interferometer moving through outer space. In the stationary frame, the round trip parallel distance is longer than 2L by the addition of (13) and (14). The speed of light is assumed a constant c as based on past measurements of light speed. If the stationary observer measured the one-way transmission interval precisely, the predicted time intervals would be (15) and (16).

$$\Delta T_{A'C'} = \frac{L}{c}\left(1+\frac{v/c}{1-\frac{v}{c}}\right) = T\left(1+\frac{v/c}{1-\frac{v}{c}}\right), \text{ and} \qquad (15)$$

$$\Delta T_{C'A''} = \frac{L}{c}\left(1-\frac{v/c}{1+\frac{v}{c}}\right) = T\left(1-\frac{v/c}{1+\frac{v}{c}}\right). \qquad (16)$$

The time span begins when light beams separate at Mirror A, which is simultaneous between both observers, because the split occurred at one point at one time instant. The two beams later combine at Mirror A simultaneously for both observers at one time instant at a point location. The time spans from splitting a light beam to later combining two light beams must be identical for both observers using the common timescale described earlier.

When light touches Mirror C or Mirror A at A″ in either frame, either event is simultaneous for both observers. Thus, the time span when light overtakes Mirror C moving one-way parallel to V_x is (15) in the laboratory if light's speed is c. When

light moves antiparallel to V_x, the one-way timespan is (16) in the laboratory. The laboratory observer calculates T = L/c. The variation in time spans to traverse the parallel arm must be absorbed in the apparent speed of light, which incorporates time since length has no time units. As the interferometer is stationary in the laboratory frame, the apparent one-way velocities in the laboratory frame are surprisingly:

$$\frac{L}{T_{A'C'}} = \frac{L}{\frac{L}{c}\left(1+\frac{\frac{v}{c}}{1-\frac{v}{c}}\right)} = c - v \text{ , and} \quad (17)$$

$$\frac{L}{T_{C'A''}} = \frac{L}{\frac{L}{c}\left(1-\frac{\frac{v}{c}}{1+\frac{v}{c}}\right)} = c + v \text{ .} \quad (18)$$

The beam overtaking the perpendicular arm in Figure 2 of the external stationary frame travels a round trip distance of 2d, along the hypotenuses AB′ and B′A″, which either is longer than L, a perpendicular leg of the triangles. If c is the emitted speed of light in the stationary frame in all directions, then the transmission intervals to B′ and A″ should be longer than L/c, which would predict destructive interference at the combination point, but both observers must record constructive interference by previous tests. Since light obeys vector addition of parallel velocity by (17) and (18), then it should also obey vector addition of velocity in general. In the stationary frame, the light would have to travel faster to B′ and then to A″ under vector velocity addition where $\vec{V} = \sqrt{c^2 + v^2}\hat{d} = c'\hat{d}$. From Figure 2, the distance d along the hypotenuse is $d = \sqrt{L^2 + v^2(\Delta\tau)^2} = \sqrt{L^2 + v^2L^2/c^2}$. In the stationary frame, the perpendicular beam traverses the longer distance 2d of AB′A″ with a faster light velocity c′ to complete the time interval:

$$\frac{2d}{c'} = \frac{2L\sqrt{1+v^2/c^2}}{c\sqrt{1+v^2/c^2}} = \frac{2L}{c} \quad (19)$$

Again, the laboratory observer makes no compensation for the moving arm perpendicular to the velocity V_x of the laboratory through outer space. Still, the time interval for light to traverse the perpendicular arm in the stationary frame is the same as 2L/c, which the laboratory observer deemed.

A faster speed of light would elongate the wavelength along the hypotenuse, but the frequency would remain unchanged so that c′ = fλ′. If one tuned continuous monochromatic light to create n integer waves in each arm in the laboratory frame, then the wavelengths in the stationary frame along the hypotenuse would also have n longer wavelengths of λ′ due to the faster light speed, but a projection onto the perpendicular leg would obtain the same wavelengths of λ recorded by the laboratory observer. Both observers record the same n wavelengths on the perpendicular arm, but this can only happen if the speed of light obeys vector addition of velocity induced by the interferometer's velocity at emission. A standing wave of n wavelengths on the perpendicular leg must be recorded by both observers in this setup, which will invalidate the γ interpretation for the sideway displacement by (12). This is also true for the parallel arm. For the external observer, the parallel leg is longer by c/(c-v) by (13) and is shorter when antiparallel by c/(c+v) in (14). The external observer counts n wavelengths on the parallel leg only when light's velocity obeys vector velocity addition as c ± v, respectively.

In the stationary frame, the parallel beam travels further than L to overtake the receding Mirror C by (13) and shorter than L by (14) to intercept the approaching Mirror A. The stationary observer allows the endpoints of the parallel arm to move. The laboratory observer considers the parallel light traveled only L in the parallel direction and L in the antiparallel direction, but the stationary observer notes that the respective distances are given by (13) and (14). The round trip distance by adding (13) and (14) > 2L, but the speed of light within the parallel arm is not c in the stationary frame, which would force the parallel beam to travel longer for the round trip than the perpendicular beam and force the recombined beams to exhibit destructive interference. Since the interferometer effectively elongated the parallel distance by the factor c/(c-v) and shortened the antiparallel distance by c/(c+v),

the interferometer alters the speed of light by the same ratios due to velocity containing length units in its numerator. The laboratory observer failed to incorporate the ratio c/(c-v) for the parallel distance and c/(c+v) for the antiparallel distance. Therefore, the speed of light in the stationary frame is affected by the same ratios. The parallel beam's velocity in the stationary frame is faster by $c^2/(c-v)$. After reflection, the parallel beam's velocity is slower by the ratio of $c^2/(c+v)$. The actual time spans in each direction for the stationary observer are:

$$\Delta T_{A'C'} = \frac{\text{Parallel distance traversed}}{\text{faster light speed}} = \frac{L\left[\left(1+\frac{v/c}{1-\frac{v}{c}}\right)\right]}{c\left(\frac{c}{c-v}\right)} = \frac{L}{c}, \text{ and } (20)$$

$$\Delta T_{C'A''} = \frac{\text{Antiparallel distance traversed}}{\text{slower light speed}} = \frac{L\left[\left(1-\frac{v/c}{1+\frac{v}{c}}\right)\right]}{c\left(\frac{c}{c+v}\right)} = \frac{L}{c}. \quad (21)$$

Thus, the recorded parallel and antiparallel times in the stationary frame are precisely L/c in each direction, which makes the total round trip time equal to 2L/c as surmised by the laboratory observer in the laboratory frame.

If a hypothetical medium exists for light transmission with a velocity $\mathbf{V}_x$ and $\mathbf{V}_y$ relative to the stationary frame while the interferometer moves with $\mathbf{v}_x$ and $\mathbf{v}_y$, then the results are unchanged using the total $\mathbf{V}_x = \mathbf{V}_x+\mathbf{v}_x$ and $\mathbf{V}_y = \mathbf{V}_y+\mathbf{v}_y$. Both the stationary observer and laboratory observer will record constructive interference for the output of the Michelson-Morley interferometer, regardless of the speed of a hypothetical medium relative to either observer. This demonstrates that neither interferometer test can prove nor disprove the existence of any hypothetical medium.

This also explains why precise measurements of light speed appear to be a constant no matter what the velocity may be of the moving inertial frame. The movement of the test apparatus relative to outer space is not compensated during laboratory measurements of light speed, so that both the length traversed and the velocity of light are affected equally to maintain the apparent ratio of L/c as a constant time span in any external inertial frame. This means that the measured speed of light is precisely the standard value c if both the light source and light detector are mutually fixed with respect to each other. When the distance between the light source and detector is fixed at a distance L during a measurement, then (20), (21), or half of (19) will produce the standard light speed c = L/(L/c).

Some may argue that prior tests measured the same standard speed of light emitted by a moving particle. For example, γ rays from the decay of π^0 mesons with more than 6 GeV were measured absolutely by timing over a known distance [20]. The test was intended to measure c + kv, and the result was $k = (-3\pm13)x10^{-5}$ for mesons moving near light speed (γ>45). The team used two detectors spaced 31.450 m to measure the time interval the γ rays traveled. Photons are absorbed in a material and subsequently emitted by the atoms of that material. The first detector absorbed the light from high-speed γ rays and emitted light rays afterward at the usual speed of light. The measured speed recorded by the second detector after light passed through the first detector (i.e., absorbed and reemitted at c) was the standard light speed. This and many other tests must be reexamined carefully to ensure that the photon speeds were directly measured without interception to eliminate any mismeasurements causing misinterpretations of the results.

The constructive interference output of the Michelson-Morley interferometer demonstrates that photons obey velocity vector addition as analyzed above. No observer reported that one beam moved off the reflection mirror or the recombination point during the test. This is because the photons move in the required direction mandated by vector displacement. A simple test would demonstrate this. Set a laser to point horizontally at a partially silvered mirror that is angled at 45 degrees relative to the local plumb line. The reflected beam is aimed vertically to a hemisphere mirror that is a distance, d, of about 10 meters above the partially

silvered mirror, so that the hemisphere is centered along the line of transmission. The vertical beam is reflected from the hemisphere of 2 cm radius, r, to the partially silvered mirror below, and some light is transmitted through it to the ground below. Observe if the impact point varies over time as Earth rotates. The hemisphere mirror has a sideway displacement due to the velocity **v** of Earth around the Sun, forcing the beam to miss the nadir of the hemisphere mirror by an angle of $\theta \approx \sin(\theta) = v\,\Delta t / r = vd/(cr)$ in radians. The reflected beam from the hemisphere mirror should touch the ground by a maximum of $d\,\theta$ = 50 cm from the plumb line assuming a maximum $v \approx 30000$ m/s from Earth's orbit. Even assuming a perpendicular projection of Earth's velocity to the 10 m arm that is a slower speed of 15000 m/s, this would still cause a 25 cm displacement from the plumb line. If no observed displacement occurs over a day, then the beam is constantly touching the nadir of the hemisphere mirror. This would prove light obeys vector addition of velocity, not only in magnitude, but also in horizontal displacement (i.e., $\mathbf{v}_\perp \Delta t$) identically as the hemisphere mirror undergoes vector addition of displacement relative to an inertial frame in outer space (i.e., $\mathbf{L'} = \mathbf{L}\ (1+v_\perp{}^2/c^2)^{0.5}$ and $c' = c(1+v_\perp{}^2/c^2)^{0.5}$).

A more rigorous demonstration reveals light does obey vector velocity addition by the operation of a precise version of the Michelson-Morley interferometer over the last three years. The Laser Interferometer Gravitational-Wave Observatory (LIGO) is a large-scale physics experiment with twin observatories to detect cosmic gravitational waves [21]. The observatories are near Hanford, Washington, and Livingston, Louisiana, with 4 km long arms within ultrahigh vacuum chambers allowing laser beams to detect gravity waves. A continuous laser beam is amplified from 40 watts to 750 watts with power reflecting mirrors. The signals are also magnified with signal recycling mirrors. LIGO has enhanced vibration absorption mechanisms to remove ground vibrations, tremors, solid Earth tides, etc. to isolate the signals. To increase the arm lengths from 4 km, Fabry-Perot cavities are installed near the beam splitting mirror and near the hanging reflection mirror at the end of each arm so that 300 reflections inside the cavities increase the effective arm length to almost 1200 km. An ultrahigh vacuum is maintained so that any gaseous molecule is removed promptly to avoid interference with the light beams. Also, one of the split signals is inverted so that destructive interference is created when recombining the two beams. The original Michelson-Morley interferometer gives constructive interference, but this enhancement allows far easier detection of variations after merging signals. Any light is readily seen against an absolute black background, but hard to detect any light variation against a bright light, much like the inability to see sunspots when looking directly at the Sun. LIGO's signal output is complete darkness (i.e., destructive interference) to indicate the recombined beams arrived at the same time. Any deviations from destructive interference (e.g., any light) are the subtle signals that gravity waves should produce according to general relativity. "At its most sensitive state, LIGO will be able to detect a change in distance between its mirrors 1/10,000th the width of a proton." [21]

The standard argument that the Michelson-Morley interferometer produced null results is that special relativity causes the arm parallel to the velocity of the moving interferometer to be shorter by the γ factor than the perpendicular arm (i.e., ratio of (5) and (1)). LIGO reveals special relativity fails to explain its null results (excluding the rare anomalies which LIGO was built to detect). As already mentioned, LIGO signals are not compensated for any speed due to the translational velocities of the Local Group that includes the Milky Way relative to the cosmos (627 km/s [22]), the Milky Way's own translational motion (estimated at 552 km/s [22]), or the solar system's tangential speed from our galaxy's rotation (220 km/s [23]), or Earth's orbital velocity (29.3 to 30.3 km/s between

perigee and apogee) that would cause a sideway displacement of either arm that light traverses. LIGO has the extreme sensitivity to detect the different velocity within each arm due to Earth's rotation.

Pick any suitable geocentric inertial frame for Earth (e.g., J2000 after transforming for rotation, nutation, precession and pole wander since January 2000 to the present or the GPS Earth-Centered, Earth-Fixed (ECEF) frame set to an arbitrary time tag near when LIGO is operating). Let the ECEF frame rotate to map the rotation of LIGO in longitude and geodetic latitude coordinates or equivalent xyz coordinates relative to the fixed geocentric frame during the test. Assume the LIGO arms are oriented north-south (NS) and east-west (EW). (If not, project both arms into NS and EW for each leg within each arm and sum the projected legs in NS and EW distances for a similar analysis.) Each arm has lengths that will be called legs that the two split beams traverse. The first leg is between the beam splitter and the entry point of the nearby Fabry-Perot cavity. The beam is reflected 150 times to cover almost 4 km each way and exits from the opposite cavity to the hanging mirror near the end of the arm. On the return, the reflected beam retraces the leg, reenters the cavity to reflect 150 times and exits the cavity to the splitting mirror. In the round trip, the beam traverses the two short legs twice and reflects a total of 300 times inside the cavity. At the atomic level, photons are absorbed by molecules and emitted so that virtually all emitted photons are aimed in the direction given by Snell's law to return or transmit light through reflective or transparent materials. The photons start each leg at the initial mean location within the reflective material and reach the other end of the leg by impacting molecules at the opposite end without interference from free molecules floating in the pathway due to the ultrahigh vacuum kept in each arm.

In the EW arm, the geodetic latitude is the same for each end of every leg, L(i), so that Earth's rotation imparts the same tangential speed of $465\ cos(lat)$ m/s relative to the geocentric frame. The beam bounces through 150 legs heading east and 150 legs heading west inside the Fabry-Perot cavity, and the beam traverses each short leg twice. Using (10) for each round trip within each leg, the total EW is:

$$\text{Total } L_{\parallel} = \sum_{i=1}^{152}\left(\frac{2L(i)}{1-v^2/c^2}\right) = 2\gamma^2 \sum_{1}^{152} L(i) = 2\gamma_{EW}^2 L_{EW} \quad (22)$$

In the NS arm, the geodetic latitude on the south end is less than the latitude on the north end of each leg. Each emission of a photon traveling from south to north begins from the southernmost latitude, and vice versa. Earth's rotation will cause a sideway displacement of each leg, so that the photons move at c along the hypotenuse as shown in Figure 4. Earth's rotation causes two tangential speeds of $465\ cos(lat_{south})$ m/s faster than $465\ cos(lat_{north})$ m/s for photons emitted respectively on opposite ends of each leg. Use (1) multiplied by c to get each individual leg length, $L_S(i)$ and $L_N(i)$. The total round trip in the NS arm is summed over all legs:

$$\text{Total } L_{\perp} = \sum_{i=1}^{152}\left(\frac{L_{NS}(i)}{\sqrt{1-v_S^2/c^2}}\right) + \sum_{i=1}^{152}\left(\frac{L_{NS}(i)}{\sqrt{1-v_N^2/c^2}}\right) < 2\gamma_{EW} L_{NS} \quad (23)$$

Since total L_{EW} = total L_{NS} for each LIGO observatory on Earth's surface, the output (excluding anomalies) is identical in arrival times for both beams at the recombination point. The ratio of (22) to (23) is not γ_{EW} from length contraction as $\gamma_N < \gamma_S = \gamma_{EW}$. A constant light speed in all directions predicts nonsynchronous output from LIGO for the geocentric observer, but LIGO observers record synchronous output.

However, if each photon has a light speed that obeys vector velocity addition based on the velocity of the molecules emitting the photons, then one obtains the same predicted synchronous output from LIGO for a laboratory or inertially moving observer. For the photons moving within

the NS arm, each one-way transmission over each leg is expressed as L(i) after dividing 2 from all sides of (19). Photons travel over the hypotenuse of distance d, which is longer by L(i) $(1+v^2/c^2)^{0.5}$, where v_i = speed at the latitude of emitted light. Also, the modified light speed, c′, is faster as c $(1+v^2/c^2)^{0.5}$ by vector addition. The result is d/c′ = L(i)/c, which means the observer in the nonrotating geocentric frame will record the same time intervals that photons traverse each perpendicular leg in the moving LIGO observatory as the LIGO observer recorded time spans in the Earth fixed frame. For photons moving within the EW arm, each one-way transmission over each leg L(i) with the modified light speed is given in (20) for parallel transmission and in (21) for antiparallel transmission. In all cases, the geocentric observer will record the same time intervals for each leg as the LIGO observer recording the time spans of L(i)/c.

VI. RAMIFICATIONS

It will take time for others to verify the results of this research, but if the velocity of photons does obey vector velocity addition, then several concepts of physics must be addressed. Readers will recall that most textbooks state that no particle travels faster than the speed of light in a vacuum. Countless electromagnetic experiments seem to demonstrate this. One of the best videos of a rigorous test using a linear accelerator demonstrated that electromagnetic fields alone do not accelerate free electrons faster than c [24]. As the electromagnetic energy was increased to accelerate the free electrons, the velocity of the electrons approached an asymptote of c. The film verified the timing cables were calibrated. It also showed that the colliding electrons did impart heat to the target that nearly equaled the total energy given to the electrons, but the speed of the electrons was virtually c, but less than c. The test is just as valid today as then. Unfortunately, the conclusion has been overgeneralized to state that nothing can go faster than the speed of light. Photons generated by electromagnetic fields are limited to the standard light speed as emitted from the molecules to impart increases in momentum to the charged electrons. The free electrons can be nudged forward by momentum transfer if slower than the moving photons. Once free electrons obtain the limit of the standard light speed, the photons can no longer overtake the electrons to transfer momentum or nudge the free electrons any faster, although more energy can be given to the electrons. Such tests prove that an electrodynamic force alone does not accelerate charged particles faster than the standard light speed in a vacuum relative to the equipment in the laboratory frame.

This paper demonstrated that the measured speed of light will be the standard speed when light sources and detection equipment are mutually fixed. However, when the source has an additional velocity relative to the detector, then Maxwell's equations must be modified to allow c to vary outside of the laboratory frame. This means that Einstein's assumptions for the axioms of special relativity theory are indeed excellent approximations, but not exactly accurate. For example, the last section of Einstein's 1905 paper contained the dynamics of the slowly accelerated electron [10, §10]. He derived that longitudinal mass would differ from transverse mass. No test has confirmed this even exists—directly or indirectly. No one has shown Einstein's derivation has any mathematical flaw concerning this subject. This unverified topic should have raised doubts about the accuracy of these two postulates of relativity. Most electrodynamic experiments do not approach the precision in significant figures to test Maxwell's equations when the sources are moving independent of the detectors.

Some standards of physics will need to be restored. The meter is now defined in terms of the time span it takes light to traverse a meter. With a varying light speed, the physical meter standard should be reestablished as the international unit of length. Some other standards may need reexamination.

General relativity shows that gravity waves and light waves have the same universal speed [25, chapter 5]. "The existence of gravitational waves is an immediate consequence of special relativity and, to some extent, the experimental discovery of gravitational waves would merely confirm the obvious." [25, p. 242] If photons can move at different speeds, then gravity could also have different speeds other than the universal standard speed. General relativity predicted the solar deflection of light and Mercury's perihelion precession. Classical physics can predict the same 1.75″ of solar deflection [26] by allowing the Sun to move as well as the photon. Previous classical derivations only obtained half of the total observed effect using a stationary Sun. General relativity predicts the Mercury perihelion has an excess precession of 42.98″/century [27, 28], but Misner, Thorne and Wheeler published their 1973 evaluation that this residual was 41.4″±0.9″/century [28, p. 1112] after updating for the revised aberration, but they offered no explanation for this discrepancy that general relativity falls outside of the error bounds. "The deviation from the theoretical prediction is not considered significant." [27, p.512] However, the author disagrees, as dynamical astronomers are not that imprecise. A post-Newtonian approximation of an accelerated, rotating frame in a gravitational field yields 5/6 of the general relativity prediction [29]. Both Icarus and Mercury fall within the error bounds of the observations utilizing this post-Newtonian approximation with the appropriate coordinate timescale. This reinforces the author's judgment that relativity is an excellent approximation, but it is not exact.

A variable light speed could modify two particles in the standard model. The muon and tauon are identical in all characteristics to the electron except their masses are different. If a high-energy particle after a collision can exceed the standard light speed, then $E = mc^2$ may be misinterpreted for the same electron with its usual rest mass as a different particle, because c is assumed a constant. A faster speed of light than the standard light speed c would explain all the entanglement experiments where two or more objects at significantly long distances, d, interact with each other within a measured short time interval, Δt (i.e., $c'\Delta t = d > c\,\Delta t$).

A varying light speed would imply that the Lorentz time dilation is incorrect for many precise timing applications. Hafele and Keating claimed they demonstrated time dilation precisely using four atomic clocks flown in commercial aircraft in westward and eastward circumnavigation of the world [30]. Essen, one of two horologists at the National Physical Laboratory (NPL) who operated the original cesium clock in the calibration effort that defined the atomic second, had reviewed the Hafele-Keating report and concluded the alterations in drift rates of the atomic clocks made the results useless [31].

The author examined the clock rates in Tables 1 and 2 [32] of the Hafele-Keating report released in 1972. The fact that the drift rates of 3 of the clocks varied significantly before and after each circumnavigation in Table 1 completely casts doubt that any average of the ensemble demonstrated relativistic time changes, as 3 of 4 clocks did not individually drift according to relativistic predictions. Table 2 proves the stability of those 3 clocks was not maintained throughout the test. Hafele had released his results at a 1971 conference, in which Hafele even doubted his own test. He admitted, "Most people (myself included) would be reluctant to agree that the time gained by any one of these clocks is indicative of anything…." [33, p.273]. By averaging the time gain with 4 clocks, Hafele did get the eastward circumnavigation with error bounds to agree with the predicted theoretical result, but there was no such fit between theory and the westward time gain [33, p. 282]. Keating later worked with Hafele to write the second report with claims that they verified time dilation [31], but careful examination uncovers many discrepancies.

The author's numerical findings on the Hafele-Keating drift rates were duplicated earlier by A. G. Kelly [34]. Kelly obtained the original raw data from the US Naval Observatory (USNO) to review against the published 1972 report and found some data in the tables differed very significantly from raw data with no explanation. Kelly determined Clock #120 performed very irregularly. He wrote, "Discounting this one totally unreliable clock, the results would have been within 5ns and 28ns of zero on the Eastward and Westward tests respectively. This is a result that could not be interpreted as proving any difference whatever between the two directions of flight". Kelly was not condemning relativity, but he was critical that the flight tests were not rigorous, and the claims were unverifiable based on the actual raw data. If light speed is not a universal constant, then clocks may exhibit different time effects than the Lorentz time dilation, which would warrant a more rigorous retesting.

If light obeys vector velocity addition, then a different interpretation of the Sagnac effect is needed. Light is inserted into a ring interferometer and splits in opposite directions. The beams exit the ring at the start/end point and undergo interference. The destructive interference determines how much the ring interferometer rotated after the beams were split. The diagram on the left of Figure 5 [35] shows a nonrotating ring of radius R would output constructive interference as each beam would travel the same length of 2πR and exit at the same time. If the ring interferometer rotated as shown on the right side of Figure 5, one beam would travel further than the other, so both beams would exit with destructive interference.

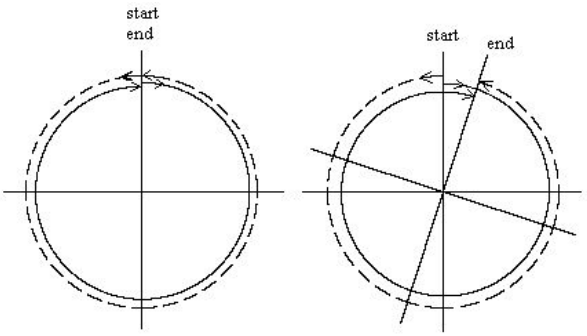

Figure 5: Sagnac effect in circular loops

It is easy to see as an external observer that one beam takes a longer trip than the oppositely traveling beam when the interferometer rotates. The rotating interferometer is a frame that is sufficiently inertial when comparing the constant angular velocity ω with the speed of light. The ring is a conduit that bends both beams to traverse in a circular path. A perpendicular acceleration is required to force the light beams to traverse a circle in the rotating interferometer. Such an acceleration is no different than the perpendicular gravity that exists for the Michelson-Morley interferometer, as any acceleration to the linear paths will be equal to both beams, so the acceleration effects cancel out when combining the two beams. As the beams are bent in circles, the distances covered by both beams in the external frame are Equations (13) and (14) for $L_{\rightarrow}$ and $L_{\leftarrow}$ when setting $L = 2\pi R$ and $v = \omega R$. The time difference between the beams is:

$$\Delta t = \frac{2\pi R}{c}\left[\left(\frac{c}{c-\omega R}\right) - \left(\frac{c}{c+\omega R}\right)\right] = \frac{4\pi\omega R^2}{c^2-\omega^2 R^2} \qquad (24)$$

However, the usual application of the Sagnac effect is found in inertial navigation systems where the interference measurement device is fixed at the exit or end of the rotating ring interferometer. If an observer is fixed with the rotating ring, special relativity requires that each beam originates at the same constant light speed c, and each beam travels the circumference of 2πR in the inertial rotating frame. This set of assumptions of special relativity for the rotation of the ring undergoing constant angular velocity,

ω, would predict both beams exit simultaneously (i.e., constructive interference in the output), but reality contradicts that theoretical prediction. Similarly for the inertial laboratory undergoing a constant linear velocity, v, equations (17) and (18) show that the inertial ring interferometer undergoing constant angular velocity will experience different one-way velocities of the light beams to be c-ωR and c+ωR. This explanation will obtain (24) in the rotating ring frame as output. The identical observed interference of output is witnessed in both inertial rotation frames (i.e., the time difference of opposite circular light beams in an interferometer ring is due to different distances traversed in the stationary rotation frame or due to different velocities of the beams with respect to the rotating frame that is fixed with the rotating ring interferometer). Thus, light obeys vector velocity addition in both linear and rotating reference frames.

This is an incomplete list of possible ramifications if light speed is not a universal constant. In any case, it will take time for the scientific community to review these results.

VII. CONCLUSION

It appeared special relativity was consistent, but some peculiar properties of special relativity reveal unresolved issues. For example, the Lorentz transformation for length and time does not appear to preserve the numerical speed of light. Let light be measured between two points A and B in one inertial frame by an observer fixed in that frame. A second observer calibrates duplicate instruments to the same units. That second observer is accelerated to a desired constant speed, turns around, and travels parallel to AB. The first observer records the speed as the standard numerical value c in m/s, and the second observer measures the light speed concurrently with the first observer to obtain the same quantity. Length contraction and time dilation of the second observer's units will cause the second observer's numerical result to be $\gamma^2 c$ by (7), where $\gamma = 1/(1 - v^2/c^2)^{0.5}$ with different sizes of units. For example, 299792458 m/s can be converted numerically in yards/minute units, which illustrate the length contraction and time dilation of the modified units. In physics, the same standard number for c is used regardless how other inertial frames move. This violates the real meaning of a universal light speed by assuming only one numerical value for all cases. Einstein [10, §3] assumed an algebraic symbol as a constant quantity of light speed, which is a numerical value in units of length and time, but the numerical value must change when the sizes of the units change to maintain the same quantity. Physicists must decide either: (A) the numerical constant for light speed is permanently fixed with no changes in the length and time units of moving inertial frames, (B) the speed of light must change its numerical value whenever the units of measurement change sizes in moving inertial frames, or (C) an alternate model is required.

This paper shows that measuring light perpendicular to the relative motion between inertial frames results in the mathematical identity that the universal speed of light is correct if and only if the Lorentz time dilation equation is correct when using that perpendicular velocity, making length contraction superfluous. This is expected as "There is no length contraction perpendicular to the direction of relative motion."[14] This leads to multiple time dilations used in the transformation between inertial frames. Consider two 3-dimensional inertial frames with (x, y, z) axes mutually parallel, but the origins are moving apart at a relative velocity V with components $v_x \neq v_y \neq v_z$. The observer in Frame 1 measures light speed over three separate lengths of L set parallel to each axis and transforms that light speed of $c_x = c_y = c_z$ to Frame 2. Because light speed was measured in three different directions, the time dilation of the proper time unit $\Delta\tau$ in Frame 1 is transformed to Frame 2 as $\gamma_x\Delta t$, $\gamma_y\Delta t$, and $\gamma_z\Delta t$. Note that $\gamma_x \neq \gamma_y \neq \gamma_z$ where γ_x is computed using v_x, etc. The derivation is based on Figure 4, which shows a time dilation of $\gamma_x\Delta t$ is appropriate for adjusting a

timed quantity in Frame 1 of any phenomena perpendicular to the x axis in Frame 2. The same applies to the time dilation $\gamma_y\Delta t$ for actions in Frame 1 perpendicular to the y axis, and $\gamma_z\Delta t$ for events perpendicular to the z axis. Observer 2 has the dilemma of having three different time dilation terms to perform a Lorentz transformation for any (x, y, z) event in Frame 1 to Frame 2, which is untenable. The three identical values for light speed in Frame 1 are transformed as three different light speeds perpendicular with each of the axes in Frame 2, which then contradicts the universality of light speed.

Special relativity produces contradictions when 3 or more inertial observers are concurrently observing the Michelson-Morley interferometer. As shown in the paper, four inertial observers in spacecraft concurrently witness the shared output of maximum intensity from constructive interference with the laboratory observer. Special relativity would predict no length contraction for the stationary laboratory observer, but it predicts two different length contractions along the x-axis and two separate length contractions parallel to the y-axis for the observers in their spacecraft. Contradictions exist when the five predictions from length contraction have no agreement in direction or size for concurrent observations.

The standard description using special relativity to explain the simultaneous null output (i.e., constructive interference) of the Michelson-Morley test assumes one axis, such as the x axis, is always parallel to the constant velocity of the apparatus. For the external observer, the round trip along the x-axis is $2\gamma^2L'$, and the y-axis round trip is $2\gamma L$. Length contraction obtains $L' = L/\gamma$, which forces the ratio of the round trip intervals to equal one for the null output. However, the orientation of the y-axis is very rarely perpendicular to the velocity vector, resulting in $v_x \neq v_y \neq 0$. The null output must have the ratio $\Delta t_x/\Delta t_y = 1 = \gamma_x/\gamma_y$ by (12), but $\gamma_x \neq \gamma_y$ in virtually all orientations, except the trivial case that both arms have zero lengths.

This paper derives the total displacement of each beam in each direction for both the Michelson-Morley interferometer with equal arms and the Kennedy-Thorndike interferometer with unequal arms. The linear movement on the x axis by a velocity v_x causes a sideway displacement of the y axis as shown in Figure 2 for the external observer. A similar effect of v_y causes a sideways movement of the x axis. The total distances are calculated using an infinite series. Based on vector addition of displacements divided by c, the ratio of time intervals for the round trip excursion over either arm by (11) or (12) is determined for both types of interferometers. Special relativity fails to predict the static output except for the trivial case when the interferometer is a point (i.e. no arms) or in the very rare case that one leg is constantly perpendicular with the constant velocity of the interferometer through space. The latter case is routinely disproved as Earth's rotation and orbital velocity changes v_x and v_y of the interferometer arms relative to the supposed constant velocity fixed in outer space, but the output remains unchanged.

This paper illustrates the ratio of time intervals by dividing light's speed into each beam's round trip excursion. Equation (12) predicts the output of $\Delta t_x/\Delta t_y = \gamma_x L_x/\gamma_y L_y$. As $v_x \neq v_y$ and varies continually, then $\gamma_x \neq \gamma_y$. The output should change continually for the Kennedy-Thorndike interferometer, contrary to test results of unchanging interference. Any time dilation is common to both unequal arms. Likewise, for the Michelson-Morley interferometer, the predicted output for the external observer is a ratio $\Delta t_x/\Delta t_y \neq 1$, but 1 is required to obtain the observed constructive interference. Special relativity does not explain the output in general from either test.

The Laser Interferometer Gravitational-Wave Observatory (LIGO) is a large-scale version of the Michelson-Morley interferometer with twin observatories to detect cosmic gravitational waves [21]. Both observatories have operated for months outputting null results, except for the rare anomalies that they were designed to detect.

Earth's freely falling frame is considered an inertial frame, so any geocentric, nonrotating frame of Earth should suffice for comparison to the LIGO on a rotating Earth using special relativity to predict null results. LIGO is positioned generally with one arm oriented east-west (EW) and the perpendicular arm oriented north-south (NS). Earth's rotation creates a tangential EW velocity in the geocentric frame. The total EW time of transmission is $2\gamma_{EW}^2 L/c$. The sideways motion of the perpendicular arm causes the NS interval to be $(\gamma_S L + \gamma_N L)/c$. In most laboratories, $\gamma_N \approx \gamma_S$ as the arms are short. However, LIGO has 4 km long arms, and the tangential velocity from rotation on the north end of an arm is slightly slower than the south end that also has the same velocity as the EW arm endpoints. For LIGO, $\gamma_N < \gamma_S = \gamma_{EW}$. LIGO is designed so that nothing interferes with the emitted beam from the originating end of an arm. LIGO has the extreme sensitivity to detect any subtle difference, such as $\gamma_N < \gamma_S$, but LIGO outputs null results (except for the rare anomalies). Thus, special relativity fails to adequately explain the null output from this ultraprecise Michelson-Morley interferometer.

A detailed reexamination of both interferometers is made. In the moving interferometer, light travels further than the arm L to overtake the receding mirror and shorter than L to intercept the approaching mirror on the other end of the arm, but the total round trip is greater than 2L. The laboratory observer makes no compensation for the moving endpoints of either arm as the interferometer moves through outer space. The laboratory observer assumes light speed is c based on previous measurements, so the expected time interval in the laboratory frame is this expected distance through outer space divided by c, which the external observer measures as the precise one-way transmission interval. If the laboratory observer assumed the arm distance is L, then L/(expected time interval) = $c \pm v_x$ by (17) or (18) in either direction. More details are derived for the light beam's traverse along the perpendicular arm. In all cases, the (actual distance traversed)/ (modified speed) = L/c, which is the one-way time interval surmised by the laboratory observer. If the laboratory observer tuned the light so that exactly n wavelengths are standing on the equal arms, then vector velocity addition is the required result in the external frame so that both external and laboratory observers record the same nodes of light on both arms.

Consequently, light not only obeys vector velocity addition in magnitude, but also in displacement. No report has been made that the light beams inside the interferometers exhibited a diurnal drift away from the recombination point after months of continuous operation, which LIGO has conducted. As described in the paper, a simple test using a laser beam, half-silvered pane, and a small hemisphere mirror could demonstrate that the laser beam stays on the nadir of the hemisphere mirror, even though the mirror exhibits perpendicular displacement to the laser beam due to Earth's motion through the domain of an inertial frame in outer space. This would demonstrate that not only does the speed of light vary in magnitude due to vector velocity addition, but the direction of the light beam also obeys vector addition of displacement.

The concept that light's velocity obeys vector velocity addition is simply an improvement over Einstein's excellent approximation that light speed was a universal constant in all directions. At its inception, special relativity had a slight shortcoming that cast doubt on its accuracy. Special relativity predicted that longitudinal mass is $\gamma^3\mu$ and transverse mass is $\gamma^2\mu$ for a particle's velocity in an inertial frame where μ is the rest mass of the particle [10, §10]. No test has identified any directional dependence when mass is measured, either directly observed or indirectly inferred from other phenomena. As demonstrated in the paper, the measured speed of light is the standard value when the light source and light detector are mutually fixed.

Ironically, neither the Michelson-Morley nor the Kennedy-Thorndike experiments can prove or disprove the existence of a hypothetical ether in

the transmission of electromagnetic light. Regardless of the velocity of the hypothetical ether relative to the interferometer, identical results are produced. It is also shown that the ring interferometer that utilizes the Sagnac effect has the same property. Thus, light obeys vector velocity addition in both inertial reference frames and inertial rotating rings.

If others verify that light obeys vector velocity addition, then several physics concepts will need to be revised. Previous test results should be reviewed to determine if updates are necessary, but the precision in significant figures will generally not change most results. Several ramifications have been listed in the paper, such as old standards would need to be reestablished, like the physical meter, if light speed is not a fixed, exact numerical constant in all reference frames. It would not be surprising that other axioms of physics, concepts, or physical models may need revision in the future.

REFERENCES

1. Fizeau, H., (1851) "Sur les hypothèses relatives à l'éther lumineux". Comptes Rendus **33**: 349–355.
2. Fizeau, H., (1859)"Sur les hypothèses relatives à l'éther lumineux". Ann. de Chim. et de Phys **57**: 385–404.
3. Michelson, A. A. and Morley, E. W., (1886) "Influence of Motion of the Medium on the Velocity of Light". Am. J. Science **31**: 377–386.
4. Michelson, A. A., (1881) "The Relative Motion of the Earth and the Luminiferous Ether". Am. J. Science **22**: 120–129.
5. Michelson, A. A. and Morley, E. W.,(1889) "On the feasibility of establishing a light-wave as the ultimate standard of length". Am. J. Science **38**: 181–186.
6. Serway, R. A. and Jewett Jr., J. W., (2014) Physics for Scientists and Engineers, Cengage Learning, 9th ed., p. 1196-1198.
7. Kennedy, R. J.; Thorndike, E. M., (1932) "Experimental Establishment of the Relativity of Time". *Physical Review,* **42** (3): 400–418.
8. Jaseva, T. S., Murray J., and Townes, C. H., (1964) "Test of Special Relativity or of the Isotropy of Space by Use of Infrared Masers" Physical Review, **133** (5A):1221.
9. Hils, D., and Hall, J. L., (1990) "Improved Kennedy-Thorndike experiment to test relativity", Phys. Rev. Lett. **64** (15): 1967.
10. Einstein, A., (1905) "On the Electrodynamics of Moving Bodies" Ann. Phys. **17**: 549-560, (translated from 1923 edition of W. Perrett and G. B. Jeffery in The Principle of Relativity:..., Methuen, London.)
11. Shankland, R. S., (1963) "Conversations with Albert Einstein". American Journal of Physics **31** (1): 47–57.
12. Einstein, A., (1961) Relativity: The Special and the General Theory, Three Rivers Press, New York, 15th ed., ISBN 0-517-88441-0.
13. Jackson, J. D., (1975) Classical Electrodynamics, 2nd ed., John Wiley & Sons, New York.
14. Young, H. D., Adams, P. W., and Chastain, R. J., (2016) Sears and Zemansky's College Physics, Pearson, 10th ed., p. 869-872.
15. Euclid, Elements, Book 1, Proposition 47.
16. Terrell, J., (1959) "Invisibility of the Lorentz Contraction", Phys. Rev. 111, (4): 1041-1045.
17. Penrose, R., (Jul 1958) "The Apparent Shape of the Relativistically Moving Sphere", *Proc. Camb. Phil. Soc.* **55**.
18. Marion, J. B., (1970) Classical Dynamics of Particles and Systems, Academic Press, NY, 2nd ed., 326-327.
19. Weisskopf, V. F., (1960) "The Visual Appearance of Rapidly Moving Objects", Phys. Today **13** (9): 24.
20. Alväger, T. A., Farley, F. J. M., Kjellman, J., and Waller, I, (1964) "Test of the Second Postulate of Special Relativity in the GeV Region", Physics Letters, **12** (3): 260-262.
21. LIGO.caltech.edu website (operated by Caltech and MIT), Facts subpage lists the extreme engineering to construct LIGO and its operation.
22. Kogut, Alan; et al., (December 10, 1993). "Dipole anisotropy in the COBE Differential Microwave Radiometers First-Year Sky Maps". The Astrophysical J., **419**: 1-6.

23. Fix, J. D., (2004) Astronomy: Journey to the Cosmic Frontier, 3rd ed., McGraw-Hill, p. 532,
24. Bertozzi, W., "The ultimate speed: and exploration with high energy electrons", Educational Development Center, Newton, Mass.
25. Ohanian, H. C. and Ruffini, R. (1994) Gravitation and Spacetime, 2nd ed, W. W. Norton and Co., New York,
26. Deines, S. D., (2016) "Classical Derivation of the Total Solar Deflection of Light", *Int. J. App. Math. and T. Phys.,* **2**(4): 52-56, DOI 10.11648/ j.ijamtp.20160204.15.
27. Goldstein, H., (1981) Classical Mechanics, 2nd ed., Addison-Wesley Publishing Co., Reading, MA, p. 511-512.
28. Misner, C. W., Thorne, K. S., and Wheeler, J. A., (1973) Gravitation, W. H. Freeman and Co., San Francisco, p. 1112-1113.
29. Deines, S. D., (2017a) "Comparing Relativistic Theories to Observed Perihelion Shifts of Mercury and Icarus", Int. J. App. Math. and T. Phys., **3**(3): 61-73, DOI 0.11648/j.ijamt. 20170303.14.
30. Hafele, J. C. and Keating, R. E., (1972) "Around-the-World Atomic Clocks: Predicted Relativistic Time Gains", *Science*, **177**: 166-177. Essen, L., Creation Res. Society Quarterly, (1977) 14: 46.
31. Essen, L., (1977) Creation Res. Society Quarterly, **14**, 46.
32. Deines, S. D., (2017b) 'Vector Addition of Light's Velocity Versus the Hafele-Keating Time Dilation Test', Int. J. App. Math. and T. Phys., **3**(3):50-55, DOI 10.11648/j.ijamtp. 20170303.12.
33. Hafele, J. C., (1971) "Performance and Results of Portable Clocks in Aircraft", Third Annual Department of Defense (DOD) Precise Time and Time Interval (PTTI) Strategic Planning Meeting, 16-18 Nov 1971, Washington, DC, p. 261-288
34. Kelly, A. G., (2000) "Hafele and Keating Tests: Did They Prove Anything?", Physics Essays, **13**(4): 616, DOI: 10.4006/1.3025451.
35. https://www.mathpages.com/rr/s2-07/2-07. Htm3

There are Infinitely Many Mersenne Primes

Fengsui Liu

ZheJiang University Alumnus

ABSTRACT

From the entire set of natural numbers successively deleting the residue class 0 mod a prime, we retain this prime and possibly delete another one prime retained. Then we invent a recursive sieve method for exponents of Mersenne primes. This is a novel algorithm on sets of natural numbers. The algorithm mechanically yields a sequence of sets of exponents of almost Mersenne primes, which converge to the set of exponents of all Mersenne primes. The corresponding cardinal sequence is strictly increasing. We capture a particular order topological structure of the set of exponents of all Mersenne primes. The existing theory of this structure allows us to prove that the set of exponents of all Mersenne primes is an infnite set .

Keywords and phrases: Mersenne prime conjecture, modulo algorithm, recursive sieve method, limit of sequence of sets.

Classification: FOR Code: 010299

Language: English

London Journals Press

LJP Copyright ID: 925622
Print ISSN: 2631-8490
Online ISSN: 2631-8504

London Journal of Research in Science: Natural and Formal

Volume 20 | Issue 3 | Compilation 1.0

There are Infinitely Many Mersenne Primes

Fengsui Liu

ABSTRACT

From the entire set of natural numbers successively deleting the residue class 0 mod a prime, we retain this prime and possibly delete another one prime retained. Then we invent a recursive sieve method for exponents of Mersenne primes. This is a novel algorithm on sets of natural numbers. The algorithm mechanically yields a sequence of sets of exponents of almost Mersenne primes, which converge to the set of exponents of all Mersenne primes. The corresponding cardinal sequence is strictly increasing. We capture a particular order topological structure of the set of exponents of all Mersenne primes. The existing theory of this structure allows us to prove that the set of exponents of all Mersenne primes is an infnite set .

Keywords and phrases. Mersenne prime conjecture, modulo algorithm, recursive sieve method, limit of sequence of sets.

Author: Nan Chang, China by "ZheJiang University alumnus, China".

I. INTRODUCTION

A Mersenne number M_x is a number that is one less than a power of two

$$M_x = 2^x - 1.$$

A Mersenne prime is a Mersenne number that is prime.

The first few Mersenne primes are:

3, 7, 31, 127, 8191, 131071, 524287, 2147483647, 2305843009213693951, 618970019642690137449562111,. . . (A000668 in the OEIS).

The first few exponents x that give Mersenne primes are:

2, 3, 5, 7, 13, 17, 19, 31, 61, 89, . . . (A000043 in the OEIS).

Mersenne primes are named after Marin Mersenne, a French Minim friar who studied them in the early 17th century.

Many great mathematicians studied Mersenne primes and left many interesting stories. We do not repeat those stories [13].

Euclid proved that if $2^p - 1$ is prime, then $2^{p-1}(2^p - 1)$ is an even perfect number. Euler proved that, conversely, all even perfect numbers have this form [1]. So that the search for Mersenne primes is also the search for even perfect numbers. This is well known as the Euclid–Euler theorem.

On December 21, 2018, it was announced that The Great Internet Mersenne Prime Search (GIMPS) discovered the largest known prime number, the 51-th Mersenne prime, $2^{282589933} - 1$, having 24862048 digits. A comput-

[1]2010 Mathematics Subject Classi cation . Primary 11N35; Secondary 11N45, 11A07,11Y16, 11B37,11B50.

London Journal of Research in Science: Natural and Formal

er volunteered by Patrick Laroche from Ocala, Florida, made the find on December 7, 2018.[4].

Mathematicians believe that the set of Mersenne primes is infinite. "But we are still missing a proof that this guess is true. We are still waiting for a modern day Euclid to prove that Mersenne's primes never run dry. Or perhaps this far-off peak is just a mathematical mirage." in "The music of the primes" the mathematician Marcus du Sautoy said[13].

Lenstra--Pomerance--Wagstaff conjectured that there are infinitely many Mersenne primes [2], [3], and made a quantitative variant formula based on the heuristics model of primes. The number of Mersenne primes up to x is

$$e^{\gamma} \times \log\log(x)/\log(2).$$

It is also not known whether infinitely many Mersenne numbers with prime exponents are composite.

The author had published that there are infinitely many Mersenne composite numbers with prime exponents by the recursive sieve method [9] [10]. In this paper, we prove that there are infinitely many Mersenne primes by an interaction between proof and algorithm, like the proof of Chinese remainder theorem.

In section 2, we repeat a sifting process of primes and obtain the recursive formula for primes p_i. By slightly refining the sifting process of primes, we design a recursive sieve for Mersenne primes.

In section 3, we prove Mersenne prime conjecture based on order topological theory for the sifting process.

II. A RECURSIVE SIEVE METHOD FOR MERSENNE PRIMES

Within the framework of recursion theory, we reformulate Eratosthenes sieve method and invent recursive sieve method, which is a modulo algorithm on sets of natural numbers

For expressing this modulo algorithm by well formed formulas, we need to extend both basic operations addition and multiplication $+$, $\times$ into finite sets of natural numbers, and introduce several definitions and notation.

We use small letters a, x, t to denote natural numbers and capital letters A, X, T to denote sets of natural numbers except for M_x.

For arbitrary both finite sets of natural numbers A, B we write

$$A = \langle a_1, a_2, \ldots, a_i, \ldots, a_n\rangle,\ a_1 < a_2 < \cdots < a_i < \cdots < a_n,$$

$$B = \langle b_1, b_2, \ldots, b_j, \ldots,\ b_m\rangle,\ b_1 < b_2 < \cdots < b_j < \cdots < b_m.$$

We define

$$A + B = \langle a_1 + b_1, a_2 + b_1, \ldots, a_i + b_j \ldots, a_{n-1} + b_m, a_n + b_m \rangle,$$
$$AB = \langle a_1 b_1, a_2 b_1, \ldots, a_i b_j \ldots, a_{n-1} b_m, a_n b_m \rangle.$$

Example:

$$\langle 1, 5 \rangle + \langle 0, 6, 12, 18, 24 \rangle = \langle 1, 5, 7, 11, 13, 17, 19, 23, 25, 29 \rangle,$$
$$\langle 6 \rangle \langle 0, 1, 2, 3, 4 \rangle = \langle 0, 6, 12, 18, 24 \rangle.$$

For the empty set $\emptyset$ we define $\emptyset + B = \emptyset$ and $\emptyset B = \emptyset$.
We write $A \setminus B$ for the set difference of A and B.
Let

$$X \equiv A = \langle a_1, a_2, \ldots, a_i, \ldots, a_n \rangle \mod a$$

be several residue classes $\mod a$.
If $\gcd(a, b) = 1$, we define the solution of the system of congruences

$$X \equiv A = \langle a_1, a_2, \ldots, a_i, \ldots, a_n \rangle \mod a,$$
$$X \equiv B = \langle b_1, b_2, \ldots, b_j, \ldots, b_m \rangle \mod b$$

to be

$$X \equiv D = \langle d_{11}, d_{21}, \ldots, d_{ij}, \ldots, d_{n-1m}, d_{nm} \rangle \mod ab,$$

where $x \equiv d_{ij} \mod ab$ is the solution of the system of congruences

$$x \equiv a_i \mod a,$$
$$x \equiv b_j \mod b.$$

The solution $X \equiv D \mod ab$ is computable and unique by the Chinese remainder theorem.

For example, $X \equiv D = \langle 5, 25 \rangle \mod 30$ is the solution of the system of congruences

$$X \equiv \langle 1, 5 \rangle \mod 6,$$
$$X \equiv \langle 0 \rangle \mod 5.$$

We known that the residue class $a_i \mod a$ is the set of natural numbers $\{x : x \equiv a_i \mod a\}$, several residue classes $A \mod a$ is the union of several sets. Thus we may write the relation $x \in A \mod a$ and set operation $B \cup (A \mod a)$.

Except extending $+, \times$ into finite sets of natural numbers, we continue the traditional interpretation of the formal language $0, 1, +, \times, \in$. The reader who is familiar with model theory may know, we have founded a new model or structure of a second-order arithmetic by a two-sorted logic

$$\langle P(N), N, +, \times, 0, 1, \in \rangle,$$

and a formal system

$$\langle P(N), N, +, \times, 0, 1, \in\rangle \models PA \cup ZF,$$

where N is the set of all natural numbers, and $P(N)$ is the power set of N; PA is the Peano theory, and ZF is the set theory.

We denote this model by $P(N)$.

The second-order language $\langle 0, 1, +, \times, \in\rangle$ has stronger expressive power. The second-order formal system $P(N)$ has some exotic mathematical structures in terms of sets of natural numbers; the first order formal system has no such structures.

Traditional recursion theory discusses functions, their inputs and outputs are natural numbers. We have computed out 51 Mersenne primes, but the evidence does not provide theoretical information about infinitude.

In the second-order arithmetics $P(N)$, we may construct recursive functions on sets of natural numbers by arithmetical operations $+, \times$ and set-theoretical operations $\cup, \cap, \setminus$, their inputs and outputs are sets of natural numbers. Then we obtain a sequence of sets of natural numbers (T_i'), which converges to the set T_e of all exponents of Mersenne primes. We reveal an exotic structure of the set T_e. The existing theory of those structures, order topology, allows us to prove the conjecture.

Now we repeat a sifting process for primes.
Let p_i be the i-th prime, $p_0 = 2$. Let

$$m_{i+1} = \prod_0^i p_j.$$

From the entire set of natural numbers, we successively delete the residue class $0 \mod p_0, 0 \mod p_1, \ldots, 0 \mod p_i$, i.e., the set of all numbers x such that the least prime factor of x is p_i, instead of the multiples of p_i in a given range. Then the left residue class $T_{i+1} \mod m_{i+1}$ is the set of all numbers x such that x does not contain any prime $p_j \leq p_i$ as a factor $(x, m_{i+1}) = 1$.

Let T_{i+1} be the set of least nonnegative representatives of the left residue class $T_{i+1} \mod m_{i+1}$. Then we obtain a recursive formula for the set T_{i+1} and the prime p_{i+1}, which represents the recursive sieve method for primes [9].

$$\begin{aligned} T_1 &= \langle 1\rangle, \\ p_1 &= 3, \\ T_{i+1} &= (T_i + \langle m_i\rangle\langle 0, 1, 2, \ldots, p_i - 1\rangle) \setminus \langle p_i\rangle T_i, \\ p_{i+1} &= g(T_{i+1}), \end{aligned} \tag{2.1}$$

where $X \equiv \langle p_i \rangle T_i \mod m_{i+1}$ is the solution of the system of congruences

$$X \equiv T_i \ mod \, m_i,$$

$$X \equiv \langle 0 \rangle \ mod \, p_i,$$

and $g(T)$ is a projective function, which takes the smallest number in the set but the number 1.

$$g(T) = g(\langle t_1, t_2, \ldots, t_n \rangle) = t_2.$$

The cardinality of the set T_{i+1} is

$$|T_{i+1}| = \prod_0^i (p_j - 1). \tag{2.2}$$

We exhibit the first few terms of formula (2.1)

$$\begin{aligned}
T_1 &= \langle 1 \rangle, \\
p_1 &= 3, \\
T_2 &= (\langle 1 \rangle + \langle 2 \rangle \langle 0, 1, 2 \rangle) \setminus \langle 3 \rangle = \langle 1, 5 \rangle, \\
p_2 &= 5, \\
T_3 &= (\langle 1, 5 \rangle + \langle 6 \rangle \langle 0, 1, 2, 3, 4 \rangle) \setminus \langle 5, 25 \rangle = \langle 1, 7, 11, 13, 17, 19, 23, 29 \rangle, \\
p_3 &= 7.
\end{aligned}$$

It is easy to prove this primitive recursive formula by mathematical induction.

In contrast with Eratosthenes sieve, which does not automatically provide theoretical information, the recursive sieve method itself mechanically provides a constructive proof of Euclid's theorem, that there are infinitely many primes[9].

This formula gives a recursive structure for every prime. Thus primes do not appear randomly; they are computed one after the other by $+, \times$. They are governed by a recursive rule. Recursion opens new theoretical windows onto our understanding of the primes. It seems this is a prime conspiracy.

We may directly extend this constructive proof into several arithmetic progressions, for example, $3x - 1$ or $4x - 1$ or $6x - 1$. We can not extend this constructive proof into Mersenne primes.

We rewrite the sifting process for primes to design a sieve for Mersenne primes and prove the Mersenne prime conjecture.

Based on the recursive sieve method for primes, formula (2.1), we successively delete all numbers x such that x contains the least prime factor p_i, we delete all composites together with the prime p_i. The sifting condition

or 'sieve' is

$$x \equiv 0 \ mod\, p_i \wedge p_i \leq x.$$

We modify the sifting condition to be

$$x \equiv 0 \ mod\, p_i \wedge p_i < x. \tag{2.3}$$

With this new sifting condition or 'sieve' we successively delete the set C_i of all numbers x such that x is composite with the least prime factor p_i,

$$C_i = \{x : x \in T_i \mod m_i \wedge x \equiv 0 \mod p_i \wedge p_i < x\},$$

but save the prime p_i.

We delete all composite sets C_j with $0 \leq j < i$ from the set N of all natural numbers and leave a sifted set

$$L_i = N \setminus \bigcup_{0}^{i-1} C_j.$$

In the sifted set, every number x does not contain any prime p_j, with $0 \leq j < i$, as factor except itself.

We delete all composite sets C_i and leave the end-sifted set, which is set of all primes T_e,

$$T_e = N \setminus \bigcup_{0}^{\infty} C_i.$$

Let A_i be the set of all primes less than p_i, the set of survivors

$$A_i = \langle 2, 3, 5, 7, \ldots, p_{i-1} \rangle.$$

From the recursive formula (2.1), we deduce that the sifted set L_i is the union of the set A_i of survivors and the residue class $T_i \mod m_i$,

$$L_i = A_i \cup (T_i \mod m_i) \tag{2.4}$$

Now we modify the sifting condition (2.3) to obtain sets of exponents of Mersenne primes.

From the identity

$$2^{ab} - 1 = (2^a - 1)(1 + 2^a + 2^{2a} + 2^{3a} + \cdots + 2^{(b-1)a}),$$

we know that the Mersenne sequence is a divisibility sequence. In other words, M_n divides M_m if and only if n divides m. It follows that every Mersenne prime M_p must has a prime exponent, but not every Mersenne number M_p with a prime exponent is Mersenne prime; any both Mersenne numbers M_p and M_q with prime exponents are coprime.

We discuss the set T_e of all exponents of Mersenne primes and its infinitude in the set N of all exponents of Mersenne numbers.

If we only consider a Mersenne number as a divisor of Mersenne numbers inside the divisibility system of Mersenne numbers, then the set T_e of all primes is the set of all exponents of Mersenne primes, every Mersenne number M_p with prime exponent does not contain any Mersenne number M_x as a factor except 1 and itself.

A Mersenne number M_q with prime exponent may contain normal prime factors, which are not numbers of the form 2^x-1, for example, $M_{11} = 23\times89$. Thus we must remove every prime q in the set T_e of all primes if M_q contains a normal prime p as a factor except itself.

Note the notion of divisibility inside the system of Mersenne numbers is different from the usual notion.

About normal prime factors of a Mersenne number with prime exponent, we have known some simple facts [1].

(1) A prime number divides at most one Mersenne number with prime exponent.
(2) Let p be a prime. Then there is a number x such that $p|M_x$ if only if there is a number $c < p$ such that $p|M_c$.
(3) If q is an odd prime, then every prime p that divides M_q is congruent to $\pm1 \mod 8$.
(4) If q is an odd prime, then every prime p that divides M_q must be 1 plus a multiple of $2q$, $p - 1 = 2kq$. This holds even when M_q is prime.
(5) Let $p \equiv 3 \mod 4$ be prime and $2p + 1$ is also prime, if and only if $2p + 1$ divides M_p.

One proves (1) by coprime. One proves (2),(3),(4),(5) by Fermat's little theorem

$$a^{p-1} \equiv 1 \mod p.$$

It follows that we only need to modify successively the set A_i of survivors for each prime p_i to obtain a new set A_{i+1} of survivors, such that if $a \in A_{i+1}$, then M_a contains neither normal prime $p \leq p_i$ nor Mersenne prime $M_p \leq M_{p_i}$ as a factor except itself.

Given any prime p_i, suppose that we have a modified set A_i, then we obtain the next set A_{i+1} by the following rules.

If the prime p_i is congruent to $\pm 1 \mod 8$, let $p_i - 1 = 2kq$, and if there is an odd prime q in the set A_i such that

$$p_i < M_q \wedge p_i|M_q,$$

London Journal of Research in Science: Natural and Formal

then M_q is a Mersenne composite, which contains the least normal prime factor p_i. We remove the prime q from the set A_i and add the prime p_i to obtain the set A_{i+1}.

$$A_{i+1} = (A_i \cup \langle p_i \rangle) \setminus \langle q \rangle.$$

If there is no such a prime q, example $p_i \equiv 3, 5, \mod 8$, then for every number x in the sifted set L_i the Mersenne number M_x does not contain the normal prime p_i as a factor. We add the prime p_i into the set A_i

$$A_{i+1} = A_i \cup \langle p_i \rangle.$$

Now for every number x in the sifted set L_{i+1}, the Mersenne number M_x does not contain Mersenne number M_{p_i} as a factor and does not the normal prime p_i as a factor also except itself.

We exhibit the first few terms of modified sets A_i as examples.

$$\begin{aligned}
A_1 &= \langle 2 \rangle, \\
A_2 &= \langle 2, 3 \rangle, \\
A_3 &= \langle 2, 3, 5 \rangle, \\
A_4 &= \langle 2, 3, 5, 7 \rangle, \\
A_5 &= \langle 2, 3, 5, 7, 11 \rangle, \\
A_6 &= \langle 2, 3, 5, 7, 11, 13 \rangle, \\
A_7 &= \langle 2, 3, 5, 7, 11, 13, 17 \rangle, \\
A_8 &= \langle 2, 3, 5, 7, 11, 13, 17, 19 \rangle, \\
A_9 &= \langle 2, 3, 5, 7, 13, 17, 19, 23 \rangle, M_{11} = 23 \times 89, \\
A_{10} &= \langle 2, 3, 5, 7, 13, 17, 19, 23, 29 \rangle, \\
A_{11} &= \langle 2, 3, 5, 7, 13, 17, 19, 23, 29, 31 \rangle,
\end{aligned}$$

The sifting condition formula (2.3) is converted into

$$(\ x \equiv 0 \mod p_i \wedge p_i < x) \vee (M_x \equiv 0 \mod p_i \wedge p_i < M_x). \quad (2.5)$$

The recursive sieve (2.5) is a perfect tool; with this tool, we may delete exponents of all non-Mersenne primes and leave exponents of all Mersenne primes. So that we only need to determine the number of all Mersenne primes $|T_e|$. If we do so successfully, then the parity obstruction, a ghost in a house of primes, has been automatically evaporated.

With the recursive sieve (2.5), each exponent of non Mersenne prime is deleted exactly once; there is need neither the inclusion-exclusion principle nor the estimation of error terms, which cause all the difficulty in normal sieve theory.

According to this sifting condition or 'sieve' we successively delete the set C_i of all numbers x, such that M_x is non-Mersenne prime with the least factor of Mersenne number M_{p_i} except itself or with the least normal prime factor $p_i > 2$ except itself,

$$C_i = \{x : x \in (A_i \cup (T_i \mod m_i)) \wedge ((x \equiv 0 \mod p_i \wedge p_i < x) \vee (M_x \equiv 0 \mod p_i \wedge p_i < M_x))\}.$$

but remain the survivor x if $p_i = x$ or $p_i = M_x$.

We delete all sets of exponents of non Mersenne numbers C_j with $0 \leq j < i$ from the set N of all exponents of Mersenne numbers and leave a sifted set

$$L_i = N \setminus \bigcup_{0}^{i-1} C_j. \tag{2.6}$$

In the above sifted set, for every number x, Mersenne number M_x contains neither normal prime $p < p_i$ nor Mersenne prime $M_p < M_{p_i}$ as a factor except itself.

We delete all sets of exponents of non-Mersenne numbers C_j and leave the end sifted set T_e, which is the set of all exponents of Mersenne primes

$$T_e = N \setminus \bigcup_{0}^{\infty} C_i.$$

The set A_i of survivors is a set of exponents of Mersenne primes or almost Mersenne primes, the candidates. If $a \in A_i$ and $M_a < p_i^2$, then M_a is a Mersenne prime.

Obviously, we have the relation

$$|A_i| \leq |A_{i+1}|.$$

From the recursive formula (2.1), we deduce again that the sifted set L_i is the union of the set A_i of survivors and the residue class $T_i \mod m_i$.

$$L_i = A_i \bigcup (T_i \mod m_i). \tag{2.7}$$

Now we intercept an initial segment T_i' from the above sifted set L_i, which is the union of the set A_i of survivor and the set T_i of least nonnegative representatives, then we obtain a new recursive formula

$$T_i' = A_i \bigcup T_i. \tag{2.8}$$

Except remaining all survivor x less than p_i in the initial segment T_i', both sets T_i' and T_i are the same.

For example

$$\begin{aligned} A_3 &= \langle 2,3,5\rangle. \\ T_3' &= \langle 2,3,5\rangle \cup \langle 1,7,11,13,17,19,23,29\rangle \\ &= \langle 2,3,5,1,7,11,13,17,19,23,29\rangle. \end{aligned}$$

Formula (2.8) expresses a recursively sifting process according to the sifting condition (2.5) and provides a recursive definition of the initial segment T_i'.

The following readers will see that the initial segment is a well-chosen notation, which makes mathematical reasoning itself easier or even purely mechanical.

We consider some properties of the initial segment $T_i^{'}$, and the limit of the sequence of the initial segments (T_i') to determine the set of all exponents of Mersenne primes and its cardinality.

The number of elements of the initial segment T_i' is

$$|T_i'| = |A_i| + |T_i|. \tag{2.9}$$

From formula (2.2) we deduce that the cardinal sequence $(|T_i'|)$ is strictly increasing

$$|T_i'| < |T_{i+1}'|.$$

Based on cardinal arithmetics we have

$$\lim T_i' = \bigcup |T_i'| = \aleph_0.$$

Based on order topology, obviously, we have also

$$\lim |T_i'| = \aleph_0. \tag{2.10}$$

Intuitively we see that the initial segment T_i' approaches the end-sifted set T_e, and the corresponding cardinality $|T_i'|$ approaches infinity as $i \to \infty$. Thus the end-sifted set, the set of all exponents of Mersenne primes is limit computable and is an infinite set.

We give a formal proof.

Let A'_i be the subset of all exponents of Mersenne primes in the initial segment T'_i,

$$A'_i = \{x \in T'_i : x \text{ is an exponent of Mersenne prime}\}. \tag{3.1}$$

Example,

$$\begin{aligned} A'_1 &= \langle 2 \rangle, \\ A'_2 &= \langle 2, 3, 5 \rangle, \\ A'_3 &= \langle 2, 3, 5, 7, 13, 17, 19 \rangle, \\ A'_4 &= \langle 2, 3, 5, 7, 13, 17, 19, 31, 61, 89, 107, 127 \rangle, \\ A'_5 &= \langle 2, 3, 5, 7, 13, 17, 19, 31, 61, 89, 107, 127, 521, 607, 1279, 2203, 2281 \rangle, \end{aligned}$$

We consider the properties of both sequences of sets (T'_i) and (A'_i) to prove Mersenne prime conjecture.

Theorem 3.1. *The sequence of the initial segments (T'_i) and the sequence of its subsets (A'_i) of exponents of Mersenne primes both converge to the set of all exponents of Mersenne primes T_e.*

First from set theory [5], next from order topology [8], we prove this theorem.

Proof. For convenience of the reader, we quote a definition of the set-theoretic limit of a sequence of sets [5].

Let (F_n) be a sequence of sets; we define $\limsup_{n=\infty} F_n$ and $\liminf_{n=\infty} F_n$ as follows.

$$\begin{aligned} \limsup_{n=\infty} F_n &= \bigcap_{n=0}^{\infty} \bigcup_{i=0}^{\infty} F_{n+i}, \\ \liminf_{n=\infty} F_n &= \bigcup_{n=0}^{\infty} \bigcap_{i=0}^{\infty} F_{n+i}. \end{aligned}$$

It is easy to check that $\limsup_{n=\infty} F_n$ is the set of those elements x, which belongs to F_n for infinitely many n. Analogously, x belongs to $\liminf_{n=\infty} F_n$ if and only if it belongs to F_n for almost all n, that is, it belongs to all but a finite number of the F_n.

London Journal of Research in Science: Natural and Formal

If

$$\limsup_{n=\infty} F_n = \liminf_{n=\infty} F_n,$$

we say that the sequence of sets (F_n) converges to the limit

$$\lim F_n = \limsup_{n=\infty} F_n = \liminf_{n=\infty} F_n.$$

From formula (2.6) we know that the sequence of sifted sets (L_i) is descending

$$L_1 \supset L_2 \supset \cdots \supset L_i \supset \cdots\cdots .$$

According to the definition of the set-theoretic limit of a sequence of sets, we obtain that the sequence of sifted sets (L_i) converges to the set T_e

$$\lim L_i = \bigcap L_i = T_e.$$

From definition (3.1) the sequence of subsets (A_i') is ascending

$$A_1' \subset A_2' \subset \cdots \subset A_i' \subset \cdots\cdots ,$$

we obtain that the sequence of subsets (A_i') converges to the set T_e,

$$\lim A_i' = \bigcup A_i' = T_e.$$

The initial segment T_i' locates between two sets A_i' and L_i

$$A_i' \subset T_i' \subset L_i.$$

It is easy to prove that the sequence of initial segments (T_i') converges to the set T_e

$$\lim T_i' = T_e.$$

In general, for any sequence of finite sets (G_i), if G_i locates between two sets A_i' and L_i,

$$A_i' \subset G_i \subset L_i,$$

then we have

$$\limsup G_i \subset \lim L_i,$$

$$\liminf G_i \supset \lim A_i'.$$

Thus

$$\lim G_i = T_e,$$

According to set theory, we have proved that both sequences of sets (T_i') and (A_i') converge to the set of all exponents of Mersenne primes T_e.

$$\lim T_i' = \lim A_i' = T_e.$$

Even $T_e = \emptyset$ the limit of set theory is valid too.

We can not use analytic techniques for limits of set theory, so that we try to endow them with an order topology and prove that according to order topology, both sequences of sets (T_i') and (A_i') converge to the set of all exponents of Mersenne primes T_e.

We quote J.R.Munkres's definition of the order topology [7][8].

Let X be a set with a linear order relation; assume X has more one element. Let $\mathbb{B}$ be the collection of all sets of the following types:

(1) All open intervals (a, b) in X.

(2) All intervals of the form $[a_0, b)$, where a_0 is the smallest element (if any) in X.

(3) All intervals of the form $[a, b_0)$, where b_0 is the largest element (if any) in X.

The collection $\mathbb{B}$ is a bases of a topology on X, which is called the order topology.

The empty or singleton is not a linear order $<$ set. There is no order topology on the empty set or sets with a single element.

The recursively sifting process formula (2.8) produces both sequences of sets together with the common set-theoretic limit point T_e.

$$\begin{aligned} \mathbf{X_1}: &\quad T_1', T_2', \ldots, T_i', \ldots\ldots; T_e, \\ \mathbf{X_2}: &\quad A_1', A_2', \ldots, A_i', \ldots\ldots; T_e. \end{aligned}$$

We further consider structures of both sets $\mathbf{X_1}$ and $\mathbf{X_2}$ using the recursively sifting process (2.8) as an order relation

$$\begin{aligned} i < j \to T_i' < T_j',\ \forall i(T_i' < T_e), \\ i < j \to A_i' < A_j',\ \forall i(A_i' < T_e). \end{aligned}$$

The set $\mathbf{X_1}$ has no repetitious term. It is a well ordered set with the order type $\omega + 1$ using the recursively sifting process (2.8) as an order relation. Thus the set $\mathbf{X_1}$ may be endowed an order topology.

In general, the set $\mathbf{X_2}$ may have no repetitious term or may have some repetitious terms or may be a set with a single element $\mathbf{X_2} = \{\emptyset\}$; in other words, $A_i' = \emptyset$ for all i.

London Journal of Research in Science: Natural and Formal

We have computed out 51 patterns of the first few exponents of Mersenne primes. The set $\mathbf{X_2}$ contains more than one element, it may be endowed an order topology using the recursively sifting process (2.8) as an order relation.

Obviously, for every neighborhood $(c, T_e]$ of T_e, there is a natural number i_0, for all $i > i_0$, we have $T_i' \in (c, T_e]$ and $A_i' \in (c, T_e]$. Thus both sequences of sets (T_i') and (A_i') converge to the set of all exponents of Mersenne primes T_e.

$$\begin{aligned} \lim A_i' &= T_e, \\ \lim T_i' &= T_e. \end{aligned}$$

According to order topology, we have again proved that both sequences of sets (T_i') and (A_i') converge to the set of all exponents of Mersenne primes T_e. We also have

$$\lim\ T_i' = \lim A_i'. \tag{3.2}$$

Only if $T_e = \emptyset$ under some sifting conditions, the set $\mathbf{X_2}$ only has a single element $\emptyset$, which has no order topology by definition. In this case, formula (3.2) is not valid, and we prove nothing by order topology.

In the last section, we shall discuss the existence of the order topological limits $\lim T_i', \lim A_i'$.

Theorem 3.1 and formula (2.10) reveal some particular order topological structures of the set of all exponents of Mersenne primes T_e on the sets $\mathbf{X_1}, \mathbf{X_2}$. Now we can prove that the set of all exponents of Mersenne primes is infinite set based on usual theorems of general topology.

Theorem 3.2. *The set of all exponents of Mersenne primes is infinite.*

We give two proofs.

Proof. A

We consider cardinalities $|T_i'|$ and $|A_i'|$ of sets on two sides of the equality (3.2), and order topological limits of cardinal sequences $(|T_i'|)$ and $(|A_i'|)$ with the usual order relation $\leq$, as both sets T_i' and A_i' tend to T_e.

From general topology, we know that if the limits of both cardinal sequences $(|T_i'|)$ and $(|A_i'|)$ on two sides of the equality (3.2) exist, then both limits are equal; if $\lim |A_i'|$ does not exist, then the condition for the existence of the limit $\lim |T_i'|$ is not sufficient [6].

London Journal of Research in Science: Natural and Formal

For exponents of Mersenne primes, the set T_e is nonempty $T_e \neq \emptyset$, the formula (3.2) is valid. Obviously, the order topological limits $\lim |A_i'|$ and $\lim |T_i'|$ on two sides of the equality (3.2) exist, thus both limits are equal

$$\lim |A_i'| = \lim |T_i'|.$$

From formula (2.10) $\lim |T_i'| = \aleph_0$ we have

$$\lim |A_i'| = \aleph_0. \tag{3.3}$$

Usually, let $\pi(n)$ be the counting function, the number of exponents of Mersenne primes less than n. Normal sieve theory, analytic number theory, is unable to provide non-trivial lower bounds of $\pi(n)$ due to the parity problem. Let n be a natural number. Then the number sequence (m_i) is a subsequence of the number sequence (n), we obtain

$$\lim \pi(n) = \lim \pi(m_i).$$

By formula (3.1), the A_i' is the set of exponents of all Mersenne primes less than m_i, and the $|A_i'|$ is the number of exponents of all Mersenne primes less than m_i, thus $\pi(m_i) = |A_i'|$. We have

$$\lim \pi(m_i) = \lim |A_i'|.$$

$$\lim \pi(n) = \aleph_0. \tag{3.4}$$

We directly proved the conjecture with the counting function $\pi(n)$.

Next, we give another proof by the continuity of the cardinal function in the above particular order topological space.

The continuous function is a morphism between topological spaces, which preserves the topological structures.

The continuity depends only on the topologies of its domain and range spaces.

Proof. B
Let $f : \mathbf{X} \to \mathbf{Y}$ be the cardinal function from the order topological space $\mathbf{X}$ to the order topological space $\mathbf{Y}$, such that $f(T) = |T|$.

$$\begin{aligned} \mathbf{X} &: \quad T_1',\ T_2',\ \ldots,\ T_i', \ldots\ldots;\ T_e, \\ \mathbf{Y} &: \ |T_1'|, |T_2'|, \ldots, |T_i'|, \ldots\ldots; \aleph_0. \end{aligned}$$

It is easy to check that for every open set $[\ |T_1'|, |d|), (|c|, |d|), (|c|, \aleph_0]$ in $\mathbf{Y}$ the preimage $[T_1', d), (c, d),\ (c, T_e]$ is also an open set in $\mathbf{X}$. According to the definition of continuity of a function, the cardinal function $|T|$ is continuous at T_e with respect to the above order topology.

$$|\lim T_i'| = \lim |T_i'|. \tag{3.5}$$

The order topological spaces are Hausdorff spaces. In Hausdorff spaces, the limit point of the sequence of sets (T_i') and the limit point of the cardinal sequence $(|T_i'|)$ are unique if both exist.

We have proved theorem 3.1, $\lim T_i' = T_e$, and formula (2.10), $\lim |T_i'| = \aleph_0$. Substitute both into formula (3.5); we obtain that the set of exponents of all Mersenne primes is infinite,

$$|T_e| = \aleph_0. \tag{3.6}$$

In the last section, we discuss the existence of the limits $\lim |T_i'|$ and $\lim T_i'$.

Without any estimation or statistical data, without the Riemann hypothesis, by the recursive sieve method, we reveal the recursive structure, set theoretic structure and order topological structure of the set T_e on sequences of sets. The well known theories of those structures allow us to prove the Mersnne prime conjecture.

In the first order formal system there is no such proof.
We proved that the set of exponents all of Mersenne primes is an infinite set. In other words we have proved that the Mersenne prime conjecture is true.

Theorem 3.3. *There are infinitely many Mersenne primes.*
By the Euclid–Euler theorem we also prove

Theorem 3.4. *There are infinitely many even perfect numbers.*

Similarly, we may prove the Fibonacci prime conjecture, in another paper, we discuss this conjecture.

IV. DISCUSSION

In general, we can not prove that the cardinal function on sequences of sets is continuous. . There is a counterexample, the Ross-Littwood paradox [12] [14].

For example: consider the limit of the sequence of sets, which have no pattern

$$T_i = \langle i+1, i+2, \ldots, 10i \rangle.$$

From set theory we know $\lim T_i = T_e = \emptyset$, thus $|T_e| = 0$. But we also have $\lim |T_i| = \lim 10i = \infty$ from real analysis. If the cardinal function is continuous, then there is a contradiction in real analysis, the empty has an infinite cardinality. In this case, one can only get up the continuity and says that there is no relation between the cardinality of the end sifted set $|T_e| = 0$ and the limit $\lim |T_i| = \infty$.

By the recursive sieve method, we have revealed that the set T_e of all exponents of Mersenne primes has the structure of a particular order topology

$$\lim T_i' = T_e.$$

So that we consider the conjecture in the particular order topological space, which is generated naturally by the recursively sifting process (2.8), rather than in real analysis, a quantitative model of prime sets or heuristics model.

We consider all sequences of finite sets (G_i), such that $A_i' \subset G_i \subset L_i$, they converge to the end sifted set T_e from set theory

$$\lim G_i = T_e.$$

We try to endow all set-theoretical convergences $\lim G_i = T_e$ with an order topology using the recursively sifting process (2.8) as an order relation, then construct a particular order topological space $\mathbf{G}$.

Here we must be careful about the existence of order topological limits.

First, according to the definition, there exists no order topology on the empty set or sets with a single element[7] [8].

Next, we quote topologist L.D. Kudryavtsev's the existence of limits of a function for $\lim |G_i|$.

If the space $\mathbf{X}$ satisfies the first axiom of countability at the point T_e and the space $\mathbf{Y}$ is Hausdorff, then for existence of the limit $\lim |G_i|$ of the cardinal function $|G_i|$, it is necessary and sufficient that for any sequence (G_i) , such that $\lim G_i = T_e$, the limit $\lim |G_i|$ exists. If this condition holds, the limit $\lim |G_i|$ does not depend on the choice of the sequence (G_i) , and the common value of these limits is the limit of $(|G_i|)$ at T [6].

Note, we consider the set sequences; the empty $\emptyset$ is as an element. If we find out at least one prime pattern, then the set sequence (A'_i) has more one element.

Only if the end sifted set is empty $T_e = \emptyset$, the limits $\lim A'_i$ and $\lim |A'_i|$ have no existence. The existence of all other limits $\lim G_i$, $\lim |G_i|$ is not sufficient from the above general topology. Thus at the point $T_e = \emptyset$, there is no "continuous" or "non-continuous". There is no contradiction. In this case, one needs no order topology.

If the end sifted set is not empty $T_e \neq \emptyset$, since the inclusion relation $G_i \supset A'_i$, the sequence (A'_i) has more one element, every sequence (G_i) has more one element, every limit of set theory $\lim G_i$ may be endowed with an order topology. Every limit of order topology $\lim G_i$ has existence, every limit of order topology $\lim |G_i|$ has existence. The condition of existence of $\lim |T'_i|$, $\lim T'_i$, $\lim |A'_i|$, $\lim A'_i$ is sufficient. Thus our proof of the theorem 3.1 and 3.2 is correct.

In the formal system $P(N)$ we deal with the Ross-Littwood paradox and find out a proof of the Mersenne prime conjecture in the particular order topological space.

The Ross-Littwood paradox shows that the restricted definition for order topology, assume X has more one element, is necessary.

We consider the set of various prime patterns T_e, in advance, we have known at least one prime pattern, and in advance, we have known that the end sifted set is not empty $T_e \neq \emptyset$.

By the same paradigm, we may predicate whether another prime pattern will persist for ever or not.

ACKNOWLEDGEMENT

I thank Kai Thompson for revising my errors of English.

REFERENCES

1. Chris K. Caldwell, Mersenne Primes: History, Theorems and lists.
2. Chris K. Caldwell, Heuristics: Deriving the Wagsta_ Mersenne Conjecture. The Prime Pages. Retrieved on 2014-05-11.
3. C. Pomerance, "Recent developments in primality testing," Math. Intelligencer, 3:3 (1980/81) 97{105. MR 83h:10015. 18
4. GIMPS Discovers Largest Known Prime Number: 282589933 _ 1. Retrieved 2019-01-01. https://www.mersenne.org/primes/press/M82589933.html
5. K.Kuratowsky and A. Mostowsky, set theory, With an introduction to descriptive set theory, North Holland Publishingcom.(1976) 118{12
6. [6] L.D. Kudryavtsev, Encyclopaedia of Mathematics, limit, [Online] Available: http://eom.springer.de/l/l058820.htm.
7. Jesper M. M_ller,General Topology web, math.ku,dk (2005)20
8. J.R. Munkres,Topology, (2rd ed.), Prentice Hall, Upper Saddle River, (2000), 84
9. Fengsui Liu, On the Sophie Germain Prime Conjecture. WSEAS Transactions on mathematics, l0 12 (2011), 421{430.
10. Fengsui Liu, There are in_nitely many Mersnne composite numbers with prime exponents. Advances in Pure Mathematics, 2018, 8, 686{698.
11. Fengsui Liu, Which polynomials represent in_nitely many primes. Global Journal of Pure and Applied Mathematics, Volume 14, Number 1 (2018), 161{180.
12. J.E.Littlewood,[1953], Littlewood's Miscellany, (ed. Bela Bollobas), Cambridge University Press, Cambridge, (1986), p.26.
13. M.D. Sautoy, The Music of the Primes , HarperCollins Publishers , (2003),p.26.
14. S.Ross, A First Course in Probability , (3rd ed.), New York and London, Macmillan,(1988)

This page is intentionally left blank

La Inversión Extranjera en México y en China, Análisis Comparativo del Marco Jurídico

Sanchez Ortiz, Alfredo

ABSTRACT

While economic factors play a key role in get the flows of capital from abroad to a host country, the legal and institutional aspects that influence this should not be overlooked; Such is the case of legal requirements and regulations. This article intends to explain the unequal foreign direct investment that China and Mexico have get since the beginning of reforms in 1980. This explan- ation is from the legal perspective, specifically the role that the laws have had in this process.

Keywords: inversión extranjera directa, estado de derecho, economía.

Classification: FOR CODE: 170202

Language: English

London Journals Press

LJP Copyright ID: 925623
Print ISSN: 2631-8490
Online ISSN: 2631-8504

London Journal of Research in Science: Natural and Formal

Volume 20 | Issue 3 | Compilation 1.0

La Inversión Extranjera en México y en China, Análisis Comparativo del Marco Jurídico

Sanchez Ortiz, Alfredo

RESUMEN

En este artículo se pretende dar una explicación a la captación tan desigual de inversión extranjera directa que China y México han tenido desde los inicios de las reformas en 1980, ya que ambas economías han considerado a la inversión extranjera como una de las fuentes para el desarrollo económico del país. Esta explicación es desde la perspectiva jurídica, específicamente del papel que las leyes han tenido en este proceso.

ABSTRACT

While economic factors play a key role in get the flows of capital from abroad to a host country, the legal and institutional aspects that influence this should not be overlooked; Such is the case of legal requirements and regulations. This article intends to explain the unequal foreign direct investment that China and Mexico have get since the beginning of reforms in 1980. This explanation is from the legal perspective, specifically the role that the laws have had in this process.

Palabras Clave: inversión extranjera directa, estado de derecho, economía.

I. INTRODUCCIÓN

En China y México las políticas de atracción de flujos de capital de inversión extranjera directa (IED)[1] no tuvieron un peso importante durante el periodo previo a la década de 1980; ambos la consideraban complementaria a los esfuerzos internos para lograr el crecimiento y el desarrollo económico. Hasta entonces habían mantenido un nacionalismo exacerbado: privilegiaron modelos económicos orientados hacia el mercado interno, levantaron barreras al flujo libre de capital y favorecieron procesos de industrialización con una fuerte intervención del Estado en la economía.

Aunque las grandes transformaciones de China y México surgieron casi al mismo tiempo, su naturaleza y trayectorias fueron divergentes: la transición china implicó no sólo un cambio en la estrategia de industrialización, sino una trans formación misma de las relaciones de propiedad y producción definidas por la dinámica de la competitividad y de la globalización. De ser China una economía cerrada, centralmente planificada y con una ineficiente asignación de sus recursos, se fue convirtiendo paulatinamente en una economía de mercado mixto (socialismo de mercado) y perfil industrial; a la vez que se pretendía abastecer al enorme mercado interno, anhelaba además, participar de manera creciente en tareas de mayor complejidad en la cadena de producción global. Para México la transición fue posterior al estallido de la crisis de 1982; con la reforma implementada, se pretendía dar respuesta a la crisis y poner las bases para una nueva dinámica de crecimiento.

Pareciera que en esta gran transformación operada por ambos países las condiciones para lograr el éxito eran más favorables para México que para China: sus fuertes vínculos económicos y comerciales con Estados Unidos y el resto del mundo capitalista, el respaldo del Fondo Monetario Internacional a las nuevas políticas de apertura comercial y liberalización económica, y el hecho de iniciar la aplicación de una reforma neoliberal en un momento en que las principales empresas industriales y financieras estaban en

[1] En el presente trabajo por IED hemos de entender "los flujos de stock de capitales por particulares o empresas de un país en otro conservando el derecho de propiedad de los activos, y con la capacidad de participar en el control y toma de decisiones de la empresa y del uso de su capital invertido".

London Journal of Research in Science: Natural and Formal

manos privadas o en proceso de privatización hacía más factible la aplicación de las nuevas políticas y preveía resultados óptimos a corto plazo[2]. China, en cambio, había iniciado su reforma sin que hubiera un sector privado amplio y fuerte; la mayoría de las empresas industriales propiedad del Estado eran ineficientes y se carecía de una estructura institucional capaz de sustentar las nuevas instituciones del mercado. A esos obstáculos habría que agregar la animadversión, sospechas y temores que despertaba la supuesta disponibilidad al cambio por parte del gobierno chino[3].

Contrario a lo que se esperaba, la atracción de capitales del exterior por China fue más exitosa que la experimentada por México. Si bien ambos se beneficiaron con los flujos de capital externo, y en cierto sentido ambos tuvieron un éxito relativo en la aplicación de sus políticas, los niveles de inversión en China han sido, por mucho, mayores a los alcanzados por México durante ese periodo. De 1989 a 2003 china capta el 6% de la IED mundial, en tanto que en México percibió el 40% de la IED que recibió china entre 1987 y 1994.

Está claro que la IED busca algún tipo de beneficio, sin embargo, en la elección de la ubicación y destino de la inversión, que importancia tiene el Estado de Derecho? Esta es la interrogante que guía el desarrollo de este trabajo.

II. ANTECEDENTES Y FUNDAMENTOS

2.1 Antecedentes en China

Las decisiones del gobierno chino de permitir una mayor inversión a partir de 1979 corresponden a transformaciones relevantes que se fueron sucediendo en el liderazgo político y en la política económica. Las transformaciones se iniciaron a finales de la Revolución Cultural y cristalizaron durante la tercera sesión plenaria del 11º Comité Central del Partido Comunista Chino en 1978, cuando se planteó la política de las "cuatro modernizaciones". agricultura, industria, ciencia y tecnología, y defensa nacional.

El principal propósito de estas cuatro modernizaciones fue cuadruplicar el PIB de China entre 1980 y el año 2000, además de elevar el estándar de vida de la población a través del crecimiento económico.

Para el cumplimiento de los objetivos previstos en la tercera sesión plenaria del 11º Comité Central del Partido Comunista se debieron realizar grandes transformaciones en todos los sectores: en la administración de las empresas, en el comercio exterior, en el sistema bancario, etc[4]. Como resultado de este pleno se establecieron el Ministerio de Comercio Exterior, el Ministerio de Relaciones Económicas Internacionales y Comercio (MOSFET), y el Comité Administrativo para la Inversión Extranjera como un organismo dependendiente. También, por primera vez se reconocieron las empresas conjuntas entre chinos y extranjeros y se introdujeron cantidades limitadas de IED en cuatro pequeñas zonas económicas especiales (ZEE) (Shenzhen, Zhuhai, Shantou y Xiamen).

Desde 1979, en la dinámica seguida para promover la IED se pueden distinguir seis etapas que se caracterizaron por los flujos realizados y por las diversas políticas que se fueron aplicando. En términos generales las etapas van desde los

[2] Durante este periodo México se había convertido en un lugar estratégico para el sistema internacional como sitio privilegiado para la inversión de capitales del exterior dadas las enormes expectativas que había despertado la firma de un Acuerdo de Libre Comercio con Estados Unidos y Canadá, amén de los recursos naturales disponibles, como el petróleo y el gas natural.

[3] Que para muchos fue confirmado en 1989 con la represión a los estudiantes chinos en la plaza de Tiananmen.

[4] De acuerdo con Mao Tsedong, China como país socialista no debía vincularse con la división internacional del trabajo porque hacerlo iría en detrimento del socialismo, pues las economías capitalistas dominaban y explotaban a las naciones en desarrollo. Por tanto, la inversión extranjera no era considerada prioritaria y sólo se le otorgaba una importancia residual. Sin embargo, con Deng Xiaoping la división internacional del trabajo no sólo proveía al país de los capitales necesarios para promover fuentes de empleo, sino que posibilitaba a la economía para hacerse de la tecnología y obtener el *know- how* necesario para transformar a China en un país desarrollado.

inicios de la reforma económica hasta nuestros días:

i) Etapa inicial (1979-1985): se inicia la IED en China.
ii) Etapa de desarrollo continuo (1986-1991): se alienta la IED en regiones selectivas.
iii) Etapa de crecimiento alto (1992-1996): se dispara la IED en China.
iv) Etapa de ajuste (1997 -2001): China sobrevive exitosamente a la crisis asiática y se orienta a su incorporación a la Organización Mundial de Comercio.
v) Etapa de consolidación (2002-2005): China se consolida como el principal país para la atracción de IED en el mundo, superando a los países tradicionalmente receptores.
vi) Etapa de reajuste (2006 en adelante): Consolidada China en la atracción de IED, se implementa una serie de medidas para limitar la participación de empresas extranjeras en el mercado doméstico; se trata de un cambio fundamental: de cantidad a calidad.

Los montos de inversión extranjera alcanzados en cada una de las etapas se pueden observar en el cuadro 2.

2.2 Antecedentes en México

Lo realizado por México en sus procesos de apertura a la IED no deja de ser contradictorio.Si bien es una dinámica que tiende hacia una apertura indiscriminada a los capitales del exterior, la apertura de los diversos sectores, tanto en China como en México, no fue homogénea. Los gobiernos que se han sucedido desde entonces conservaron para el gobierno y para los mexicanos diversos sectores considerados como estratégicos. De ahí el análisis de los tipos de IED y el marco legal que norma y regula la inversión de los actores nacionales y foráneos, así como la de los actores privados y gubernamentales.

La liberación económica mexicana fue consecuencia, en gran medida, de la crisis de 1982, que puso de manifiesto el agotamiento del modelo de Industrialización Sustitutiva de Importaciones (ISI) establecido en el país hasta esa fecha. Con posterioridad, las autoridades mexicanas apli caron distintos programas macroeconómicos para estabilizar la economía, controlar la inflación y reducir el déficit fiscal, y además se replanteó el modelo de crecimiento económico, para lo cual se puso en marcha una serie de reformas que permitieron el ajuste de los precios relativos para lograr una asignación de recursos más eficiente y contar con una estructura productiva capaz de participar y competir en los mercados internacionales. En esta dinámica, las exportaciones jugaron un papel preponderante en la estrategia del desarrollo económico mexicano.

Desde la Segunda Guerra Mundial y hasta principios de los años ochenta, la mayoría de los países latinoamericanos siguieron el modelo ISI, consistente en un conjunto de políticas para favorecer la industrialización dirigida por el Estado y la protección de la industria nacional mediante el apoyo a las empresas públicas y privadas nacionales. (Gary, 2005). [9]La ISI se fundamentaba en la convicción de que ciertas características latinoamericanas —entre ellas sus valores culturales y su estructura institucional— tornaban ineficaces los mecanismos del mercado en la región, así como la idea de que la apertura del mercado pondría en manos extranjeras un mayor control de la economía.

En la ISI, el Estado desempeñaba el papel central en el control de la economía, estableciendo la autosuficiencia económica y el desarrollo de la industria nacional como sus prioridades. Los gobiernos otorgaban mayor valor al desarrollo industrial que a los esquemas tradicionales de comercio agrícola y recursos primarios, y muchos pensaban que la acumulación gradual de capacidad industrial fomentada por esta estrategia mejoraría la posición de los países latinoamericanos en la economía mundial. A medida que avanzaron los años cincuenta y sesenta, las políticas ISI desplegaron un conjunto de características comunes: elevadas barreras arancelarias para los bienes extranjeros, en especial artículos industriales; monedas sobrevaluadas y, después de los años cincuenta,

cada vez más medidas para atraer capital extranjero.

En los años sesenta y setenta, las principales economías latinoamericanas pasaron de una fase de ISI primaria (centrada en bienes de consumo básicos como textiles, ropa, calzado y procesamiento de alimentos) a una ISI secundaria orientada a sustituir importaciones en una variedad de productos más avanzados, como los bienes de consumo duraderos (automóviles), bienes intermedios (petroquímicos y acero) y bienes de capital (maquinaria pesada). En esta década, Latinoamérica se hizo muy dependiente de los mercados de capital internacional para financiar el sector estatal, hasta que la deuda acumulada se derrumbó. Para los años ochenta, la ISI estaba en problemas en toda la región.

Refiriéndonos en concreto a la ISI en México[5], ésta incluyó un sistema de elevadas barreras arancelarias, la formación de monopolios operados por el gobierno en industrias como el petróleo y la electricidad, y la intermediación gubernamental en el financiamiento de las empresas comerciales. La sustentabilidad de tales directrices contó con el apoyo de las fuerzas políticas del país, dominadas por el Partido Revolucionario Institucional (PRI). Con el liderazgo del PRI, México tuvo un sólido crecimiento entre los años cincuenta y setenta, con una tasa de 6% anual y bajos índices inflacionarios. (fourcade-Gourinchas y Sara, 2002) Durante la década de los setenta, y hasta principios de los ochenta, las exportaciones petroleras y el endeudamiento externo permitieron sobrellevar la crisis estructural. Sin embargo, la incapacidad de continuar con este proceso de financiamiento fue puesta en evidencia en 1982, cuando condiciones externas (particularmente el masivo endeudamiento) requirieron por parte del gobierno mexicano la búsqueda de nuevas formas de financiamiento o incluso el replanteamiento del modelo de desarrollo seguido, lo cual puso fin al modelo ISI y condujo a importantes cambios en la estructura económica de la región (Dussel Peters 2000).

El deterioro de las condiciones macroeconómicas al final de los años setenta (bajo crecimiento, desigualdad económica creciente, crisis en la balanza de pagos de los gobiernos e hiperinflación periódica) favoreció la adopción de un enfoque más orientado al mercado, conocido como "Consenso de Washington", lo que llevó a implementar reformas económicas profundas encabezadas por un programa de ajuste y estabilización en las políticas fiscal y cambiaria, en concordancia con el decálogo del Consenso de Washington. De esta manera, las reformas debían ser consistentes con los dos objetivos del programa: saneamiento fiscal y estabilización macroeconómica. La reforma tributaria y las privatizaciones se orientaron a cumplir con la primera meta, mientras que la liberalización del comercio exterior, la desregulación y la liberación financiera tenían como objetivo alcanzar rápidamente la estabilización macroeconómica (Castillo 2007); es así como se implementa el neoliberalismo. Al principio, las políticas neoliberales se centraron en reformar los flujos de cuentas corrientes y cuentas de capital, y en controlar las volátiles tasas de inflación. (Weyland 2004) posteriormente la reforma se extendió hacia la reconfiguración del papel del Estado en la economía. En términos generales, las principales políticas del neoliberalismo económico en América Latina se pueden resumir en siete pasos.(Portes 1997).

a) Apertura al comercio internacional.
b) Privatización de empresas públicas.
c) Desregulación de bienes, servicios y mercados de mano de obra.
d) Liberalización de mercados de capital, incluidos fondos de pensiones privatizados.
e) Fomento de la disciplina fiscal basada en recortes drásticos del gasto público.

[5] De 1940 a 1970 este modelo fue relativamente exitoso en México, cuando el PIB real creció a una tasa anual superior a seis por ciento. Sin embargo, las causas por las que la economía mexicana no avanzó dentro del modelo ISI son muy variadas; entre algunas de ellas se señalan: a) Un elevado proteccionismo; b) Generosidad en los subsidios a la industria; c) Importantes concesiones fiscales a la importación de bienes de capital; d) Alto contenido importado de la producción manufacturera, y e) Incapacidad de la economía para generar divisas suficientes para el crecimiento.

f) Desmantelamiento y reducción de programas sociales apoyados por el Estado.
g) Fin de la política industrial de tipo ISI.

Las reformas neoliberales se extendieron por América Latina a diferente velocidad, pero terminaron estableciendo un mayor uso de los mecanismos de mercado en todos los países. Los gobiernos se abocaron a ajustar el valor de sus monedas y reducir drásticamente las barreras al libre comercio y los controles sobre el capital privado extranjero. Con estas reformas, América Latina tuvo un crecimiento económico moderado a principios de los años noventa, que se volvió más lento a finales de la década y principios de la siguiente, lo que generó nuevas críticas al modelo, controversia que persiste a la fecha (Peters 2000).

Al igual que en China, en México estas reformas fueron aplicadas en etapas: la primera, de 1982 a 1987, estuvo vinculada directamente con las negociaciones del gobierno con autoridades financieras internacionales sobre la crisis de la deuda, lo que trajo consigo nuevos controles sobre las políticas monetaria y fiscal, que se tradujeron en disminución del gasto público. Una segunda etapa introdujo cambios más drásticos, como una extensa privatización, reducción de las barreras al comercio y liberalización de las regulaciones de la inversión extranjera.

La reforma a la economía mexicana abarcó un amplio espectro de actividades: privatización de empresas estatales, desregulación económica, cambio en el trato a las inversiones extranjeras y apertura comercial acelerada. Las reformas buscaron colocar el sector privado como el eje central de la conducción económica, y se les confirió la capacidad de operar competitivamente en los mercados mundiales sin el apoyo gubernamental. Parte central de estas acciones fue la apertura del mercado interno al comercio internacional, la atracción de capitales del exterior vía inversión extranjera, una consecuente desregulación de la economía, una mayor privatización de las empresas públicas y la liberación financiera, todo ello complementado con el compromiso de mantener una política monetaria prudente, una política fiscal austera y la eliminación de créditos preferenciales. El cambio estructural se basó en seis líneas generales: i) apertura comercial; ii) modificaciones al marco regulatorio de las IED; iii) privatización de empresas públicas; iv) desregulación económica; v) modificación al marco regulatorio de la tenencia de la tierra, y vi) regulación de las prácticas monopólicas.

Los empeños en esa dirección, sobre todo a partir de la segunda mitad de los ochenta transformaron al país; en pocos años se pasó de una economía casi cerrada a una de las más abiertas al comercio y a la inversión extranjera. La injerencia del sector público en la economía cambió drásticamente, hacia el achicamiento del sector paraestatal y el desplazamiento de la inversión estatal a favor del mercado en la determinación de precios clave, como la tasa de interés, el tipo de cambio nominal y los precios de insumo básicos.

Como parte de la reforma, México abrió su comercio a mediados de la década de los ochentas, específicamente desde su adhesión al Acuerdo General sobre Aranceles Aduaneros y Comercio (GATT) en 1986 (Mattar 2000).

2.3 La Inversión Extranjera Directa

La IED es una dinámica clave en el desarrollo de integración, ya que puede crear vínculos estables y duraderos entre las economías. Ofreciendo a las empresas diversos canales, e instalaciones de producción más baratas, las cadenas mundiales de valor y acceso a nuevas tecnologías. Como tal, puede proporcionar un gran estímulo en los estados receptores así como en los estados de origen de la IED.

El continuo y creciente movimiento internacional de capital bajo la forma de inversión extranjera directa ha derivado en las últimas décadas en la aparición de multitud de enfoques que buscan justificación a las causas y destinos de estos flujos financieros. Los crecientes enfoques teóricos denotan la inexistencia de una explicación consensuada sobre los desencadenantes de tales

flujos. Algunos estudiosos habrán de enfocar su análisis para el estudio de la localización de la IED y sus determinantes al considerar como equiparables el libre comercio con la movilidad de los factores, al justificar los desplazamientos de los factores productivos (capital y trabajo) a través del comercio de bienes. Desde esta perspectiva es recurrente la adopción de los enfoques que se apoyan en las llamadas *teorías tradicionales* mediante las cuales se explica la localización de los capitales mediante las ventajas que resultan por los diferenciales en costos y tasas salariales (la teoría de las ventajas absolutas, de las ventajas comparativas, etc.). Por otro lado, destacan *enfoques más modernos*, que sin desechar las conclusiones que se desprenden de las teorías tradicionales puntualizan otros aspectos, como dotaciones relativas de factores de las distintas naciones, diferencias en productividad, el efecto del capital humano y de la infraestructura, etc.

Hay otros estudiosos que privilegian en sus análisis los aspectos micro, por lo que parten de las consideraciones particulares de las empresas para explicar los flujos de capitales al exterior. Por el contrario, hay también quienes observan esos flujos desde una perspectiva contraria (macro). Estos últimos consideran que los flujos de capitales están dados por los aspectos externos en los que la empresa se desenvuelve. Quizá para no dejar fuera algún aspecto relevante, otros teóricos consideran un enfoque ecléctico e integrador.

El inversionista, por supuesto, no actúa en el vacío. Las condiciones en los estados potencialmente huéspedes, incluida las decisiones de la ley o marco legal, juega también un papel importante en la toma de decisiones para la IED. En este contexto, ha aumentado el interés por el papel de las instituciones en la atracción de IED. Entendiendo por instituciones no solo las estructuras políticas, sino también el marco legal y su papel en las condiciones económicas.

La necesidad de incorporar en los modelos teóricos variables que impliquen la existencia de ciertas imperfecciones en los mercados derivó en la aparición de nuevas teorías, como las llamadas "nuevas teorías del comercio internacional", con la consecuente aparición de nuevas justificaciones a la localización de la IED. Desde esta perspectiva, las "imperfecciones" del mercado, en gran parte explican esos flujos. Habría que agregar, finalmente, la existencia de otras revisiones teóricas, como las que parten de la organización industrial, la teoría de las corporaciones transnacionales y la teoría estratégica.

Como se puede apreciar, no existe ninguna teoría que haya sido consensuada y capaz de explicar de una forma completa y satisfactoria la IED. Hemos de reconocer que resulta ilusorio tener una teoría única sobre el tema. Es un anhelo inalcanzable dado que la inversión es de esencia polifacética. Todos estos enfoques buscan responder al "cómo" y al "por qué" de los flujos de capital en el mundo.

Se dice que la IED esta incentivada a invertir cuando los derechos de propiedad, cumplimiento de contratos y seguridad de las personas están garantizados. Sin embargo, este estudio tiene como meta comprobar que el Estado de Derecho fomenta la IED, que el Estado de Derecho es un factor determinante para atraer IED independientemente de los beneficios que este tipo de inversión busca, se trata de evidenciar que la explicación de las teorías que señalan que el factor determinante y principal para la atracción de flujos de IED es la búsqueda exclusiva de beneficios o ventajas. Para evidenciar lo anterior demostramos empíricamente el caso de México y China en la atracción de flujos de IED, comprobando que el factor determinante en la atracción de flujos de IED, es el Estado de Derecho, y que China ha sido más exitosa que México en la atracción de dichos flujos, debido a que la intervención del Estado chino ha sido más determinante para garantizar y hacer valer el Estado de Derecho.

La literatura sugiere que las empresas participan en la IED con el fin de obtener beneficios de uso su propiedad o de una ventaja específica (por ejemplo, una tecnología) para producir en el extranjero; asegurar el acceso a una ventaja específica en el extranjero (por ejemplo, un

recurso natural, un nuevo mercado o trabajo); y la internalización de la producción o los servicios. Sostiene además, que la relación entre el Estado de Derecho, el crecimiento económico y desarrollo se basan en los incentivos que el Estado de Derecho crea para la inversión y el comercio. En consecuencia, de acuerdo a ello. La IED puede agruparse en cuatro tipos distintos:

A. La que busca recursos, impulsada por la ventaja comparativa en recursos naturales o mano de obra características del mercado (mano de obra barata o especializada).
B. La que busca Mercados, con el objetivo de llegar a mercados regionales para superar los obstáculos y barreras a las importaciones, como la regulación de costos de transporte.
C. La que busque eficiencia y que tiene como objetivo la competitividad, aplicando una estrategia más rentable de integración transfronteriza de la producción.
D. La que busca activos o adquisiciones con el propósito de promover los objetivos estratégicos (por ejemplo, emprender I + D beneficioso).

Se ha intentado medir el impacto de los factores relacionados con el Estado de Derecho en las decisiones de los inversionistas, de la siguiente forma:

A. Principalmente en algunas determinantes, como los niveles de crecimiento económico, salarios y tamaño del mercado, encontrar preferencias para la inversión con economías y mercados y mano de obra relativamente barata.
B. Otros estudios examinan el papel del Estado anfitrión en los ámbitos económicos y políticos, así como tasas impositivas, control de capital y la liberación.

A pesar de algunos resultados mixtos, las investigaciones indican generalmente que los inversionistas se guían hacia mercados de capitales y políticas que fomentan el comercio. Muchos de estos estudios en este campo han adoptado un enfoque econométrico, para analizar grandes conjuntos de datos y buscar correlación entre el cumplimiento del Estado de Derecho y los flujos de IED.

Ahora bien, el Estado de Derecho es un concepto multifacético. A la fecha ha habido relativamente poca investigación sobre cómo los diferentes aspectos o factores del estado e derecho afectan a la IED. Como resultado, la literatura existente solo presenta una variedad de la evidencia sobre el impacto del Estado de Derecho en las inversiones, crecimiento y desarrollo. En varios documentos de las Naciones Unidas encontramos declaraciones claras y conexión positiva entre desarrollo económico y Estado de Derecho. En particular, en la Declaración de la Reunión de la Asamblea General de la ONU celebrada en septiembre de 2012, se establece que: El progreso del Estado de Derecho en lo nacional e internacional es esencial para una economía sostenida e inclusive para el crecimiento y desarrollo sostenible por lo que estamos convencidos de que esta interrelación debe ser considerada en la agenda de desarrollo internacional posterior a 2015 (ONU, 2012, 2)

Para las Naciones Unidas, el concepto de Estado de Derecho ocupa un lugar, se refiere a un principio de gobierno según el cual todas las personas, instituciones y entidades, públicas y privadas, incluido el propio Estado, están sometidas a unas leyes que se promulgan públicamente, se hacen cumplir por igual y se aplican con independencia, además de ser compatibles con las normas y los principios internacionales de Derechos Humanos. Asimismo, exige que se adopten medidas para garantizar el respeto de los principios de primacía de la ley, igualdad ante la ley, rendición de cuentas ante la ley, equidad en la aplicación de la ley, separación de poderes, participación en la adopción de decisiones, legalidad, no arbitrariedad, y transparencia procesal y legal.

En esta investigación se sostiene que, en el caso particular de los flujos de IED que han recibido México y China, estos han estado condicionados en gran medida al Estado de derecho, esto es, que la atracción de los flujos de IED, se han debido a las reformas y adecuaciones legales hechas en

ambas naciones. Por tanto las variables son las siguientes.

A. Variable independiente: reformas y adecua ciones legales aplicadas por el Estado.
B. Variable dependiente: flujos de IED.

III. MÉTODO

Para identificar la relación causal que presentan las variables dependientes e independientes, aplicamos la técnica estadística de la correlación, que determina la relación o dependencia que existe entre dos variables que intervienen en una distribución bidimensional. Ello para determinar si los cambios en una de las variables influyen en los cambios de la otra. En caso de que suceda, se dice que las variables están correlacionadas o que hay correlación entre ellas. Aplicamos esta técnica para conocer el tipo de relación que existe, básicamente entre las reformas legales llevadas a cabo en México y China, y los flujos de IED que cada uno de estos países ha atraído. Nos interesa cuantificar la intensidad de la relación lineal entre dos variables. El parámetro para ello es el coeficiente de correlación lineal de Pearson, cuyos valores oscilan entre –1 y +1. Por tanto cuanto más cerca estén los coeficientes de +1.0 y de -1.0, mayor o menor será (de acuerdo al signo) la fuerza de la relación entre las variables.

Coef. Pearson (r) representa el tipo de relación que existe entre las variables, considerando lo siguiente:

El valor del índice de correlación varía en el intervalo [-1,1], indicando el signo el sentido de la relación (Fernández, 1996):
Si r =1, existe una correlación positiva perfecta. El índice indica una dependencia total entre las dos variables denominada relación directa: cuando una de ellas aumenta, la otra también lo hace en proporción constante.

- Si 0 < r < 1, existe una correlación positiva.
- Si r=0, no existe relación lineal. Pero esto no necesariamente implica que las variables son independientes: pueden existir todavía relaciones no lineales entre las dos variables.
- Si -1< r < 0, existe una correlación negativa.
- Si r = -1, existe una correlación negativa perfecta. El índice indica una dependencia total entre las dos variables llamada relación inversa: cuando una de ellas aumenta, la otra disminuye en proporción constante.

El valor para la variable “Reformas Legales” se determinó (dado que no hay ningún estudio o estándar al respecto) tomando como base el alcance de la reforma respectiva asignado un puntaje de 0 a 1; se le asignó el valor de 1 uno para las reformas a la Constitución, en caso de que la reforma sea a una ley secundaria se les asigno el valor de 0.5. Los eventos y flujos de IED que se consideran son los que contienen los cuadros 1 y 2.

IV. ANÁLISIS Y RESULTADO

El cuadro 1 contiene la cronología de las reformas realizadas a la constitución y leyes secundarias realizadas en México y China en el periodo de 1980 al 2018, como ya se indico; el valor para la variable “Reformas Legales” se determinó considerando como base el alcance o impacto de la reforma en cuestión, asignando un puntaje de 0 a 1. El uno se asignó para las reformas a la Constitución y 0.5 para la reforma a la ley secundaria.

Cuadro 1: Cronología de los principales cambios legales en China y México de 1980 a 2018

Suceso en México	AÑO	Suceso en China
	1980	Reglamentos sobre zonas económicas especiales en la provincia de Guadong
	1981	Ley ISR sobre empresas extranjeras
	1982	Medidas Administrativas Provisionales Cobro de cuotas afluentes
	1983	
	1984	Aparición formal del mercado valores chino
	1985	
Entrada al GATT	1986	Principios generales del Derecho civil Se abre un mostrador de intercambio de Acciones
	1987	
Reforma al artículo 127 constitucional, Programa de reestructuración industrial. Establecimiento del impuesto al activo de las empresas para aumentar la renta pública	1988	Primer reforma constitucional en el Artículo 14
Decreto automotriz para modernización mediante su apertura a la competencia internacional. Apertura al capital extranjero, se reducen los procedimientos advos. Para la IED	1989	
	1990	Reforma de ley de la RPC sobre Joint Ventures Equitativos Chino Extranjeros
Reforma de las leyes de protección intelectual (extensión por 2 años en la duración de las patentes)	1991	
	1992	
Se emite la ley de Inversión Extranjera	1993	Segunda Reforma Constitucional Artículo 15
Inicio del TLCAN	1994	Ley de comercio exterior
La ley de Inversión Extranjera se modificada (Liberación comercial. Disminución de tasas arancelarias, aumento de la inversión del sector exportador. Programas de apoyo a las exportaciones no petroleras.) Se crean programas de apoyo a las exportaciones del sector público en las transacciones comerciales del exterior.	1995	ley de bancos comerciales
	1996	
	1997	
	1998	Reforma del sistema de regulación financiero

	1999	Se realiza la Tercera reforma constitucional (ley de empresas de propiedad intelectual)
	2000	
	2001	China ingresa a la Organización mundial de comercio
	2002	
	2003	Se establece una comisión regulatoria bancaria
Firma del Tratado de Libre Comercio con Japón	2004	Reforma a la ley de empresas de la RPC
	2005	Reforma a la ley de empresas de la RPC
	2006	Modificación a la ley de sociedades empresariales
Firma del Tratado de Libre Comercio con la Unión Europea.	2007	Se promulgan la Ley de propiedad Y Ley Antimonopolio de la RCP
	2008	
	2009	
	2010	
La ley de Inversión Extranjera es modificada Se crean acuerdos para la Promoción Recíproca de las Inversiones (APPRIS)	2011	
	2012	
	2013	Reformas económicas y sociales en el Tercer pleno del 18 Comité del partido Comunista Chino
	2014	El gobierno central lanzó políticas para acelerar la transformación y el desarrollo innovador de las zonas y para el desarrollo económico y tecnológico a nivel estatal, así mismo emitió criterios para acelerar el desarrollo de la ciencia y de servicios de tecnología, y para fomentar la inversión extranjera en servicios de manufactura y alta tecnología avanzada.
Zonas Económicas Especiales	2015	
Ley en IED 2020	2018	Reforma a la Ley de IED

Fuente: Elaboración propia.

Cuadro 2: Montos de IED en China y en México de 1980 a 2018

IED US$ Mil millones	IED en MÉXICO	Año	IED en CHINA	IED US$ Mil millones
	Primera etapa Reconversión económica con crisis e inestabilidad		Primera etapa Periodo de emergencia e inicio de las grandes transformaciones	
0.85		1983		0.92
0.75		1984		1.42
0.9		1985		1.96
1.2		1986		2.24
1.6		1987	Segunda etapa Fase de desarrollo continuo y reajuste	2.31
2.4	Segunda etapa Recuperación de la confianza	1988		3.19
2.8		1989		3.39
2.6		1990		3.49
4.7		1991		4.37
4.3		1992	Tercera etapa Fase de alto crecimiento	11.01
4.3		1993		27.52
10.9		1994		33.77
9.5	Tercera Etapa Crisis	1995		37.52
9	Cuarta etapa De la crisis a la estabilidad	1996		41.70
13		1997	Cuarta etapa Etapa de ajuste	45.26
12		1998		45.46
14		1999		40.32
18.3		2000		40.71
30	Quinta etapa Recuperación de la confianza	2001		46.85
24		2002	Quinta etapa Etapa de consolidación	52.74
18.2		2003		53.51
24.9		2004		60.60
25.9		2005		72.54
21		2006		72.71
32	Sexta etapa Recesión y Crisis	2007	Sexta etapa Recesión y Recuperación	83.52
29		2008		108.3
17.8		2009		95.0
26.4		2010		114.7
23.6		2011		123.9
20.4	Séptima etapa	2012	Séptima etapa	121
45.8		2013		123.9
25.6		2014		128.5
30.2		2015		135.6
30		2016		134
30		2017		136
32		2018		139

Fuente: Elaboración propia en base al World Investment report (varios años), de las Naciones Unidas, Nueva York y Ginebr

Cuadro 3: Principales normas que rigen la IED en China y México

China	México
Ley de Inversión Extranjera Directa (2019)	Ley de inversión Extranjera directa
Ley para el establecimiento y desarrollo de empresas conjuntas Chino-Extranjeros	
La ley de la República Popular China sobre contractos Joan Ventures Chino-Extranjeros y su reglamento y aplicación	Reglamento de la ley extranjera directa y del registro nacional de inversión
La ley de la República Popular de China para empresas con propiedad total de Extranjeros (EPE).	Resolución general de comisión nacional de inversión extranjera
Reglamento de Ley de la República Popular de China para empresas con propiedad total de Extranjeros (EPE).	Ley del Impuesto sobre la Renta
La ley de impuesto sobre la renta de la República Popular y su reglamento de aplicación.	
Normas provisionales del Ministerio de Comercio en la Inversión de Capital de Empresas con Inversión Extranjera.	
Disposiciones sobre el encauzamiento de la orientación de la inversión extranjera; Guía para las industrias con inversión extranjera; catálogo de ramas de producción favorecidas para la inversión extranjera.	
Ley de la República Popular China para la Protección de las Inversiones de los compatriotas de Taiwán y su reglamento de aplicación.	
Disposiciones para el establecimiento de sociedades de inversión por inversionistas extranjeros.	
Disposiciones sobre fusiones y adquisiciones de una empresa nacional por inversores extranjeros.	
Medidas de inversión estratégica para inversores extranjeros en sociedades cotizadas.	
Reglamento provisional sobre reinversión.	

Fuente: Elaboración propia en base a Invest in China. (2016), Oficina Económica y Comercial de España (2019).

Como se observa en el cuadro 3, a diferencia de México, el marco legal que rige la inversión en la República Popular China, sigue siendo más restrictiva, que en México. Considerando únicamente la legislación básica para la IED en China hay 14 leyes y/o reglamentos mientras que en México solo existen 4. En ese sentido, las autoridades chinas han promulgado más de 200 disposiciones, entre leyes y reglamentos, que regulan, complementan y modifican esas leyes. Mientras el gobierno mexicano promueve la inversión extranjera directa mediante el libre aprovechamiento de las ventajas disponibles sin privilegiar con políticas particulares a ningún sector y enlista las actividades reservadas al Estado, o sólo a los mexicanos y aquellas sujetas a límites máximos de participación de IED, el gobierno Chino ha promulgado una "Guía de Inversiones" con el fin de adaptar la inversión extranjera a su plan de desarrollo económico y social. En esa guía, además de establecer las inversiones alentadas, permitidas y prohibidas, se presentan los incentivos y estímulos que se ofrece según sea el tipo de inversión. Con ello guían "administrativamente" la inversión hacia los sectores que consideran prioritarios.

En este mismo sentido, se han elaborado y aprobado un catálogo para "Sectores Ventajosos para Inversiones Extranjeras en las Regiones Central y Occidental". En dicho catálogo se especifican los mismos estímulos que se ofrecen a

empresas "alentadas". Estos estímulos se concretan en impuestos fiscales favorables, facilidades para importación de equipo, partes, repuestos y tecnología.

En comparación con México, donde desde un inicio, se practica el principio de "trato nacional para inversionistas extranjeros", en China los inversionistas extranjeros que desean establecer sus empresas o abrir oficinas representativas requieren obtener permisos del gobierno central y local, así como obtener otros registros comerciales. De acuerdo con las leyes vigentes en China, el Estado adopta un sistema de clasificación administrativa para la IED. Las provincias, municipalidades, regiones autónomas y ciudades, como unidades independientes, tienen la autoridad de examinar y aprobar inversiones menores a 30 millones de dólares en aquellas áreas permitidas o alentadas por el Estado. Cuando una inversión excede este monto deberá ser aprobada por la Comisión de Planeación de Desarrollo Económico o por la Comisión Estatal de Economía y Comercio, esto no sucede o está regulado en México.

En referencia a los derechos de propiedad, de acuerdo con la Constitución China, sólo se les puede otorgar a los inversionistas el derecho de "uso" sobre la propiedad inmobiliaria y se les niega el derecho de propiedad total[6]. En México, en cambio, los inversionistas no tienen restricción alguna para la adquisición directa o indirecta de inmuebles, sea para propósitos residenciales, industriales o comerciales; la Constitución expresamente protege el "derecho o garantía de propiedad" en su artículo 27. Si bien, este artículo tiene dos restricciones particulares a este derecho: los extranjeros no pueden adquirir "directamente" la propiedad de inmuebles localizados en una faja de 100 kilómetros a lo largo de las fronteras y 50 kilómetros en las playas; en este caso, el dominio sobre los inmuebles se puede adquirir a través de un "fideicomiso", o a través de una sociedad mexicana con la totalidad de capital extranjero. Asimismo, ni los extranjeros ni los mexicanos pueden adquirir mayores extensiones a la pequeña propiedad cuando se trate de tierras agrícolas, ganaderas o forestales.

En México, en general, no se da un tratamiento preferencial a empresas extranjeras por su giro industrial, ubicación geográfica o niveles de desempeño, Con excepción de las Zonas Económicas Especiales, que recientemente fueron instauradas (31 de mayo de 2016) mediante la Ley Federal de Zonas Económicas Especiales, esta ley es para el gobierno el marco jurídico para lograr un desarrollo armónico y ofrecer un entorno de negocios excepcional para atraer inversiones en las Zonas Económicas Especiales,

Las Zonas Económicas Especiales son áreas geográficamente delimitadas y ubicadas en sitios con ventajas naturales y logísticas para convertirse en zonas altamente productivas. Estas regiones gozan de condiciones especiales para su desarrollo, tales como incentivos, infraestructura y beneficios fiscales y laborales. En el caso de China hay un tratamiento diferenciado a empresas extranjeras según sea el tipo de bienes (de baja, mediana o alta tecnología), destino de los bienes (al mercado doméstico o a las exportaciones), la situación que guarde (permitida o alentada), su ubicación regional y su destino final (ver cuadros 1 y 2).

[6] El gobierno asigna ese derecho por una contraprestación en dinero. Este derecho es limitado a 70 años para propósitos residenciales, 50 años para industriales y 40 para comerciales o turísticos. El titular del derecho puede enajenarlo o arrendarlo.

Grafica 1:

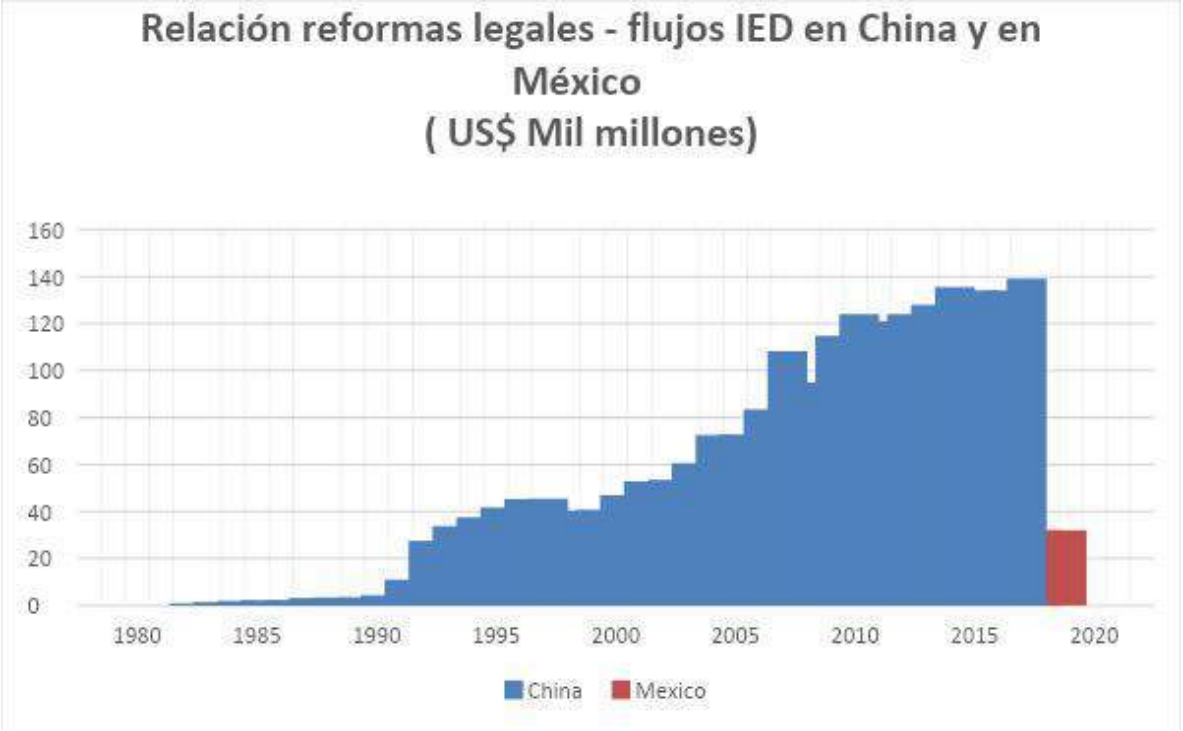

Fuente: Elaboración propia en base a World Investment report (Varios años) e Invest in China.

La relación Reformas Legales y flujos de IED que se evidencia en la Grafica 1 son los datos contenidos en los cuadros 1 y 2. En esta gráfica se presentan los datos de flujos de IED que entraron a China y México de 1980 a 2018 (cuadro 2).

Se observa que del periodo de 1980 a 1990 no existía una diferencia en flujos de IED tan notable entre China y México sino hasta a partir de 1992 donde las diferencias empiezan a ser considerables e inicia el despunte en materia de flujos de inversión extranjera que percibe China en relación con México, donde México mantiene la entrada de IED en parecidas dimensiones desde 2001. China por el contrario mantiene un perfil de aumento en la entrada de IED desde 2001.

De la relación entre las reformas legales y los flujos de IED, que se observa en el grafico I se establece que esta relación es básicamente de causa – efecto para el caso de China. Aunque como es lógico, los efectos no son de inmediato, dado que las reformas tardan en tener sus efectos, que en este caso fue prácticamente una década para que los flujos de IED fueran notoriamente estimulados por las reformas emprendidas en China. Para el caso de México, que no se realizaron el mismo número de reformas o adecuaciones legales, y estas, además no se hicieron de forma comprehensiva ni gradual, entonces, en la misma medida la IED respondió a este tipo de estímulo en la misma forma e intensidad en que las reformas se hicieron.

Al efectuar la correlación entre las reformas legales y flujos de IED, observamos que en efecto si existe correlación entre estas dos variables; en China el coeficiente de correlación es de 0.9260 y la correspondiente a México es de 0.8526.

V. CONCLUSIÓN

Del análisis aquí hecho, se puede concluir que existen marcadas diferencias en el marco normativo que rige la inversión extranjera en China y en México. En términos generales se aprecia una mayor "bondad" en la regulación mexicana, sin embargo, observamos que China tiene un estado de derecho consolidado a diferencia de México, y además:

1.- El gobierno chino llevo a cabo:

i) Una reforma tributaria favorable para la inversión foránea en sectores prioritarios.
ii) Creación de zonas económicas especiales para la producción y exportación con preferencias arancelarias, la creación de zonas de desarrollo, el establecimiento de ciudades costeras y triángulos de desarrollo.
iii) Aplicación de Incentivos Fiscales para inversión y desarrollo de infraestructura.

2.- El gobierno mexicano dejo en los sectores privados domésticos y foráneos la decisión de invertir, aplico programas de fomento a las exportaciones e impulso un limitado apoyo fiscal.

3.- Como se puede deducir de la gráfica 1, China ha sido comprehensiva en cuanto a la regulación de la IED, se observa que en la década de los 80 china realiza las adecuaciones legales necesarias para atraer flujos de IED, modificaciones que resultan en una complete transformación al Sistema legal. China prácticamente durante toda la década de los 80 se dedica a crear las bases o "cimientos" que le permitirán crear la estructura legal para garantizar y dar confiabilidad a la IED tal y como lo maneja la NEI. Estas bases legales permitieron atraer grandes flujos de IED a partir de la siguiente década, esto es de 1990. En el caso de México no se creó la infraestructura o "cimientos" que permitieran crear la infraes tructura necesaria para atraer los flujos de inversión, observamos que México realiza sus adecuaciones al marco jurídico una década después de cuando China lo hizo, década en la que china ya estaba recibiendo los frutos de la implementación de las medidas pertinentes con lo que México llega tarde y es esta una de las causas (independientemente del tamaño del Mercado, que de acuerdo con estudios empíricos ha tenido un gran impacto en la atracción de IED), por las que México quedo rezagado respecto a China en cuanto a la tracción de flujos de IED.

4.- Las leyes en México buscan promover la inversión extranjera y evitar restricciones adicionales, como permisos previos para iniciar los proyectos; además, no se debe cumplir con una regulación especial, pues los procedimientos que se aplican a los inversionistas mexicanos igualmente se aplican a los extranjeros, Mientras que China si tiene condiciones y restricciones para la IED. China atrae 5 veces más flujos de IED que México, lo cual explica que la fortaleza del Estado de derecho -además del tamaño de mercado- es un factor determinante en la atracción y destino de dichos flujos.

BIBLIOGRAFÍA

1. Chipman y Qian. (2018). El catálogo de 2017 de inversión extranjera de China abre acceso a nuevas industrias: en China Briefing, abril de 2018. Recuperado de: https://www.china-briefing.com/news/el-catalogo-de-2017-de-inversion-extranjera-de-china-abre-acceso-nuevas-industrias/
2. Enrique Dussel Peters (2000). La inversión extranjera directa en México. Santiago de Chile: CEPAL – ECLAC.
3. Fernández S, Pita y Pértega Díaz S. (1996). Unidad de Epidemiología Clínica y Bioestadística. Utilización e Interpretación de las Técnicas de Correlación disponible. Complexo Hospitalario Juan Canalejo. A Coruña (España). Disponible en https://www.fisterra.com/gestor/upload/guias/var_cuantitativas2.pdf.
4. Fourcade-Gourinchas, Marion y Sarah L. Babb (2002). The Rebirth of the Liberal Creed: Paths to Neoliberalism in Four Countries. American Journal of Sociology, núm. 108, vol. 3. pp. 533-579.
5. Gary Gereffi. (2005). The global economy: Organization, governance, and development. pp. 160-182, en Neil J. Smelser y Richard Swedberg (comps.).The Handbook of Economic Sociology, 2a. ed., Princeton, NJ: Princeton University Press and Russell Sage Foundation.
6. Guzmán, Alenka y Toledo, Alejandro. (2005). Competitividad manufacturera en México y China en el mercado estadounidense. Economía UNAM, núm. 4. Recuperado de

http://www.revistas.unam.mx/index.php/ecu/article/view/2823.
7. Invest in China. (2016). China Ministry of Commerce People´s Republic of China. Number 13267. Ministry of Commerce People´s Republic of China. Recuperado de: http://www.fdi.gov.cn/1800000121_10000161_8.html.
8. Máttar, Jorge (2000). Inversión y crecimiento durante las reformas económicas, en Clavijo, Fernando (2000) Reformas Económicas en México 1982 – 1999. El Trimestre Económico 92. México: Fondo de Cultura Económica, pp. 156 – 256.
9. Weyland, Kurt. (2004). Assessing Latin American neoliberalism: Introduction to a debate. Latin American Research Review, núm. 39, vol. 3, pp. 143-149.
10. López, José Francisco. (2019). Guía para calcular e interpretar el IDH. Economipedia: Haciendo fácil la economía. Recuperado de: https://economipedia.com/guia/guia-para-calcular-e-interpretar-el-idh.html
11. Lu, Ding y Tang, Zhimin. (1997). State intervention and business in China. the role of preferential policies. UK: Cheltenham. pp. 68-70. Recuperado de:http://www.ssina.com/news/releases/pdf_releases/20081014_report.pdf
12. Matthews, R. C O. (1986). 'The Economics of Institutions and the Sources of Economic Growth', Economic Journal. 96. 903-18. En Vargas Hernández, José Guadalupe. (2005). Análisis de Fundamentos De La Teoría Institucional. Revista Digital Universitaria. Volumen. 6 Número 8. ISSN: 1067-6079. Agosto.
13. Ministry of Commerce of the People's Republic of China. Brief Statistics on China's Direct Investment Overseas in 2019. Disnponible en *http://www.fdi.gov.cn/index.htm.*
14. North, Douglas. (1990) A transaction cost theory of politics. Journal of Theoretical Politics, Cambridge: Cambridge University Press, 2 (No. 4), 355-367 pp. En Vargas Hernández, José Guadalupe. (2005). Análisis de Fundamentos de la Teoría Institucional. Revista Digital Universitaria.Volumen.6 Número 8. ISSN: 1067-6079. Agosto.
15. Oficina Económica y Comercial de España (2019). Guía de incentivos a la implantación en México 2019. ICEX España Exportación e Inversiones. Recuperado de: https://www.icex.es/icex/es/navegacion-principal/implantacion-e-inversion-exterior/informacion-para-invertir-en-el-exterior/guias-incentivos/DOC2015505665.html.
16. Organización de las Naciones Unidas (2012). Declaración de la reunión de alto nivel de la Asamblea General sobre el estado de derecho en los planos nacional e internacional. Consultado en https://undocs.org/es/%20A/RES/67/1.
17. Portes, Alejandro (1997). Neoliberalism and the sociology of development: Emerging trends and unanticipated facts. Population and Development Review, núm. 23, vol. 2, pp. 238.
18. Rowat, Macolm; Malik, Waleed y Dakolias, María. (1995). Judicial Reform in Latin America and the Caribbean. Proceedings of the World Bank Conference, Documento Técnico del Banco Mundial 280. En Vargas Hernández, José Guadalupe. (2005). Análisis de Fundamentos De La Teoría Institucional. Revista Digital Universitaria.Volumen. 6 Número 8. ISSN: 1067-6079. Agosto.
19. Secretaría de Economía. (2012). Inversión Extranjera Directa en México y el Mundo. México: noviembre. Recuperado de: http://www.economia.gob.mx/files/comunidad_negocios/ied/analisis_publicaciones/Otros%20estudios/carpeta_informacion_estadistica_1115.pdf
20. Secretaría de Economía. (2015). Inversión Extranjera Directa en México y el Mundo. México: abril. Recuperado de: http://www.economia.gob.mx/files/comunidad_negocios/ied/analisis_publicaciones/Otros%20estudios/carpeta_informacion_estadistica_0415.pdf
21. Secretaría de Economía. (2019). Inversión Extranjera Directa en México y el Mundo. México: abril. Recuperado de: https://www.

gob.mx/cms/uploads/attachment/file/465562/Carpeta_IED_2019-1T.pdf
22. UNCTAD, World Investment Report, Foreign Direct Investment and the Challenge of Development. United Nations, Nueva York y Ginebra, 1999.
23. UNCTAD. (2019). World Investment report 2019: Transnational Industries and development. Nueva York y Ginebra: Naciones Unidas. Recuperado de: http://unctad.org/en/Publications Library/wir2016_en.pdf
24. Vargas Hernández, José Guadalupe. (2005). Análisis de Fundamentos De La Teoría Institucional. Revista Digital Universitaria. Volumen. 6 Número 8. ISSN: 1067-6079. Agosto.
25. Wei, Yegua Dennis. (2000). Regional Development in China. States, Globalization, and Inequality. Routledge Studies on China in Transition, No.115-116.

This page is intentionally left blank

Cosmic Ray Origins: Part 1. Frequency Upshifting of Light Rays/Electromagnetic Radiation Near Stars in Dynamic Universe Model

Satyavarapu Naga Parameswara Gupta (snp Gupta)

ABSTRACT

The high Energy Cosmic Rays can have multiple origins. In this paper we will consider their origins due to Frequency Upshifting of distant electro- magnetic radiation coming from distant galaxies or the radiation coming from stars inside the Milkyway, by using the Dynamic universe Model.

We will see a simulation using a Subbarao path or Multiple bending of light rays, where a ray started at some star will go on bend and its frequency gets upshifted and gains energy at every star in its path. We also will present a table of types of stars that are existing in Milkyway which will be used in next subsequent papers.

Keywords: cosmic rays, origins of cosmic rays, dynamic universe model, sita calculations, multiple bending of light, frequency upshifting of electromagnetic radiation, subbarao paths.

Classification: FOR Code: 240102

Language: English

London Journals Press

LJP Copyright ID: 925624
Print ISSN: 2631-8490
Online ISSN: 2631-8504

London Journal of Research in Science: Natural and Formal

Volume 20 | Issue 3 | Compilation 1.0

Cosmic Ray Origins: Part 1. Frequency Upshifting of Light Rays/Electromagnetic Radiation Near Stars in Dynamic Universe Model

Satyavarapu Naga Parameswara Gupta (snp Gupta)

ABSTRACT

The high Energy Cosmic Rays can have multiple origins. In this paper we will consider their origins due to Frequency Upshifting of distant electro- magnetic radiation coming from distant galaxies or the radiation coming from stars inside the Milkyway, by using the Dynamic universe Model.

We will see a simulation using a Subbarao path or Multiple bending of light rays, where a ray started at some star will go on bend and its frequency gets upshifted and gains energy at every star in its path. We also will present a table of types of stars that are existing in Milkyway which will be used in next subsequent papers.

Keywords: cosmic rays, origins of cosmic rays, dynamic universe model, sita calculations, multiple bending of light, frequency upshifting of electromagnetic radiation, subbarao paths.

Author: Retd Assistant General Manager, Bhilai Steel Plant, Res 1B / Street 57 / Sector 8 / Bhilai 490008.

I. INTRODUCTION

There are multiple origins of Cosmic Rays. They originate outside solar system [1] or from distant galaxies [2]. In addition to the generally accepted sources of Cosmic rays like they originate from the supernova explosions of stars and Active galactic nuclei like blazar TXS 0506+056;(See for example, the data based on observations of neutrinos and gamma rays from Supernova explosions as observed by Fermi FGST in (2013) [3] & Active Galactic Nuclei produces Cosmic Rays observed from blazar TXS 0506+056 in 2018.[4][5]); Dynamic Universe Model proposes three additional sources like frequency upshifting of light rays, astronomical jets from Galaxy centres and occasional solar flares from sun or other stars in Milkyway.

How these cosmic rays acquire high energy and why they are intermittent, what are the stages of development of originated Cosmic rays will be discussed in subsequent next 12 papers or so. Every paper will have its mathematical back-ground and SITA calculation sheets and / or Subbarao path calculation sheets. We will discuss the origination of Cosmic Rays mostly outside Solar System and Milkyway also. We also know Cosmic rays are composed primarily of high-energy protons and atomic nuclei; they are of uncertain origin.

As we see above in the origins of Cosmic Rays there are three parts. Hence this original paper was divided into three papers as the simulations will be different for each paper. Hence those three additional sources for Cosmic Ray Origins are:

a. Frequency upshifting of light rays,
b. Astronomical jets from Galaxy centres
c. Occasional solar flares from sun or other stars in Milkyway

1.1. Composition

Cosmic Rays or Cosmic Radiation is different from electromagnetic radiation or photons. Photons are considered as massless for all practical purposes, (they have no rest mass) though there is a minute mass associated with these photons. These Cosmic Rays consisting of Protons, Helium and other higher elements with the electrons stripped

London Journal of Research in Science: Natural and Formal

off. This composition is confirmed by Fermi Space Telescope FGST Data [1]. They are not just positively charged ions of elements, but total electrons were missing from these nuclei. Composed primarily of high-energy protons and atomic nuclei, they are of uncertain origin. And Dynamic Universe Model proposes three different types of possible origins for these Cosmic rays.

Primary Cosmic rays originate outside of Earth's atmosphere.

Secondary Cosmic rays originate due to collisions with air and other particles in Earth's atmosphere and fall on Earth. Now on wards we will Refer Primary cosmic rays as Cosmic rays only.

Primary cosmic rays are about 99% (of which 89% are protons,9% are alpha rays, 1% are nuclei of other heavier elements, called HZE ions.[6]) are the nuclei of atoms without electrons and remaining 1% are electrons like beta particles. There is a minute fraction of positrons and antiprotons.

Electro magnetic radiation and frequency upshifting when the ray passes grazingly near a mass like Sun or planet. When the frequency is high enough like alpha, beta or gamma radiation will be formed. ("How these particles will particles will gain high energies and the mechanisms of such high energies acquisitions" will be covered in another paper.)

1.2. Energy

These Cosmic rays are at the higher end of the energy spectrum, it is generally believed in physics that relativistic kinetic energy is the main source of the mass-energy of cosmic rays. We will see how Dynamic Universe Model explains these higher energies.

The energies of the most energetic ultra-high-energy cosmic rays (UHECRs) have been observed to approach 3×10^{20} eV[7], about 40 million times the energy of particles accelerated by the Large Hadron Collider[8]. Most cosmic rays, however, do not have such extreme energies; the energy distribution of cosmic rays peaks on 0.3 gigaelectronvolts (4.8×10^{-11} J) [9]. The highest-energy detected fermionic cosmic rays are about 3×10^{6} times as energetic as the highest-energy detected cosmic photons. An Extreme-Energy Cosmic ray (EECR) is an UHECR with energy exceeding 5×10^{19}. The particles with estimated arrival energies above 5.7×10^{19} eV are extremely rare. It is about one such event every four weeks in the 3000 km² area surveyed by the observatory.[10].

1.3. Formation of Cosmic Rays

We discuss here what are the possible ways of formations of Cosmic rays according to Dynamic Universe Model:

The energy gained is "=1.0001850323435700E+00" and frequency upshifting is with a ratio "1.0001850323435700E+00". Surprisingly both are same. These formulae were derived by the author in his earlier papers as referenced below.[11], [12], [13] and [14].

1. d. The energy gain at each star is added to the existing energy possessed at present with the incoming electro-magnetic radiation. This radiation on the move will gain energy and continues its journey. After the radiation gains energy and its frequency get upshifted, this radiation may .....

1. d.1. Hit a planet or a star or any astronomical object

1. d.2. Travel into the vast empty space

1. d.3. Pass Grazingly at another star or planet and gains energy and its frequency gets upshifted and travel again. The cycle described in this point (d.3.) will gets repeated.

II. MATHEMATICAL BACKGROUND

The mathematics of Dynamic Universe Model is published and is available in many open access papers hence not repeated here. The following linear tensor equation (1) is the basis for all these calculations.

$$\Phi_{ext}(\alpha) = -\sum_{\substack{\beta=1 \\ \alpha\neq\beta}}^{N^{\gamma}} \frac{Gm_{\beta}^{\gamma}}{\left| x^{\gamma\beta} - x^{\gamma\alpha} \right|} - \sum_{\substack{\beta=1 \\ \alpha\neq\beta}}^{N^{\delta\gamma}} \frac{Gm_{\beta}^{\delta\gamma}}{\left| x^{\delta\gamma\beta} - x^{\delta\gamma\alpha} \right|}$$

This concept can be extended to still higher levels in a similar way. There are other variations of the mathematics used in some different applications like VLBI explanations. The above Equation is the main resourceful equation, which gives many results that are not possible otherwise today.

2.1 Case3. When the velocity of gravitational mass is not exactly opposite or exactly in the same direction to the incoming light ray:

In this case the gravitational field will act as some brake or enhance the energy of the incoming light ray depending on ***(Cos ϕ)*** of the velocity of gravitational mass relative to incoming radiation, where ***(ϕ)*** is the angle between the light ray and velocity of gravitational mass .

The gravitating mass is moving with a velocity $\boldsymbol{\mu}$ making an angle ***(ϕ)*** as the angle between light ray velocity of gravitating mass and applies brake on the photon. This is something similar to the case where the gravitational mass is fixed in position and the photon of the rest mass $\boldsymbol{E / c^2}$ is moving with velocity $\mu \, Cos \, \phi + c$

Hence the initial velocity of photon = $- \mu \, Cos \, \phi - c$. It's velocity is towards the gravitational mass. The photon is having a freefall. Its final velocity = $- \boldsymbol{\mu} \, Cos \, \phi - c - g_o t$ [where ***t*** is the time of flight of photon].

Initial Energy = $m \, (\mu \, Cos \, \phi + c)^2 / 2 = E \, (\mu \, Cos \, \phi + c)^2 / 2 \, c^2 = E \, (\mu^2 \, Cos^2 \, \phi + c^2 + 2\mu \, Cos \, \phi c) / 2c^2$

3.2. From excel sheet Derivation of equations for the effect of movement of gravitational mass on the frequency of the incoming light ray with c:

Energy due to Gravitation of Sun (or star) on the photon = $\boldsymbol{E_s}$ = Initial Energy = $m \, (\mu \, Cos \, \phi + c)^2 / 2 = E \, (\mu \, Cos \, \phi + c)^2 / 2 \, c^2 = E \, (\mu^2 \, Cos^2 \, \phi + c^2 + 2\mu \, Cos \, \phi \, c) / 2c^2$

Frequency of photon = $\boldsymbol{\vartheta = E / h \text{ or } E = h \, \vartheta}$

Energy due to Gravitation of Sun (or star) on the photon = $E_s = E \; g_o \; r / c^2$ = Initial Energy = $m \, (\mu \, Cos \, \phi + c)^2 / 2$ *vak 12102019 ?????*

Initial Frequency = = $E \, (\mu^2 \, Cos^2 \, \phi + c^2 + 2\mu \, Cos \, \phi c) / 2hc^2$

$= E \, (\mu \, Cos \, \phi + c)^2 / 2 \, hc^2$

Vak 18DEC 2019: ERRATA

The above equations which are in were wrong. This mistake happened while reducing the equation to derive "Initial Frequency = ϑi" *and* "Final Frequency = ϑo"*. This was found while doing calculations numerically in excel. There was a result mismatch.*

Now the error was corrected.

Sorry for the error, and the Author regrets the error

=snp.gupta 18DEC 2019

Initial Frequency = $\vartheta i = E \, (\mu \, Cos \, \phi + c)^2 / 2 \, hc^2$

- $\Rightarrow \; \vartheta i = E \, (\mu \, Cos \, \phi + c)^2 / 2 \, hc^2$
- $\Rightarrow \; \vartheta i \; 2 \, hc^2 = E \, (\mu \, Cos \, \phi + c)^2$
- $\Rightarrow \; (\vartheta i \; 2 \, hc^2) / (\mu \, Cos \, \phi + c)^2 = E = h \, \vartheta s$
- $\Rightarrow \; (\vartheta i \; 2 \, c^2) / (\mu \, Cos \, \phi + c)^2 = \vartheta s$ =*Start Frequency*

Energy due to Gravitation of Sun (or star) on the photon after freefall = E_f = Final Energy = $\frac{1}{2} \, (E / c^2)(- \mu \, Cos \, \phi - c - g_o t)^2 = \frac{1}{2} \, (E / c^2)(\mu^2 \, Cos^2 \, \phi + c^2 + g_o^2 t^2 + 2\mu \, Cos \, \phi \, g_o t + 2c g_o t + 2\mu \, Cos \, \phi c)$

Final Frequency = $\vartheta o = E \, (\mu^2 \, Cos^2 \, \phi + c^2 + g_o^2 t^2 + 2\mu \, Cos \, \phi \, g_o t + 2c g_o t + 2\mu \, Cos \, \phi c) / 2hc^2$

$= \frac{1}{2} \, (E / hc^2)(- \mu \, Cos \, \phi - c - g_o t)^2$

Final Energy = $\frac{1}{2} \, (E / c^2)(- \mu \, Cos \, \phi - c - g_o t)^2 = \frac{1}{2} \, (E / c^2)(\mu^2 \, Cos^2 \, \phi + c^2 + g_o^2 t^2 + 2\mu \, Cos \, \phi \, g_o t + 2c g_o t + 2\mu \, Cos \, \phi c)$

Final Frequency = $\vartheta o = 1 / [\frac{1}{2} \, (E / c^2)(- \mu \, Cos \, \phi - c - g_o t)^2]$

$= 1 / [\frac{1}{2} \, (E / c^2)(\mu^2 \, Cos^2 \, \phi + c^2 + g_o^2 t^2 + 2\mu \, Cos \, \phi \, g_o t + 2c g_o t + 2\mu \, Cos \, \phi c)]$

here $E = h \, \vartheta$ that means

$= \{ \; (2 \, c^2) / h \, (\mu^2 \, Cos^2 \, \phi + c^2 + g_o^2 t^2 + 2\mu \, Cos \, \phi \, g_o t + 2c g_o t + 2\mu \, Cos \, \phi c) \}$

III. WHAT ARE SUBBARAO PATHS OR MULTIPLE BENDING OF LIGHT RAYS?

Assume a light ray was emitted and coming from a distant Galaxy or star, that light ray passes grazingly with some other star or planet. Then four things will bound to happen…

a. It bends slightly in the gravitation field.
b. It gains energy while it bends.
c. Its frequency gets up-shifted when while it bends.
d. It travels further.

So, after bending the original light ray will be a different light ray with higher frequency. Then it may pass grazingly near another star. Near the Second star all the above 4 things will happen. Many of the light rays go diverted paths. But some paths will be constant for a while. When these bending's will happen multiple number of times, they will become "Subbarao's paths" or following "Multiple bending of light rays". When frequency gets up-shifted sufficient number of times they will become particles like muons or positrons or electrons.

This is how these cosmic rays originate. Because of the Dynamism built in the universe, none of the stars or planets will stay in positions for forming paths. Hence these "Subbarao's paths" or "Multiple bending of light ray paths" will never be constant. These paths will get disturbed always, and new paths will form.

That is the reason why a bunch of cosmic rays will appear and they will stop from that direction. The Cosmic rays will always be intermittent. The detailed discussion of this will form another paper with the proper simulations to prove the point.

4.1.10.1. Bending of Light Equations and Diagram Fig.1:

Bending always happen in a 2D plane only. For a ray coming in 3 dimensions, it will bend in a 2D plane containing the center of gravity of star and line of the light ray. Let's assume a light ray is coming from a distant star or a Galaxy. Let the light ray is passing Grazingly near a star or Sun.

For calculation purposes lets an imaginary set of 2D coordinate axis as shown in figure. (Note: For information: an absolute set of coordinate axis is not necessary.) Let the light ray is passing through (0,0) of the set of axes as defined now. Let it make an angle α with x axis. See fig.1 for visualizing details.

The light ray bends an angle θ due to gravitation of that Star at the point A. After bending it continues its journey via point B. Lets drop a vertical line at point B via point C, which is the intersection of vertical and an horizontal passing through point A. Now in the right-angle triangle ABC the angle BAC is $\alpha - \theta$. Now we can see clearly, that 'AB' the distance 'ct' travelled by electro-magnetic radiation in time t with velocity c is the diagonal.

In triangle ABC the distance travelled in x coordinate direction = $(x2-x1) = ct \cos(\alpha - \theta)$ and the distance travelled in y coordinate direction = $(y2-y1) = ct \sin(\alpha - \theta)$.

Therefore the coordinates of B = $(x2, y2) = [\{x1 + ct \cos(\alpha - \theta)\}, \{y1 + ct \sin(\alpha - \theta)\}]$.

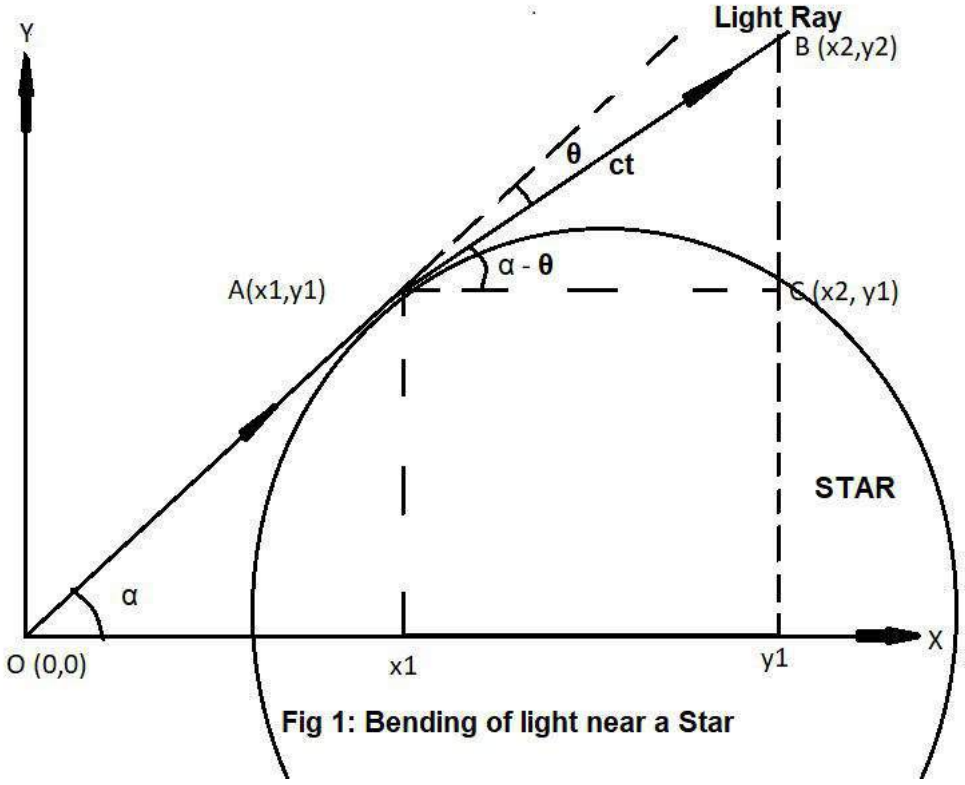

Fig 1: Bending of light near a Star

4.1.10.2. We will consider only those stars that are lying in a single plane, as the bending happens in a single plane. This electro magnetic radiation or the light travels further and 77further into the space. If this radiation encounters another star in the same plane, this radiation will bend again in its gravitation field or otherwise it will continue its voyage into space.

4.1.10.3. On every bending its energy will boost-up and frequency will increase.

4.1.10.4. We will calculate the energy and frequency of the electro-magnetic radiation depending on the type of star that populate in that region of the milky way.

4.1.10.5. There is more possibility that the radiation reaching the center of Milkyway (or any Galaxy).

IV. USING ARTIFICIAL INTELLIGENCE FOR SELECTION OF STARS

We can use Artificial Intelligence (AI) processes and equations fothis selection process for further accuracies. But we did not use AI at this stage.

Here the ray of light (Electro-magnetic radiation) forms a cone of light, which may cover a number of stars in its path. We will use AI equations to single out only one star. Or otherwise all the bending happens in one plane and a single ray of light (not cone). Simulate a Star's Mass, Diameter, Type according to the type of stars in that region of Milkyway Galaxy.

V. EQUATION OF BENDING INCOMING RAY OF LIGHT (Θ)

The equation " $4 (G M/c^2)/R_o$ " is the deflection angle for light found by using null geodesics in the Schwarzschild metric according to General Relativity.http://www.Theory.caltech.edu/people / patricia/obsertop.html

$$\theta = 4GM / c^2R$$

Where E is energy of photon and c is velocity of light photon.
The distance of the photon from center = r. Energy due to Gravitation of Sun (or star) on the photon = $E_s = E\, g_o\, r / c^2$. Frequency of photon = $\vartheta = E / h$ or $E = h\, \vartheta$.

VI. COMPUTER SIMULATIONS / CALCULATIONS

We performed Simulations and calculations after implementing formulae as shown below.

Excel Table equations checking and Crosschecking the different calculations

Different formulae used in the Excel calculation sheet
Let w = $(2\, c^2 / h)$

x = $(\mu \cos\phi + c + g_o t)^2$

y = $(\mu+c)(\mu+c)$

z = $(1 / (\mu \cos\phi + c + g_o t)^2) - (1 / (\mu+c)(\mu+c))$

p = $(2\, c^2 / h)\, [(1 / (\mu \cos\phi + c + g_o t)^2) - (1 / (\mu+c)(\mu+c))]$

therefore...

$P = w / x - w / y = w\,(1/x - 1/y)$

Change in Energy = $\frac{1}{2}\, (E / c^2)\, (g_o^2 t^2 + 2\mu \cos\phi\, g_o t + 2c g_o t)$, here $E = h\, \vartheta$ that means
Change in Energy = $\frac{1}{2}\, (h\, \vartheta / c^2)\, (g_o^2 t^2 + 2\mu \cos\phi\, g_o t + 2c g_o t)$

// ////////////////////////// Following equations are added to cross check accuracy of implementation in excel , there can be mistakes while we apply equations and perform calculations
// //

$P = w / x - w / y = w\,(1/x - 1/y)$

We checked this above equality for making sure calculations are going in right direction.

Hight of Photon from the surface of Sun = (R-r) Where r is radius of Sun and R is the distance of photon from the centre of Sun

Initial Energy due to sun at R = m g_o (R-r) = $m\,(\mu \cos\phi + c)^2 / 2 = E\,(\mu \cos\phi + c)^2 / 2c^2 = E\,(\mu^2 \cos^2\phi + c^2 + 2\mu c) / 2c^2$

Final Energy due to sun = m g_o (R-r- c t - $g_o t^2$) = $\frac{1}{2}\,(E / c^2)(-\mu \cos\phi - c - g_o t)^2 = \frac{1}{2}\,(E / c^2)(\mu^2 \cos^2\phi + c^2 + g_o^2 t^2 + 2\mu \cos\phi\, g_o t + 2c g_o t + 2\mu \cos\phi\, c)$

Change in Energy due to Sun = m g_o (R-r- c t - $g_o t^2$) - m g_o (R-r)

= m g_o (R-r- c t - $g_o t^2$- R+ r) = m g_o (- c t - $g_o t^2$) = LHS

Change in Energy RHS = $\frac{1}{2}\,(E / c^2)\,(g_o^2 t^2 + 2\mu \cos\phi\, g_o t + 2c g_o t)$, here $E = h\, \vartheta$ that means

Change in Energy RHS = $\frac{1}{2}\,(h\, \vartheta / c^2)\,(g_o^2 t^2 + 2\mu \cos\phi\, g_o t + 2c g_o t)$

LHS = RHS gives..... Check this identity.....

m g_o (- c t - $g_o t^2$) = $\frac{1}{2}\,(h\, \vartheta / c^2)\,(g_o^2 t^2 + 2\mu \cos\phi\, g_o t + 2c g_o t)$

//////////////////////////////////////

For cross checking only
// //

Hence change in Frequency = $\delta\vartheta = 1 / \{2\,(h / c^2)\,(g_o^2 t^2 + 2\mu \cos\phi\, g_o t + 2c g_o t)\}$

= $\{ 2c^2 / (h\,(g_o^2 t^2 + 2\mu \cos\phi\, g_o t + 2c g_o t)\}$

Here it can be observed that above equation is the main equation and the "change in Frequency equations" in the above case1 and case 2 of this section are special cases of above equation. It will become equation in case1 when ϕ is '0 degrees' and equation in case 2 when ϕ is 180 degrees.

While making the excel sheet we find two types initial frequencies and two types of initial energies. These are confusing, so one will be renamed as START frequency, and another as

START energy. The other two calculated initial frequency and calculated initial energy will exist as it is.

Attached File name

vak CRP1 Origins.xls

1. We need to formulate an excel interation sheet such that we input frequency and it will calculate all the other values like initial energy, final energy, final frequency etc., depending on Sun's gravity, radius and type. By changing input frequency and taking another star also exactly similar to Sun.

In later simulations we will change star data also and get more relevant and meaningful simulations.

File name

C:\E\Vak Cosmic Rays\Vak CR papers\P1 Origins\P1.1. Feq Upshift\vak1 CRP1 Origins.xls

C:\E\Vak Cosmic Rays\Vak CR papers\P1 Origins\P1.1. Feq Upshift\vak CRP1 Origins.xls

2. Here we started with start frequency and that frequency become the final frequency after freefall. Later the light ray of same frequency was went to another star and became initial frequency.

Initial Frequency = $\vartheta i = \zeta = E\ (\mu^2\ Cos^2\ \phi + c^2 + 2\mu\ Cos\ \phi c)/2hc^2$

$= E\ (\mu\ Cos\ \phi + c)^2\ /2\ hc^2 = \zeta$

$\Rightarrow\ 2\zeta hc^2/E = (\mu\ Cos\ \phi + c)^2$

$\Rightarrow\ 2\zeta hc^2/E = (\mu\ Cos\ \phi + c)^2$

$\Rightarrow\ (2\zeta h/E)^{1/2} = (\mu\ Cos\ \phi + c)$

$\Rightarrow\ ((2\zeta h/E)^{1/2} - c) = \mu\ Cos\ \phi$

Final Frequency = $\vartheta o = E\ (\mu^2\ Cos^2\ \phi + c^2 + g_o^2 t^2 + 2\mu\ Cos\ \phi\ g_o t + 2cg_o t + 2\mu\ Cos\ \phi c)/2hc^2$

$= \frac{1}{2}\ (E / hc^2)(-\mu\ Cos\ \phi - c - g_o t)^2$

$\vartheta o = \frac{1}{2}\ (E / hc^2)(-\mu\ Cos\ \phi - c - g_o t)^2$

$\Rightarrow\ \vartheta o = \frac{1}{2}\ (E / hc^2)(-\mu\ Cos\ \phi - c - g_o t)^2$

$\Rightarrow\ (c\ (2\ \vartheta o\ h/E)^{1/2} - c - g_o t) = \mu\ Cos\ \phi = (c\ (2\zeta h/E)^{1/2} - c)$

$\Rightarrow\ (c\ (2\ \vartheta o\ h/E)^{1/2} - c - g_o t) = (c\ (2\zeta h/E)^{1/2} - c)$

$\Rightarrow\ (c\ (2\ \vartheta o\ h/E)^{1/2} - g_o t) = (c\ (2\zeta h/E)^{1/2})$

$\Rightarrow\ (2\ \vartheta o\ h/E)^{1/2} - g_o t/c = (2\zeta h/E)^{1/2}$

Initial energy = $h\ \vartheta\ (\mu\ Cos\ \phi + c)^2\ /2\ c^2$

Initial frequency = Initial energy / h

$= h\ \vartheta\ (\mu\ Cos\ \phi + c)^2\ /2\ c^2\ /\ h$

$= \vartheta\ (\mu\ Cos\ \phi + c)^2\ /2\ c^2$

Photon Start frequency = $E\ (\mu\ Cos\ \phi + c)^2\ /2\ hc^2$

Initial energy = $h\ \vartheta\ (\mu\ Cos\ \phi + c)^2\ /2\ c^2$

Initial frequency = Initial energy / h

$= h\ \vartheta\ (\mu\ Cos\ \phi + c)^2\ /2\ c^2\ /\ h$

$= \vartheta\ \boldsymbol{(\mu\ Cos\ \phi + c)^2\ /2\ c^2}$

Photon Start frequency = $E\ (\mu\ Cos\ \phi + c)^2\ /2\ hc^2$

Ratio (Final energy / Initial Energy) =

$= [\frac{1}{2}\ (E / c^2)(-\mu\ Cos\ \phi - c - g_o t)^2] / [E\ (\mu\ Cos\ \phi + c)^2\ /2\ c^2\ ]$

$= [\ \frac{1}{2}\ (E / c^2)(\mu^2\ Cos^2\ \phi + c^2 + g_o^2 t^2 + 2\mu\ Cos\ \phi\ g_o t + 2cg_o t + 2\mu\ Cos\ \phi c)\ ] / [\ E\ (\mu^2\ Cos^2\ \phi + c^2 + 2\mu\ Cos\ \phi c)/2c^2\ ]$

$= [\ (-\mu\ Cos\ \phi - c - g_o t)^2] / [\ (\mu\ Cos\ \phi + c)^2\ ]$

$= [\ (\mu^2\ Cos^2\ \phi + c^2 + g_o^2 t^2 + 2\mu\ Cos\ \phi\ g_o t + 2cg_o t + 2\mu\ Cos\ \phi c)\ ] / [\ (\mu^2\ Cos^2\ \phi + c^2 + 2\mu\ Cos\ \phi c)\ ]$

=1.0001850323435700E+00

Ratio (Final frequency / Initial frequency)=

$= \vartheta i\ /\ \vartheta f$

Stars In Galaxy

C:\E\Vak Cosmic Rays\Vak CR papers\Galaxy Stars\Nova Stars in Milkyway.doc

VII. MILKYWAY GENERAL STRUCTURE

Our Milkyway appears to be a galaxy with a 12-18,000 ly long "bar" in the central bulge, which is two to three times longer than it is wide. Its central bulge consists of old stars whose brightest stars are red giants of relatively low mass and big bluish stars recently born from gas held tightly around the galactic center (towards an object called Sagittarius A* , a Densemass massing about 2.5 million suns), Its central bulge extends to two to four bluish spiral arms on opposite sides that wrap around the bulge and each other outwards through the dimmer and redder galactic disk, possibly including broken arm segments, yellowish "ghost" arms where most short-lived OB stars have already perished.

Surrounding the Milky Way's spiral disk and bulge is the slightly flattened galactic halo of old stars, averaging somewhat lower in mass than our sun, including a relatively small number of individual stars and 200 or so globular clusters -- roughly half above and half below the disk.

VIII. SPECTRAL TYPE

Electromagnetic radiation from the star is analyzed by splitting it with a prism or diffraction grating into a spectrum exhibiting the rainbow of colors interspersed with spectral lines. Each line indicates a particular chemical element or molecule, with the line strength indicating the abundance of that element. The strengths of the different spectral lines vary mainly due to the temperature of the photosphere, although in some cases there are true abundance differences.

This is a system of classification which indicates the star's predominant colour showing its surface temperature. (See Table1. Spectral types) The sequence of the seven basic spectral types is denoted in capital letters, as derived from surface temperature, particularly at the extremes of the spectrum, in the bluish and reddish tints of the hottest and coolest stars, respectively.

Table 1: Spectral types: Shows a system of classification which indicates the star's predominant colour showing its surface temperature, with examples

Class	Effective temperature[1][2]	Vega-relative chromaticity[3][4][5]	Chromaticity (D65)[6][7][8][9]	Main-sequence mass[10][11] (solar masses)	Main-sequence radius[10][11] (solar radii)	Main-sequence luminosity[10][11] (bolometric)	Hydrogen lines	Fraction of all main-sequence stars[8]	Example
O	≥ 30,000 K	blue	blue	≥ 16 $M_\odot$	≥ 6.6 $R_\odot$	≥ 30,000 $L_\odot$	Weak	~0.00003%	Iota & Zeta (Alnitak) Orionis Aa
B	10,000–30,000 K	blue white	deep blue white	2.1–16 $M_\odot$	1.8–6.6 $R_\odot$	25–30,000 $L_\odot$	Medium	0.13%	Algol A, Regulus Aa
A	7,500–10,000 K	white	blue white	1.4–2.1 $M_\odot$	1.4–1.8 $R_\odot$	5–25 $L_\odot$	Strong	0.6%	Sirius A, Vega
F	6,000–7,500 K	yellow white	white	1.04–1.4 $M_\odot$	1.15–1.4 $R_\odot$	1.5–5 $L_\odot$	Medium	3%	Procyon A, Eta Cassiopeia A (F9-G0)
G	5,200–6,000 K	yellow	yellowish white	0.8–1.04 $M_\odot$	0.96–1.15 $R_\odot$	0.6–1.5 $L_\odot$	Weak	7.6%	Sun, Alpha Centauri A

K	3,700–5,200 K	light orange	pale yellow orange	0.45–0.8 $M_\odot$	0.7–0.96 $R_\odot$	0.08–0.6 $L_\odot$	Very weak	12.1%	Alpha Centauri B, Epsilon Eridani
M	2,400–3,700 K	orange red	light orange red	0.08–0.45 $M_\odot$	≤ 0.7 $R_\odot$	≤ 0.08 $L_\odot$	Very weak	76.45%	Proxima Centauri, Barnard's Star

Each spectral type is further subdivided into 10 divisions from 0 through 9, hottest to coolest. Most stars are of type M, with diminishing numbers up to type O -- quite rare in our galaxy. About 90 percent of all stars are main sequence dwarfs of spectral type F through M (excluding 9 percent white dwarfs, 0.5 percent red giants, and 0.5 percent everything else). On the other hand, the average mass of main sequence dwarf stars rises dramatically from M to O.

The current version of CHVIEW consolidates stars of unknown spectral type as well as those of all other spectral types into "X". The non-OBAFGKM spectral types include reddish giants and supergiants that have become relatively rich in carbon, such as C (formerly R and N) and S types, as they have run out of hydrogen as the primary fuel for nuclear fusion -- none are currently believed to be located within 250 ly from Earth. WC (carbon-rich) and WN (nitrogen-rich) Wolf-Rayet stars such as Suhail (WC8, Gamma2 Velorum Aa) are massive stars (averaging 20 solar masses in binaries with O stars) that may have already expelled 40 percent or more of their original mass, including their entire hydrogen envelope. The extreme luminosity of Wolf-Rayets is obscured by the dust and gas shed by them.

Analysis of the spectral lines found in star light yields additional information, which is noted in lower case letters following the capital letter denoting spectral type. Examples include:

Table 2: Types of Spectral lines: Analysis of the spectral lines found in star light yields additional information

Spectral peculiarities for stars	
Element symbol: Code	Abnormally strong spectral lines of the specified element(s)[30]
:	uncertain spectral value[17]
...	Undescribed spectral peculiarities exist
!	Special peculiarity
comp	Composite spectrum[30]
e	Emission lines present[30]
[e]	"Forbidden" emission lines present
er	"Reversed" center of emission lines weaker than edges
eq	Emission lines with P Cygni profile
f	N III and He II emission[17]
f*	N IV λ4058Å is stronger than the N III λ4634Å, λ4640Å, & λ4642Å lines[31]
f+	Si IV λ4089Å & λ4116Å are emitted, in addition to the N III line[31]
(f)	N III emission, absence or weak absorption of He II
(f+)	[32]
((f))	Displays strong He II absorption accompanied by weak N III emissions[33]
((f*))	[32]
h	WR stars with hydrogen emission lines.[34]

ha	WR stars with hydrogen seen in both absorption and emission.[34]
He wk	Weak Helium lines
k	Spectra with interstellar absorption features
m	Enhanced metal features[30]
n	Broad ("nebulous") absorption due to spinning[30]
nn	Very broad absorption features[17]
neb	A nebula's spectrum mixed in[30]
p	Unspecified peculiarity, peculiar star.[d][30]
pq	Peculiar spectrum, similar to the spectra of novae
q	P Cygni profiles
s	Narrow ("sharp") absorption lines[30]
ss	Very narrow lines
sh	Shell star features[30]
var	Variable spectral feature[30] (sometimes abbreviated to "v")
wl	Weak lines[30] (also "w" & "wk")

Some stars have stellar companions so close that they appear to be single stars. Analysis of the spectra from such stars may indicate Doppler shifts from the movements of the stellar pair, suggesting the presence of a companion star. Called spectroscopic doubles (spec.dou.) or binaries (SB), spectral lines found in their star light may be periodically doubled ("double-line" binary). If one star's spectrum is too faint to be seen, however, the spectral lines of the primary star may oscillate about a mean position ("single-line" binary). In astrometic binaries, the presence of an invisible companion is inferred from slight "wobblings" in the motion of the primary.

MASS & EVOLUTION. A star is probably born as a nebular cloud of gas and dust of interstellar size collapses, spinning inward via an accretion disk towards an increasingly dense core. While still obscured from view by dust, nuclear fusion may ignite at the center of these pre-stellar objects, as hydrogen is fused into helium. Proto-stars (pre-"main sequence," T-Tauri stars and Herbig-Haro objects, possibly R Coronae Australis/CD-37 13027 which may only be 27 ly from Sol) are born as the energy of hydrogen fusion pushes outward to balance the inward pull of gravity. Eventually, any surrounding -- possibly stellar amounts of -- gas and dust that remain around the star will be blown away by the star's radiation in T-Tauri winds, including much that may be infalling through its stellar disk and blown out in jets (that may be driven by an intense magnetic field) at the star's poles. Once fusion begins, planets may have only a few hundred thousand years or so to form from proto-planetary objects before the dusty circumstellar disk becomes too tenuous, and the star enters the main sequence. Young stars in the solar neighborhood include many OBA type stars such as Beta Pictoris (A3-5), which is young enough to have an easily detectable dust disk, Epsilon Eridani (a K2V with a dust ring as wide as 60 times the Earth to sun distance that is estimated to be between one half and one billion years old), the double-binary system of HD 98800 which has four main-sequence K and M stars that may be only 10 million years old.

Astrophysicists have concluded that, in order to sustain the nuclear reactions necessary to become a star, a gaseous body must have about 0.074-0.080 the mass of our sun. Currently, some astronomers have been defining smaller objects with between 0.013 and 0.080 solar masses (about 13 to 80 Jupiter masses) as "brown" dwarfs, especially those in particularly eccentric orbits around a star since such objects probably formed at about the same time as the star from the same nebular cloud. (According to at least one theory, a "super planet" that is detected in a close-in orbit could be either a brown dwarf or a

gas giant that formed after the birth of the star from a dust disk but migrated inward as the result of friction with dust or some other mechanism.) While at least one theory predicts a huge number of brown dwarfs, their dimness make them difficult to detect and few discoveries were actually confirmed until recently. In 1995, however, a brown dwarf companion to Gliese 229 (only about 19 ly distant) was not only confirmed by the international astronomical community but also photographed by the Hubble Space Telescope; by late 1996, at least 12 were found within 250 ly of Earth -- even more if farther objects are counted.

Most stars begin their life as "dwarfs" and spend the bulk of their lifetime in the main sequence with the same spectral type. As a star ages within the main sequence, however, it can become more as well as less luminous. Once a star moves off the main sequence, it will eventually swell so large that it's surface temperature will drop enough to shift its spectra dramatically downwards. Some large stars will shift spectral class down and back up more than once, as they shed mass through stellar winds and outbursts like nebulae and novae and shift from core hydrogen fusion (e.g., to helium, carbon, then oxygen) as their primary source of radiant energy.

Roughly 90 percent of all dwarf stars have a mass between 0.085 (M8) and 0.8 (G8) in theory -- such as Tau Ceti (G8p) -- of that of our sun, Sol. About 10 percent of the stars, including Sol (G2), lie within the intermediate main sequence. While the lower limit of this range is 0.9 solar masses, the upper mass limit is uncertain, somewhere between six (B5) and 10 (B2) solar masses in theory.

Most of the stars discussed thus far will swell up and become giant stars for a period of about 20 percent of their main-sequence lifetime, as they use up their core hydrogen and begin fusing helium then heavier elements at higher temperatures. Our own sun will leave the main sequence by expanding from its current diameter of about 0.01 of an astronomical unit (AU) -- 1/100 of the distance from the Earth and to the sun -- to as much as one AU. Eventually, these giant stars will literally puff off their cooler outer layer of mostly unfused hydrogen into interstellar space as planetary nebulae, leaving behind the dense cores called "white" dwarfs that are as small as, or smaller, than the Earth in diameter but with 0.5 to 1.4 solar masses.

Less than one percent of all stars lie in the upper main sequence, between about eight (B3) and 120 (O3) solar masses in theory. These stars quickly consume their core hydrogen, swell up into larger "supergiants," but may blow up in supernovae. The end result of such explosions may be a neutron star (1.4 to six solar masses) or a more massive a black hole.

Small, cool, and faint M stars -- such as nearby Barnard's Star (M3.8) which may already be around 10 billion years old -- may last for 50 billion years or more before cooling into black dwarfs. However, the more massive a star is, the faster it consumes and sheds its mass, and the shorter it "lives" as a star. [The lifespan of a star is a function of their mass (or energy supply) and luminosity (rate of energy consumption) -- roughly proportional to 1/Mass raised to the power of 2.5.] The hottest and most massive stars may use up their hydrogen at such a pace that they last less than a million years, short compared with our sun's expected lifetime of about 10 billion years -- still about five billion to go. Vega, type A0, may live only one billion years; a type B star may live for 30-some million years; and the massive O types may last only as long as three to four million years. Hence, the OBA stars observed in our skies are relatively young stars compared with redder spectral types, and any planets found around these stars are unlikely to have had the time to have evolved multi-cellular lifeforms similar to those found on our 4.5 billion-year-old Earth. Since the estimated age of our galaxy is about 13 billion years or less, none of the lower mass stars (M to G8) have had time to fade from view, but most of the previously born, higher mass stars (B to O) have already perished.

Stars also are assigned luminosity classes:

Table 3: Yerkes luminosity classes: A number of different luminosity classes are distinguished and listed above.

Yerkes luminosity classes		
Luminosity class	Description	Examples
0 *or* Ia+	hypergiants or extremely luminous supergiants	Cygnus OB2#12 – B3-4Ia+ [18] V810 or Omicron1 Centauri (?)
Ia	luminous supergiants	Eta Canis Majoris – B5Ia [19] Antares Aa, Canopus
Iab	intermediate-size luminous supergiants	Gamma Cygni – F8Iab [20]
Ib	less luminous supergiants	Zeta Persei – B1Ib [21]
II	bright giants	Beta Leporis – G0II [22] Dubhe A, Tarazed
III	normal giants	Arcturus – K0III [23] Aldebaran Aa, Arcturus
IV	subgiants	Gamma Cassiopeiae – B0.5IVpe [24] Procyon A, Beta Hydri
V	main-sequence stars (dwarfs)	Achernar – B6Vep [21] Sol, Sirius A
sd (*prefix*) *or* VI	subdwarfs	HD 149382 – sdB5 *or* B5VI [25] Kapteyn's Star
D (*prefix*) *or* VII	white dwarfs [c]	van Maanen 2 – DZ8 [26] Procyon B, Sirius B

This classification system is perhaps a better indicator of a star's relative age and stage of evolution within its class as well as of its mass. Subdwarfs, such as nearby Kapteyn's Star (M0VI or M0sd), are more bluish than younger main-sequence dwarf stars and have a lower "metals" content of elements heavier than helium -- perhaps due to their birth in an earlier age (or region) of the galaxy when relatively few supernovae had as yet spewed their metals into surrounding dust clouds. Most of the stars in the central bulge and in the globular clusters of the galactic halo are old, low metals stars.

LOCAL STARS & STELLAR POPULATIONS. Stars in the solar neighborhood include representatives of the two major stellar populations of the galaxy, disk and halo stars.

Including the stars of the distant globular clusters, halo stars are among the galaxy's oldest, thought to be mostly 10 billion years and older. While halo stars are only very weakly concentrated towards the galactic plane, they exhibit a strong concentration towards and including the galactic nucleus but with highly eccentric orbits. These stars contain a very low metals abundance relative to the sun (with a mean around 0.02 of Sol's). Not surprisingly, there are very few halo stars are in the solar neighborhood (perhaps as low as 0.1 percent), but they include local subdwarfs, Kapteyn's Star (M0VI or M0sd) and Groombridge 1830 (a G8VIp with "superflares" that is now believe to be a single star -- no M-type flare star companion). Also called Population II stars because of their later discovery, this group also includes RR Lyrae variables with periods greater than 12 hours, subdwarfs and other extremely metal-poor stars, and some red giants.

Often called Population I stars, the relatively younger stars of the galactic disk can be further subdivided into four distinctive groups: very young spiral arm; young thin disk;

intermediate-age disk; and older thick disk and nucleus. As mentioned previously, the spiral arms include most of the galaxy's interstellar gas and dust, young stars, and stellar associations, including: O and B stars; supergiants; Cepheid variables; pre-main sequence, T-Tauri stars and Herbig-Haro objects (e.g., R Coronae Australis/ CD-37 13027); and some A stars. Less than a hundred million years old, these stars are rich in metals (as rich as, but ranging up to twice, Sol's abundance) and have highly circular galactic orbits within 1,000 ly of the galactic plane. While often extremely bright when not obscured by dust, these stars probably total substantially less than one percent of all Milky Way or nearby stars.

Young thin disk stars lie within 1,500 ly of the galactic plane and have galactic orbits of low eccentricity. Around one billion years or more in age, they include many A and F stars, AFGK giants, some GKM main-sequence dwarfs, and white dwarfs. While they have a mean metals abundance near Sol's (1.0), some may be twice as rich. Totalling as much as nine percent of all stars in the solar neighborhood, they include Sirius2 (A0-1Vm and A2-5VII -- also DA2-5) and Vega (A0Va).

Intermediate-age disk stars include our Sun (G2V), most G and some K and M dwarfs, some subgiants and red giants, and planetary nebulae. Many are around five billion years old and have a metals content ranging from 0.5 to 1.0 of Sol's (with a mean around 0.8). These stars lie within 3,000 ly of the galactic plane, with moderately eccentric galactic orbits. For example, Sol is traveling at seven kilometers per second north ward out of the plane and may eventually rise 200-250 ly above it after 15 million years, while the Alpha Centauri3 (G2V, K1V, and M5.5Ve flare star) system may eventually travel about 800 ly out with an upward velocity that is three times faster. As much as 84 percent of the stars in the solar neighborhood are included in this group.

Most thick disk and many nucleus stars are old. While many are more than eight billion years old, they are probably less than 10 billion years old. They include many K and M dwarfs, white dwarfs, some subgiants and red giants, moderately metals-poor stars, long-period variables, and RR Lyrae variables with periods less than 12 hours. Most thick disk stars lie within 5,000 ly of the galactic plane (thick disk mean of 3,500 ly) and have considerably eccentric orbits. Their metals abundance ranges from 0.2 to 0.5 of Sol's (with a thick disk mean of 0.3). Thick disk stars may comprise as much as four percent of nearby stars, including Lalande 2115 (M2.1V) which is moving perpendicular to the galactic plane at a fast velocity of 47 km/sec.

NOTABLE NEARBY STARS. More information on specific nearby stars (with links to research papers abstracted and electronically scanned by NASA and other organizations or by individual astronomers) is available at SolStation.com's web pages on Notable Nearby Stars.

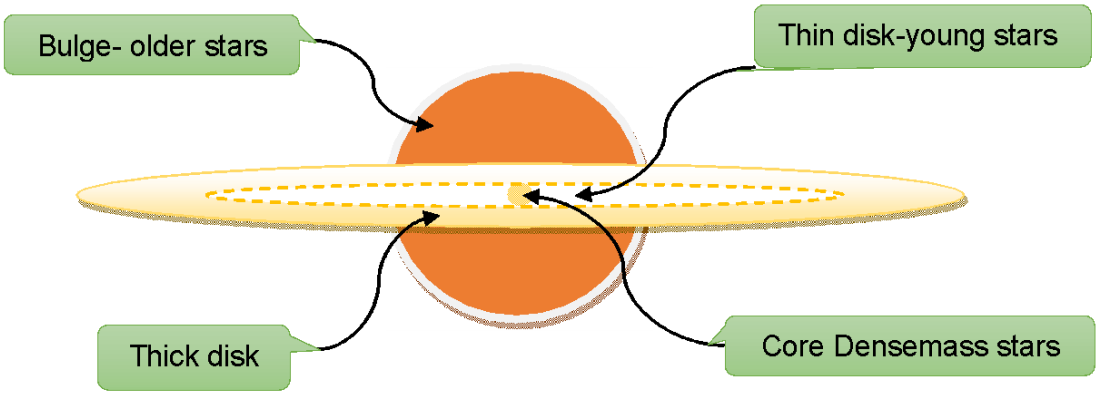

Fig 2. Milkyway or any Spiral Galaxy

Robert Gendler, Amanda Smith, IoA, Cambridge U.

Larger and jumbo image.

Spiral galaxies like the Milky Way and its largest neighbor, Andromeda, have large central bulges of mostly older stars, as well as a relatively young thin spiral disk (surrounded by older, thick disk stars that may have come from mergers with satellite galaxies) and a luminous halo that includes numerous globular clusters (more).

Now we will form a Table of types of Stars in the Milkyway (See above fig):

Table 4: Types of Stars in various parts of Milkyway

Part of Milky-way	Types of stars in it	age
Local stars & stellar populations	disk stars	
-do-	disk and halo stars See Note1	10 billion years and older
-do-	distant globular cluster stars	10 billion years and older
Solar neighbour hood	subdwarfs, Kapteyn's Star (MoVI or Mosd) and Groombridge 1830 Note 2	
-do- Population II stars	RR Lyrae variables, subdwarfs and other extremely metal-poor stars, and some red giants. See Note3	
Galactic Disk	Population I 1. very young spiral arm; 2. young thin disk; 3. intermediate-age disk; 4. older thick disk and nucleus. See note 4	
Galactic disk and Spiral arms	young stars, and stellar associations, including: O and B stars; supergiants; Cepheid variables;	

	pre-main sequence, T-Tauri stars and Herbig-Haro objects (e.g., R Coronae Australis/CD-37 13027); and some A stars See note 4	
Young thin disk stars lie within 1,500 ly of the galactic plane	A and F stars, AFGK giants, some GKM main-sequence dwarfs, and white dwarfs See Note 5	one billion years or more
Intermediate-age disk stars lie within 3000 ly	our Sun (G2V), most G and some K and M dwarfs, some subgiants and red giants, and planetary nebulae see Note 6	
thick disk and many nucleus stars lie within 5,000 ly (thick disk mean of 3,500 ly)	K and M dwarfs, white dwarfs, some subgiants and red giants, moderately metals-poor stars, long-period variables, and RR Lyrae variables with periods less than 12 hours See Note 7	More than8 Billion years old

Note1: Halo stars show increasing concentration towards galactic center. They have low metal abundance compared to Sun.

Note 2: subdwarfs, Kapteyn's Star (M0VI or M0sd) and Groombridge 1830 (a G8VIp)

Note 3: These are Population II stars includes RR Lyrae variables, subdwarfs and other extremely metal-poor stars, and some red giants.

Note 4: Population I stars: includes galaxy's interstellar gas and dust, young stars, and stellar associations, including: O and B stars; supergiants; Cepheid variables; pre-main sequence, T-Tauri stars and Herbig-Haro objects (e.g., R Coronae Australis/CD-37 13027); and some A stars.

Note 5 : they include many A and F stars, AFGK giants, some GKM main-sequence Totalling as much as nine percent of all stars in the solar neighbourhood, they include Sirius2 (A0-1Vm and A2-5VII -- also DA2-5) and Vega (A0Va).

Note 6: Intermediate-age disk stars include our Sun (G2V), most G and some K and M dwarfs, some subgiants and red giants, and planetary nebulae. the Alpha Centauri3 (G2V, K1V, and M5.5Ve flare star) As much as 84 percent of the stars in the solar neighborhood are included in this group.

Note 7: Thick disk and many nucleus stars: They include many K and M dwarfs, white dwarfs, some subgiants and red giants, moderately metals-poor stars, long-period variables, and RR Lyrae variables with periods less than 12 hours. Thick disk stars may comprise as much as four percent of nearby stars.

IX. DISCUSSIONS AND CONCLUSION

Here in this paper we saw that

1. That High energy Cosmic rays can be originated from star light from our Milkyway or Any other Galaxy with a low energy. The light rays will gain frequencies and energies will become particles and gain energies to become High energy.
2. We did a simulation of Subbarao's path (Multiple Bending) with all the stars in a plane. A ray started will go on bend and its frequency gets upshifted and gains energy at every star in its path. Real star positions will be taken in a subsequent paper.
3. We have shown a table of star distributions in our Milkyway. This table will be used in the next paper where we will take the stars types possible at various locations in our Milkyway, and near real star simulation will be done.
4. Dynamic Universe Model proposed like the three additional sources 1. frequency up-

shifting of electro-magnetic radiation rays, 2.astronomical jets from Galaxy centres and 3. occasional solar flares from sun or other stars in Milkyway. We simulated and proved that first one "frequency upshifting of electro-magnetic radiation rays" is a feasible solution to this problem of "Origins of Cosmic rays".

ACKNOWLEDGEMENTS

I sincerely thank Maa Vak for continuously guiding this research.

REFERENCE

1. ^ Woodside, Gayle (1997). Environmental, Safety, and Health Engineering. US: John Wiley & Sons. p. 476. ISBN 978-0471109327. Archived from the original on 2015-10-19.
2. ^ Stallcup, James G. (2006). OSHA: Stallcup's High-voltage Telecommunications Regulations Simplified. US: Jones & Bartlett Learning. p. 133. ISBN 978-0763743475. Archived from the original on 2015-10-17.
3. Fermi Space Telescope (2013) FGST details at: https://fgst.slac.stanford.edu/
4. ^ HESS collaboration (2016). "Acceleration of petaelectronvolt protons in the Galactic Centre". Nature. **531** (7595): 476–479. arXiv:1603.07730.Bibcode:2016Natur.531..476H. doi:10.1038/nature17147. PMID 26982725.
5. ^ Collaboration, IceCube (12 July 2018). "Neutrino emission from the direction of the blazar TXS 0506+056 prior to the IceCube-170922A alert". Science. **361** (6398): 147–151. arXiv:1807.08794. Bibcode:2018Sci...361..147I.doi:10.1126/science.aat2890. ISSN 0036-8075. PMID 30002248.
6. ^ Jump up to: [a] [b] "What are cosmic rays?". [https://web.archive.org/web/20121028154200/http://imagine.gsfc.nasa.gov/docs/science/know_l1/cosmic_rays.html] NASA, Goddard Space Flight Center. Archived from the original on 28 October 2012. Retrieved 31 October 2012. copy Archived 4 March 2016 at the Wayback Machine.
7. H. Dembinski; et al. (2018). "Data-driven model of the cosmic-ray flux and mass composition from 10 GeV to 10^11 GeV". Proceedings of Science. ICRC2017: 533. arXiv:1711.11432. doi:10.22323/1.301.0533.
8. ^ "Cosmic Rays". National Aeronautics and Space Administration. Nasa. Retrieved 23 March 201.
9. ^ Gaensler, Brian (November 2011). "Extreme speed". COSMOS (41). Archived from the original on 7 April 2013.
10. ^ Watson, L. J.; Mortlock, D. J.; Jaffe, A. H. (2011). "A Bayesian analysis of the 27 highest energy cosmic rays detected by the Pierre Auger Observatory". Monthly Notices of the Royal Astronomical Society. **418** (1): 206–213. arXiv:1010.0911. Bibcode:2011MNRAS.418..206W. doi:10.1111/j.1365-2966.2011.19476.x. https://www.auger.org/index.php/component/users/?view=login.
11. S.N.P.GUPTA (2012) SITA: Dynamic Universe Model: Blue Shifted Galaxies Prediction. Lap Publications, Saarbrucken, Germany.
12. S. N. P. GUPTA (2017) Nucleosynthesis after frequency shifting in electromagnetic radiation near gravitating masses in Dynamic Universe Model with Math.
13. Einstein A (1952) The foundation of General theory of relativity. Dover publications, New York, USA.
14. Gupta, S.N.P. (2010) Dynamic Universe Model: A Singularity-Free N-Body Problem Solution. S. N. P. Gupta 130 VDM Publications, Saarbrucken. http://vaksdynamicuniversemodel.blogspot.in/p/books-published.html
15. Gupta, S.N.P. (2011) Dynamic Universe Model: SITA Singularity Free Software. VDM Publications, Saarbrucken. http://vaksdynamicuniversemodel.blogspot.in/p/books-published.html
16. Gupta, S.N.P. (2011) Dynamic Universe Model: SITA Software Simplified. VDM Publications, Saarbrucken. http://vaksdynamicuniversemodel.blogspot.in/p/books-published.html

17. Gupta, S.N.P., Murty, J.V.S. and Krishna, S.S.V. (2014) Mathematics of Dynamic Universe Model Explain Pioneer Anomaly. Nonlinear Studies USA, 21, 26-42.
18. Gupta, S.N.P. (2013) Introduction to Dynamic Universe Model. International Journal of Scientific Research and Reviews Journal , 2, 203-226.
19. Gupta, S.N.P. (2015) "No Dark Matter" Prediction from Dynamic Universe Model CameTrue! Journal of Astrophysics and Aerospace Technology, 3, 1000117.
20. Gupta, S.N.P. (2014) Dynamic Universe Model's Prediction "No Dark Matter" in the Universe Came True! Applied Physics Research, 6, 8-25.
21. Gupta, S.N.P. (2015) Dynamic Universe Model Predicts the Live Trajectory of New Horizons Satellite Going to Pluto. Applied Physics Research, 7, 63-77.
22. Gupta, S.N.P. (2014) Dynamic Universe Model Explains the Variations of Gravitational Deflection Observations of Very-Long-Baseline Interferometry. Applied Physics Research, 6, 1-16.
23. S.N.P Gupta (2019) Rotating Universe and Simultaneous Existence of Red and Blue shifted Galaxies in Dynamic Universe Model. OSP J Nuc Sci 1: JNS-1-105 https://drive.google.com/file/d/1HJ63FVkLmrJly9dosfGhl5sD73hRiTN/view?usp=sharing
24. S.N.P Gupta (2019) Model of Universe. OSP J Nuc Sci 1: JNS-1-109 https://drive.google.com/file/d/1JpdEy_-__dS81CiYaaCgzz6m8cslIM7z/view?usp=sharing

This page is intentionally left blank

Combustion Characteristics of High-Density Briquettes Produced from Sawdust Admixture and its Performance in Briquette Stove

Bello R. S & Onilude M. A.

University of Ibadan, Nigeria

ABSTRACT

Combustion characteristics of high-density briquettes produced from sawdust admixture at three moisture contents of 12%, 10%, and 8% using screw press extruder was investigated in this work. The briquettes were burnt in free air and developed briquette stove and the combustion characteristics data collected and analyzed. The burn characteristics investigated include ignition time, total burning time, mass reduction, normalized burn rate, the effects of density on briquette characteristics, and stove performance. The results indicated that briquettes' self-ignition time in open air and stove was slow, however, burns with a steady flame. High density of the briquette was responsible for slow flame propagation resulting in a longer time to burn out while lower density briquettes reach the burning phase faster than higher-density briquettes. The normalized burn rate increases with an increase in briquette density. The stove performance characteristics most depend on the quality of fuel material. There is an inverse relationship between specific fuel combustion and thermal efficiency of the stove. The specific fuel consumption increases with decrease in moisture content. From these results, the higher the briquettes particle moisture, the higher the specific fuel combustion and the lower the stove thermal efficiency and vice versa.

Keywords: briquette, high-density, extruder, burn rate, normalized, thermal, efficiency.

Classification: FOR Code: 299902

Language: English

London Journals Press

LJP Copyright ID: 925625
Print ISSN: 2631-8490
Online ISSN: 2631-8504

London Journal of Research in Science: Natural and Formal

Volume 20 | Issue 3 | Compilation 1.0

Combustion Characteristics of High-Density Briquettes Produced from Sawdust Admixture and its Performance in Briquette Stove

Bello R. S. [α] & Onilude M. A. [σ]

ABSTRACT

Combustion characteristics of high-density briquettes produced from a screw press extruder using sawdust admixture at three particle moistures of 12%, 10%, and 8% was investigated in this article. The briquettes produced were burnt in free air and briquette stove while the combustion data collected was analyzed. The combustion characteristics investigated include ignition time, total burning time, mass reduction, and burn rates. The effects of particle moistures and briquette density on stove performance were also evaluated. The results show that self-ignition time and flame propagation for each briquette in open air and the stove was slow. Briquetes from lower particle moisture reach the burning phase faster than higher particle moisture briquettes. The normalized burn rate for all briquettes increased with an increase in density. The specific fuel consumption increases with decrease in particle moisture. At higher particle moisture, the specific fuel combustion reduces and vice versa for all briquettes. This result is indicative of an inverse relationship between specific fuel combustion and stove thermal efficiency.

Keywords: Briquette, high-density, extruder, burn rate, normalized, thermal efficiency.

Author α: Department of Agricultural & Bioenvironmental Engineering Technology, Federal College of Agriculture Ishiagu, Nigeria

σ: Department of Wood Products Engineering, University of Ibadan, Nigeria

I. INTRODUCTION

Among the several energy resources available, fossil fuel remained the most exploited resource in today's technological world. Economic growth, urbanization, population increase, and global energy needs have led to overdependence and increased demands on the use of fossil fuels, which consequently had contributed to the outrageous increases in fuel prices in developing countries of Africa and Asia, especially in Nigeria. This increasing trend of fossil fuel prices coupled with worsening effects of global warming have prompted the exploration of alternative sources of energy such as wood and briquettes (Lim, 2007). However, these resource-based materials are under pressure from both human activities and natural factors, including draught.

According to a 2010 report of the Energy Commission of Nigeria, Nigeria, as of 2010, was consuming about 43.4 x 10^9 kg of fuel-wood annually (Ajiboye *et al.,* 2016) with an average daily consumption of about 0.5 to 1.0 kg of dry fuel-wood per person (Olorunnisola, 2007). This invariably made the demand for fuel wood to have risen to about 213.4x10^3 metric tons, while the supply would have decreased to about 28.4x10^3 metric tons by the year 2030 (Adegbulugbe, 1994). The complete reliance on the use of wood, which, is on the increase on daily basis especially in the less technologically developed countries of the world as stated by Aremu and Agarry (2013), for industrial and domestic cooking would not solve the present energy crisis; rather it would lead to deforestation or desertification resulting in further scarcity of this resource (Salunkhe, *et*

al, 2012). As noted by Olorunnisola, (2007), this should, of necessity be characterized by a departure from the present subsistence energy usage levels, to more sustainable and diversified energy options such as densification into briquettes.

Different raw material properties produce different conditions during the densification process, and this causes differences in the final quality of the products (Qian *et al.,* 2013, Križan *et al.,* 2015). It is necessary, therefore, to characterize these material properties to know out their optimal factor for densification. It is equally important to determine the impact of the technological and material variables: raw material parameters; technological process; and structural variables (Križan *et al.,* 2015), known to grossly affect the final quality of the briquettes.

Variability in biomass materials and structural requirements have made applicable technological processes and machines used in high-density briquette production defer. The utilization of high-pressure technologies in the densification of loose materials and their use in boiler furnace chambers for remote industrial and domestic heating are strong reasons to study their combustion characteristics and increased applications (Risović *et al.*, 2008).

Chin and Siddiqui, 2000 and Faizal *et al,* (2011) gave a good review of research works on the combustion characteristics of biomass. Husain *et al,* (2002) documented the combustion characteristics of low-density briquettes containing fiber and shell residues in 60:40 ratio using 10% starch (of the weight of residues) as binding agent. Li (2003) investigated the ignition temperature of coal briquette with plastic (polyethylene) addition and found that the ignition temperature decreased from 413 to 373°C when plastic was added. Currently, there are relatively few published works on the combustion characteristics of high-density briquettes produced from sawdust admixtures and its effect on different property behaviours compared to its low and medium-density briquettes. In producing high quality briquettes, several combustion characteristics such as burning rate, fuel consumption rate, smoke generation, flame propagation, ignition time, gross calorific values, and heat release values among others are required.

However, the majority of these studies were extensively carried out and reported for low and medium-density (using manual or piston press technologies). However, the present level of literature and data are not sufficient to fully exploit the full potential of high-density briquettes from sawdust admixture. Consequently, more studies are required for its characterization. This work investigates the novel combustion characteristics of briquettes produced from composite sawdust under steady-state experimental conditions.

II. MATERIALS AND METHOD

Briquette samples: In this study, samples of high-density briquettes (Figure 1) produced from sawdust admixture at 12%, 10%, and 8% particle moistures using a screw press extruder.

Briquette stove: As noted by Bello *et al.*, (2013), the effects of smoke around the cooking environment make existing stoves environmentally unfriendly and uncomfortable during cooking. Therefore, a focused effort on stove design and technology, and other factors needed to deliver the health and climate benefits associated with reducing the emissions and improving the health of citizens and their economic and social impacts (Bello *et al.*, 2013) necessitated the development and testing of an updraft high-density briquette/ biomass stoves (Bello *et al.*, 2019).

Figure 1: Briquette samples and stove used for the test

III. METHODOLOGY

A measured quantity of briquettes was burnt and two recommended performance tests: (water boiling test (WBT) and controlled cooking test (CCT)) to evaluate quantitative and qualitative information about the fuel combustion characteristics and stove performances(Stewart, 1987) .

Water boiling test (WBT): Dry weights of experimental materials like pot and stove were taken and recorded. The pot was filled with an initial known weight of water and the same weight was maintained throughout the course of the experiment. The water temperature data was recorded at intervals of five (5) minutes until the moment the water came to a vigorous boil.

Controlled cooking test (CCT): Controlled cooking test was carried out with rice and yam and the performance characteristics of the briquettes in the stove. When the cooking was properly done, the mass of the cooked yam and time to achieve cooking were recorded with the aid of a stopwatch.

Statistical analysis tools and models: Statistical analysis was carried out to verify the significance of the variations in the selected briquettes. The model parameters were estimated using SPSS 16.0 program (Release 16.0.0 for Windows) and Excel (Microsoft Corp., 2003) software to establish relationships between briquette burn characteristics. The effects of briquette density and moisture content on the burn characteristics of the briquette was done to determine the level of significance of each parameter on measured variables.

Correlation analysis was used to examine the relationship among the variables to provide a standard index of variability between the correlation coefficients. Regression analysis was also carried out to establish the relative contributions of briquette density, and material moisture in the prediction of the combustion characteristics of each briquette. The results of the unstandardized (β) and standardized Beta (B) regression coefficients, multiple correlation coefficient (R), adjusted R^2, and its associated p values for each of the variables that suggest whether the generated regression model is a good predictor of briquettes' properties or not (Mitchual *et al.,* 2013) were determined.

Performance test variables and equations: The variables used in the calculation of stove and briquette parameters were based on the approach used by FAO (1990), Ahuja *et al.* (1997) and Olorunisola (1999). Four sets of variables used in the evaluation of test procedures are as follows:

i. *Briquette burn rate:* The procedure for the determination of briquette burn rate employed by Onuegbu *et al.* (2012) and Bello *et al.* (2015) was adopted in the experiment. Briquette sample of known weight was ignited with a burner and the weight loss measured every 10 seconds throughout the combustion process using a stopwatch until constant burnt weight was obtained. The weight loss at specific time was computed from the expression:

$$\text{Burn rate} = \textit{Total weight of burnt briquette (kg)/Total time taken (hr)} \quad (1)$$

ii *Time spent in cooking per kilogram of cooked food (T_s):* Ratio of time spent in actual cooking to the total weight of the cooked food.

$$T_s = \textit{Total time spent in cooking (hr)/Total weight of cooked food (kg) (hr/kg)} \quad (2)$$

iii *Specific fuel consumption:* Specific fuel consumption is defined as the amount of solid fuel equivalent used in achieving a defined task divided by the weight of the task. It can be expressed as:

$$PHU = Mass\ of\ fuel\ consumed/Total\ mass\ of\ cooked\ food \quad (3)$$

iv *Thermal efficiency (η):* Thermal efficiency is a measure of the proportion of the total energy which is gainfully employed in any thermody-namic system. This is a ratio of the work done by heating and evaporating water to the energy consumed by burning wood. According to Clarke (1985) the thermal efficiency of a cooking stove depends largely on how well the heat generated is transferred from hot gas fuel line to the pot or vessel on the stove (convective heat transfer). Thermal efficiency is calculated from the percentage heat utilized (PHU) given by:

$$\eta th(100\%) = Burn\ rate\ x\ PHU \quad (4)$$

IV. RESULTS

4.1 Briquette burning characteristics

Free air and stove combustion tests were used to determine the briquettes burn characteristics. Each briquette was ignited by lighter and supplemental fuel (kerosene) enough to ensure the whole of the surface of the briquette was ignited simultaneously. Figure 2 shows the different stages of combustion processes from ignition to burnout. Figure 2(a) is the ignition phase, fire establishment can be observed burning around the briquette, Figure 2(b) & (c) are phases in the flaming combustion stage (d), is at the end of flaming combustion (burnout), and finally, in stage (e), there is no flame and the briquette decomposes purely by char combustion.

Figure 2: Flame propagation of briquette in stove combustion chamber

After igniting the lighter was removed, the combustion proceeded with flame heights of up to 46 cm. From this preliminary observation, it was evident that the designed combustion chamber could contain the flame height within the chamber as seen from Figure 2.

4.2 Briquette mass reduction rate

Table 1 shows the rate of each briquette reduction by mass consumed during burning. Mass loss was recorded for each briquette burnt at intervals until the mass of the briquette was 5% of its initial mass (Chaney, 2010).

Table 1: Mass of materials consumed in stove and normalized mass

Time (hr)	Mass of Fuel (kg)			Normalized Mass			Briquette Length (m)		
	12%	10%	8%	12%	10%	8%	12%	10%	8%
0.00	1.05	1.09	1.60	1.00	1.00	1.00	0.90	0.90	0.90
0.17	0.96	1.01	1.49	0.91	0.93	0.93	0.78	0.74	0.70
0.33	0.88	0.90	1.40	0.84	0.83	0.88	0.67	0.62	0.59
0.50	0.76	0.78	1.27	0.72	0.72	0.80	0.52	0.47	0.45
0.67	0.62	0.66	1.16	0.50	0.61	0.73	0.47	0.38	0.32
0.84	0.47	0.57	1.08	0.45	0.52	0.68	0.38	0.27	0.21
1.01	0.34	0.45	1.0	0.32	0.41	0.63	0.28	0.22	0.15

4. 3 Effect of density on NBR

The impact of mass-volume reduction on density is shown in Table 3 to find relationships between reduced mass and density of all test samples.

Table 3: Effect of mass-volume reduction on briquette density

Time (hr)	Mass of fuel (kg)			Reduced volume of briquette			Reduced density of briquette		
	12%	10%	8%	12%	10%	8%	12%	10%	8%
0.00	1.00	1.00	1.00	1.49	1.49	1.49	0.71	0.73	1.07
0.17	0.91	0.93	0.93	1.29	1.22	1.16	0.74	0.83	1.29
0.33	0.84	0.83	0.88	1.11	1.02	0.97	0.79	0.88	1.44
0.50	0.72	0.72	0.80	0.98	0.78	0.74	0.78	1.00	1.72
0.67	0.50	0.61	0.73	0.82	0.63	0.53	0.76	1.05	2.19
0.84	0.45	0.52	0.68	0.63	0.45	0.45	0.75	1.27	2.40
1.01	0.32	0.41	0.63	0.46	0.36	0.25	0.74	1.25	4.00

4.4 Briquette performance characteristics in stove

The briquette was tested in a special briquette stove to determine the variations in time required to raise water temperature to 100 °C in water boiling test (WBT) and time taken to boil specific quantity of food in controlled cooking test (CCT)

Figure 3: Water boiling and cooking test setups

4.5 Briquette burn rate determination in boiling water (WBT)

The summary of results of water boiling test (WBT) and controlled cooking tests (CCT) using each briquette sample in order to determine briquette consumption (burn rate) in briquette stove is presented below in Table 4 and 5. The controlled cooking tests (CCT) were conducted under various conditions for two varieties of food; rice and yam, respectively were presented in Table 5.

Table 4: Water boiling test (WBT) performance results

Parameter	12%	10%	8%
Time before fuel reaches steady burning (min)	3.35	7.23	2.32
Time spent to boil 1.5kg of water to 100 °C (hr)	0.14	0.09	0.07
Total time spent for total fuel combustion (hr)	0.69	0.78	0.90
Mass of consumed fuel (kg)	1.62	1.09	1.05
Burn Rate (kg/hr)	2.35	1.34	1.17

Table 5: Controlled cooking test (CCT) performance results with rice and yam

Parameters	12%	10%	8%
Initial mass of raw food (kg)	1.00(1.00)	1.00(1.00)	1.00(1.00)
Final mass of cooked food (kg)	2.39(2.33)	2.38(2.45)	2.40(2.35)
Initial mass of fuel before cooking (kg)	1.60(1.60)	1.09(1.09)	1.05(1.06)
Final mass of fuel after cooking (kg)	0.60(1.04)	0.40(0.40)	0.71(0.43)
Mass of consumed fuel (kg)	1.00(0.56)	0.69(0.69)	0.34(0.62)
Total time spent for cooking (hrs)	0.66(0.39)	0.62(0.34)	0.54(0.31)
Burn Rate (kg/hr)	1.52(1.44)	1.11(2.03)	0.6(2.00)

4.4 Briquette performance characteristics in stove

The briquette was tested in a special briquette stove to determine the variations in time required to raise water temperature to 100 °C in water boiling test (WBT) and time taken to boil specific quantity of food in controlled cooking test (CCT)

Figure 3: Water boiling and cooking test setups

4.5 Briquette burn rate determination in boiling water (WBT)

The summary of results of water boiling test (WBT) and controlled cooking tests (CCT) using each briquette sample in order to determine briquette consumption (burn rate) in briquette stove is presented below in Table 4 and 5. The controlled cooking tests (CCT) were conducted under various conditions for two varieties of food; rice and yam, respectively were presented in Table 5.

Table 4: Water boiling test (WBT) performance results

Parameter	12%	10%	8%
Time before fuel reaches steady burning (min)	3.35	7.23	2.32
Time spent to boil 1.5kg of water to 100 °C (hr)	0.14	0.09	0.07
Total time spent for total fuel combustion (hr)	0.69	0.78	0.90
Mass of consumed fuel (kg)	1.62	1.09	1.05
Burn Rate (kg/hr)	2.35	1.34	1.17

Table 5: Controlled cooking test (CCT) performance results with rice and yam

Parameters	12%	10%	8%
Initial mass of raw food (kg)	1.00(1.00)	1.00(1.00)	1.00(1.00)
Final mass of cooked food (kg)	2.39(2.33)	2.38(2.45)	2.40(2.35)
Initial mass of fuel before cooking (kg)	1.60(1.60)	1.09(1.09)	1.05(1.06)
Final mass of fuel after cooking (kg)	0.60(1.04)	0.40(0.40)	0.71(0.43)
Mass of consumed fuel (kg)	1.00(0.56)	0.69(0.69)	0.34(0.62)
Total time spent for cooking (hrs)	0.66(0.39)	0.62(0.34)	0.54(0.31)
Burn Rate (kg/hr)	1.52(1.44)	1.11(2.03)	0.6(2.00)

5.6 Stove performance evaluation

The performance of the stove was evaluated by determining its specific fuel consumption (SFC) and thermal efficiency and the result presented in Table 6.

Table 6: Performance evaluation of each briquette parameters

Parameters	12%	10%	10%
Specific fuel consumption (SFC)	0.75	0.68	0.61
Thermal Efficiency (TE) (%)	34.56	52.64	64.38

IIV. DISCUSSIONS

Briquette burning characteristics: Briquette self-ignition time in open air and stove was low, but when supported with little quantity of kerosene, it burns with a steady flame. Each briquette retained its shape during burning and did not expand, hence lasts significantly longer compared to medium or low-density briquettes. The flame characteristics of the burning briquette revealed a progressive smoldering within the briquette hole, followed by a growing yellow flame at the periphery and simultaneous blue flame within the center hole. This flame propagates into high yellow flame with a brilliant white flame at the center and glowing flame at the surrounding. As the briquette burns out, the flame degenerates and gradually dies off as char combustion set-in.

Briquette mass reduction rate: Briquettes with lower burn rates have better performance than those of high burn rates which burn out within a short time.

The gradients of the steady-state combustion phase for each briquette were plotted to find the normalized burn rate (NBR) for each briquette according to equation 5 is shown in Figure 4.

$$NBR = Be^{-\beta x} \quad 5$$

Where
x = the density in kg/m^3
B = exponential frequency factor is a function of briquette burn time in hours.
þ= constant determined for briquette by a least-squares fit of Equation 5.

The exponential equations for each of the lines are: For 12%, 10% and 8% MC briquettes respectively:

$$NBR = 1.1003e^{-1.128s} \quad 6$$
$$NBR=1.0924e^{-0.938s} \quad 7$$
$$NBR = 1.02775e^{-0.526s} \quad 8$$

An exponential function for each curve shows that the least-squares fit line is satisfactory.

To determine the values of B and β for each of the three normalized burn rates of briquette, the mean value for the constant β was determined for each briquette samples as shown in Table 7 which gives a mean of 0.864±0.002 for the sawdust briquettes burnt and the normalized burn rate (NBR) for the briquette expressed as:

$$NBR = 1.0632e^{-0.864s} \quad 9$$

Table 7: Values of B and β for briquette moisture on NBR

MC (%)	B(hr^{-1})	β
12	1.1003	1.128
10	1.0624	0.938
8	1.0275	0.526
Mean	1.0632	0.864

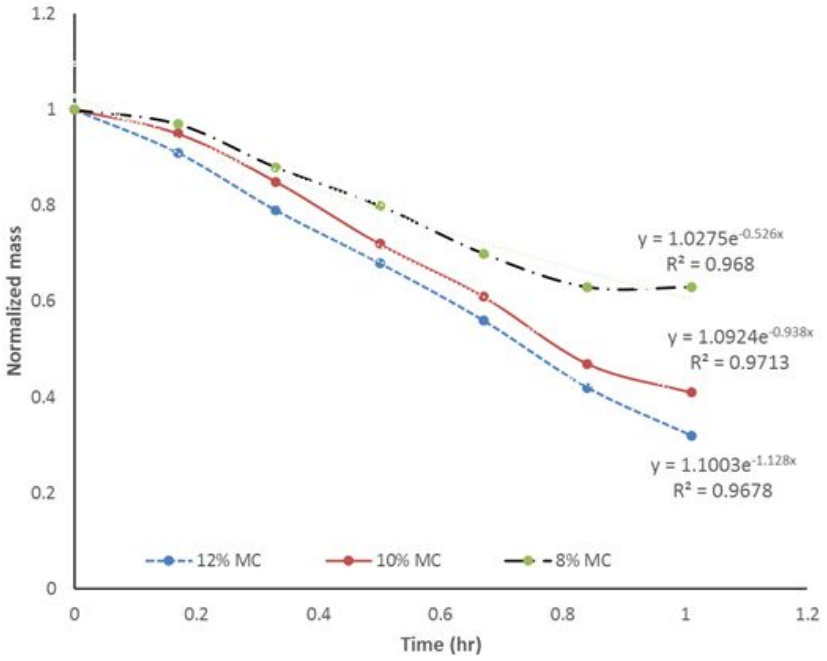

Figure 4: Plot of phase burning of each briquette and burn rate

Effect of density on NBR: The relative importance of density on the normalized burn rate is required to understand the degree to which each factor is needed to be controlled in briquette manufacture. The normalized burn rate was determined and a least-squares fit of the normalized mass was plotted against the density (Figure 5a).

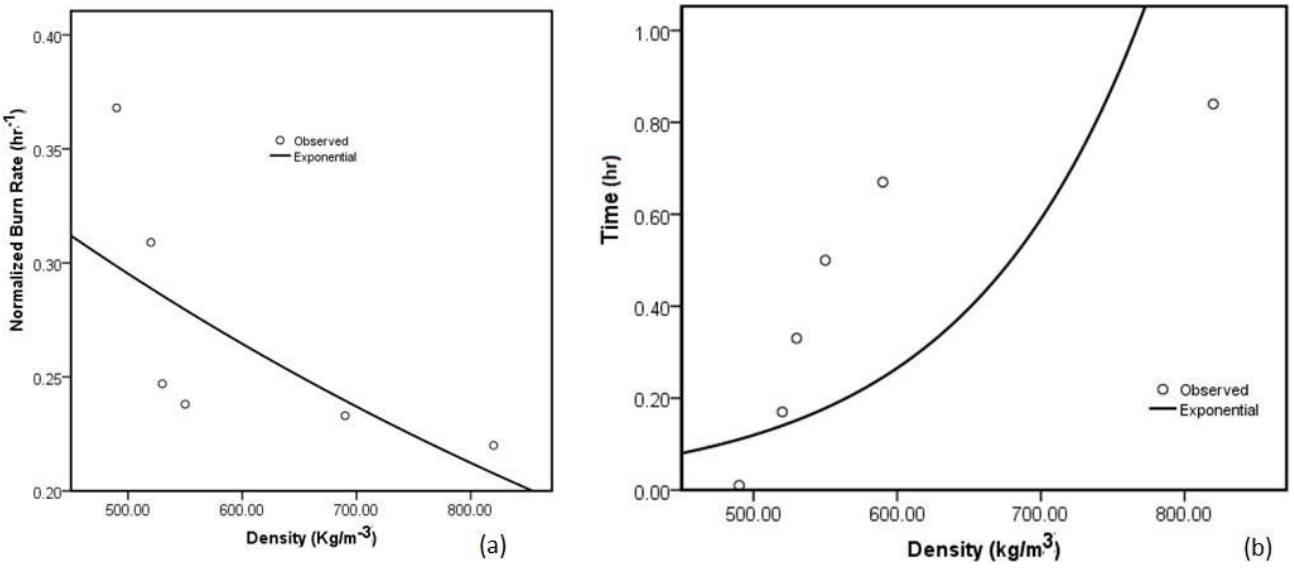

Figure 5: Effects of briquette density on a) NBR and b) total burning time (TBT)

The trend in Figure 5(a) indicates that normalized burn rate increases with an increase in briquette density. After an exponential fit on the scattered plot of NBR versus density, values of constants B and β were estimated for the curve by regression analysis as B=0.501 and β = −0.001 the NBR equation for the exponential curve is:

$$NBR = 0.501e^{-0.001s} \quad 10$$

From the equations, the NBR shows a clear tendency to decrease as the density increases, as predicted from literature (Chaney, 2010). The

result shows the significance of density on normalized burn rate; higher density briquettes have a lower normalized burn rate.

Effect of density on briquette total burning time: Considering the total time taken to burn the whole briquette starting from the initial mass to the maximum mass loss (approximately 5% of initial mass (Mandal *et al.,* 2012) to determine the total burning time (TBT), a plot of time against density (Figure 5b) gives a good estimation of (TBT). An exponential regression analysis provided the best fit curve with the regression equation (11) predicting the total burning time at a given density:

$$TBT = 0.002e^{-0.008s} \quad 11$$

The result indicates that high briquette density was responsible for slow flame propagation resulting in longer burning time. By implication, the higher density briquette takes more time to burn out while a lower density briquettes took shorter time but reach burning phase 2 faster than higher density briquettes.

Effect of briquette density on burn rate: It is equally significantly important to note that the density of briquette increases as the mass to volume ratio reduces. The impact of mass-volume reduction on density is graphically illustrated for briquette samples in Figure 6 and these show some inverse relationships between reduced mass and density of all test samples with significant correlations in lower moisture briquettes: (0.0413, 0.969 and 0.948) for 12%, 10%, and 8% briquettes respectively.

Briquette burn rate in boiling water (WBT) and control cooking tests (CCT): From Table 4, it takes a shorter time (0.07hrs), to boil 1.50kg of water with 8% moisture content briquette, and consuming 1.05kg of fuel, while it takes longer time (0.9<0.78<0.07) hrs to consume the relatively same quantity of fuel for other briquettes.

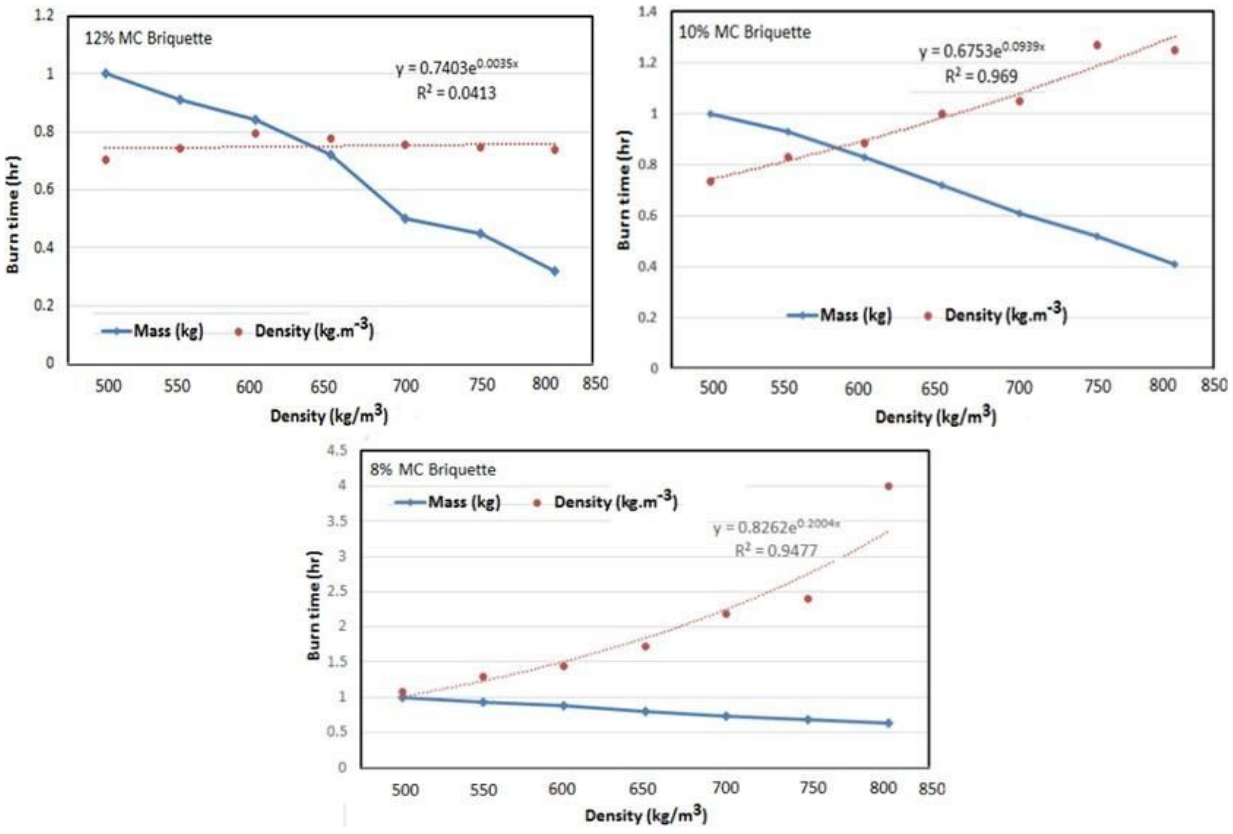

Figure 6: Effect of burn rate on mass reduction and density of 12%, 10% and 8% briquette

The rate of burning of each briquette in the stove significantly varied. The burn rate values decrease with an increase in feedstock moisture content. The implication of this is that more fuel is required for cooking with briquettes produced from higher moisture briquettes than for low moisture briquettes. Variations in the amount of briquette do not significantly affect the resulting burn rates in the cooking of each food. Total time spent in burning off the fuel varied at each stove but maintained a time range of 32-39min. Time spent in cooking rice and yam were as indicated in each operation. Relatively, the time spent in cooking ~1 kg of food; rice (yam) is not significantly different for all the briquettes burnt in the stove (minimum 0.54/0.31 hrs. for 8% moisture briquettes and maximum 0.66 (0.39) hrs. for 12% moisture briquettes). The practical implication is that a lesser quantity of 8% moisture briquettes will be required to cook the same quantity of food compared to the 12% moisture briquettes.

Stove performance evaluation: from the results, the stove has different thermal efficiencies and specific fuel consumption (SFC) when tested with different briquette samples. The result of the thermal efficiency and the average specific fuel consumption of the stove obtained from the experiment are (64.38%, 52.64% and 34.56%), and (0.6, 0.68, 0.75) kg/hr. for 12%, 10% and 8% briquette samples respectively. The thermal efficiency of the stove increases with an increase in briquette material moisture content while the specific fuel consumption increases with a decrease in moisture content. This result implies that stove performance characteristics are largely dependent on fuel material quality. Equally, from the result, it is evident that the fuel burn rate has a significant effect on the stove's thermal performances. The ability to control fuel burn rate is therefore essential if thermal stove performances are to be optimized and that there is an optimum fuel burn rate that could give maximum stove efficiency for a given configuration (Kandpal *et al.,* 1994).

IIIV. CONCLUSION

Form the experimental considerations; the briquette burn characteristics improves with increase in briquette quality. Burn rate increased for briquettes produced at lower moisture content, and reduced for higher density briquettes. Briquette combustion characteristics are dependent on the environmental conditions under which it is burned and also on the medium in which they are burned. Briquette burn rates vary from open-air burning, to controlled air (stove) burning. The briquette stove's thermal efficiency is dependent on the quality of fuel. There is an inverse relationship between specific fuel combustion and thermal efficiency of the stove. The higher the briquettes particle moisture, the higher the specific fuel combustion and the lower the stove thermal efficiency and vice versa.

Conflict of Interests

The authors declared that there is no conflict of interests regarding the publication of the article..

REFERENCES

1. Adegbulugbe AO, 1994. Energy-environment issues in Nigeria. *International Journal of Global Energy Issues 6(12):7-18.*
2. Ahuja DF, Joshi V, Smith KR, Venkataraman, C, 1997. Thermal Performance and Emission Characteristic of Unvented Biomass-Burning Cookstove. *Standard Methods for Evaluation. Biomass. 10:12.*
3. Ajiboye TK, Abdulkareem S, Anibijuwon AOY, 2016. Investigation of Mechanical Properties of Briquette Product of Sawdust-charcoal as aPotential Domestic Energy Source. *J. Appl. Sci. Environ. Manage. Dec. 2016 Vol. 20 (4) 1179-1188. https://dx.doi.org/10.4314/jasem.v20i4.34*
4. Aremu MO, Agarry SE. 2013. Enhanced Biogas Production from Poultry Droppings using Corn Cob and Waste Paper as Co-Substrates, *International Journal of Engineering Science and Technology; 2013 Vol. 5 No. 2 pp 247-253.*

5. Bello RS, Adegbulugbe TA, Onilude MA, 2015. Characterization of three conventional cookstoves in south eastern Nigeria. *Agric Eng Int: CIGR Journal. 17(2):122-129*http://www.cigrjournal.org/index.php/Ejounral/article/view/3037/2106
6. Bello RS, Odey SO, Saidu MJ. 2019. *Development and comparative evaluation of three high-density biomass stoves and clay-lined charcoal stove. Proceedings of the 20th International Conference and 40th AGM of the Nigeria Institution of Agricultural Engineers (NIAE), Landmark University, Omu-Aran, Nigeria. Pp 1349 – 1358.*
7. Bello RS, Okafor EC, Ezebuilo CN, Bello MB, Umahi O, 2013. Cookstove technologies and environmental impacts in the South-eastern Nigeria. In Sustainable Environmental Management: Issues & Projections. *Eds Bello R. S. Balogun R. B. & Okereke S. N. ch 21. 275-299. Createspace, Charl US. ISBN-13: 978-149-285-349-7*https://www.createspace.com/4462554
8. Chaney J, 2010. Combustion Characteristics of Biomass Briquettes. *Unpublished PhD thesis submitted to the University of Nottingham.*
9. Chin OC, Siddiqui KM, 2000. Characteristics of Some Biomass Briquettes Prepared Under Modest Die Pressures. *Biomass and Bioenergy. 18, 223-228.*
10. Clarke R., 1985. Wood-stove Dissemination. Proceedings of the Conference held at Wolfheze, The Netherlands. *Intermediate Technology Publications, 9 King Street, London. pp 97-102.*
11. Faizal H. M., Latiff Z. A., Mazlan A. Wahid, Darus A. N., 2011. Physical and Combustion Characteristics of Biomass Residues from Palm Oil Mills. *New Aspects of Fluid Mechanics, Heat Transfer and Environment. ISSN: 1792-4596 ISBN: 978-960-474-215-8, 34-38*
12. FAO 1990. The briquetting of agricultural wastes for fuel: Environment and Energy paper*, vol. 11. FAO, Rome.*
13. Husain Z, ZA, Zainal, MZ Abdullah, 2002. Briquetting of palm fiber and shell from the processing of palm nuts to palm oil. *Biomass and Bioenergy 22(6):505-509 DOI: 10.1016/S0961-9534(02)00022-3*
14. Kandpal JB., Maheshwari RC, Kandpal TC, 1994. Air pollution from biomass combustion in domestic cookstove. *Renewable Energy, Vol. 4. No. S. pp. 54S--S49. 1994*
15. Križan P., Miloš M, Ľubomír Š and Beniak J., 2015. Behaviour of Beech Sawdust during Densification into a Solid Biofuel. *Energies 8, 6382-6398; doi: 10.3390/en8076382 ISSN 1996-1073 www.mdpi.com/journal/energiesInternational Energy Agency (IEA), 2002. Africa key Energy Statistics* http://www.iea.org *Accessed October, 2010.*
16. Li, T., 2003. Development of Plastic Waste Disposal Method by Combustion of Coal Briquette. *Department of Ecology Engineering, Toyohashi University of Technology.*
17. Lim MT, 2007. Characterization of a Bubbling Fluidized Bed Biomass Gasifier. *MSc thesis Universiti Sains Malaysia. Pp 1-44.*
18. Mitchual JS, Kwasi F, Darkwa NA, 2013. Effect of species, particle size and compacting pressure on relaxed density and compressive strength of fuel briquettes. *Int J Energy Environ Eng (2013) 4: 30. doi:10.1186/2251-6832-4-30*
19. Olorunnisola AO, 1999. The efficiency of two Nigerian cooking stoves in handling corncob briquettes. *Nigerian Journal of Renewable Energy 7(1&2): 31-34.*
20. Olorunnisola AO, 2007. Production of fuel briquettes from waste paper and coconut husk admixtures. *Agricultural Engineering International, Vol.IX, article EE06066, 2007.*
21. Onuegbu TU, Ekpunobi E, Ogbu IM, Ekeoma MO and Obumselu FO. 2012. Comparative studies of ignition time and water boiling test of coal and biomass briquettes blend. *International Journal of Research & Reviews in Applied Sciences, Vol.7, pp.153–159, 2012.*

22. Qian K., Kumar, Patil A, BellmerK, , Wang D, YuanD, HuhnkeW, RL, 2013. Effects of biomass feedstocks and gasification conditions on the physiochemical properties of char. *Energies, 6, 3972–3986.*
23. Risović A, Dukić, I, Vućković, K., 2008. Energy analysis of pellets made from wood residue. *Croat. J. for. eng. 29 (2008) 1, pp 95-105.*
24. Salunkhe DB Rai RK, Borkar RB., 2012. Biogas Technology, *International Journal of Engineering Science and Technology; (4) No.12 pp 4934-4940.*
25. Stewart, W., 1987. Improved Wood, Waste and Charcoal Burning Stoves. *A Practical Manual. Intermediate Technology Publications, Covent Garden, London, UK.*

This page is intentionally left blank

Combining Ability Study in Some Genetic Stocks of Bottle Gourd

AKM Quamruzzaman, M.M.R. Salim, L. Akhter, M.M. Rahman & M.A.Z. Chowdhury

ABSTRACT

A study was conducted in bottle gourd to estimate the combining ability for yield and its ten yield-related components. Twenty-one bottle gourd hybrids generated from 7 × 7 diallel cross (excluding reciprocals) along with their seven parents evaluated in a Randomized Block Design with three replication at the Olericulture Division of Horticulture Research Centre, Bangladesh Agricultural Research Institute, Gazipur, Bangladesh during 2018-19. Analysis of variance revealed highly significant differences among all the F1 hybrid means and their respective seven parental values for all the traits examined. The mean squares of general combining ability (GCA), the specific combining ability (SCA) were also highly significant. SCA genetic variances were greater than GCA. In the present study, high GCA values were found in parents P2, P4, P5 (days to 1st harvest); P1, P2, P7 (fruit length); P3, P6 (fruit diameter); P3, P6 (exocarp thickness); P6, P1 (TSS); P1, P3 (branches per plant); P3, P6 (vine length); P1, P6 (fruits number per plant); P2, P6, P7 (average fruit weight); P1, P2, P6, P7 (yield per plant), which were selected for good combiner for yield and yield contributing characters.

Keywords: bottle gourd, combining ability, sca, gca, hybrids, additive, and non-additive gene action.

Classification: FOR CODE: 060499

Language: English

London Journals Press

LJP Copyright ID: 925626
Print ISSN: 2631-8490
Online ISSN: 2631-8504

London Journal of Research in Science: Natural and Formal

Volume 20 | Issue 3 | Compilation 1.0

Combining Ability Study in Some Genetic Stocks of Bottle Gourd

AKM Quamruzzaman[α], M.M.R. Salim[σ], L. Akhter[σ], M.M. Rahman[ρ] & M.A.Z. Chowdhury[Ѡ]

ABSTRACT

A study was conducted in bottle gourd to estimate the combining ability for yield and its ten yield-related components. Twenty-one bottle gourd hybrids generated from 7 × 7 diallel cross (excluding reciprocals) along with their seven parents evaluated in a Randomized Block Design with three replication at the Olericulture Division of Horticulture Research Centre, Bangladesh Agricultural Research Institute, Gazipur, Bangladesh during 2018-19. Analysis of variance revealed highly significant differences among all the F1 hybrid means and their respective seven parental values for all the traits examined. The mean squares of general combining ability (GCA), the specific combining ability (SCA) were also highly significant. SCA genetic variances were greater than GCA. In the present study, high GCA values were found in parents P2, P4, P5 (days to 1st harvest); P1, P2, P7 (fruit length); P3, P6 (fruit diameter); P3, P6 (exocarp thickness); P6, P1 (TSS); P1, P3 (branches per plant); P3, P6 (vine length); P1, P6 (fruits number per plant); P2, P6, P7 (average fruit weight); P1, P2, P6, P7 (yield per plant), which were selected for good combiner for yield and yield contributing characters. Higher SCA values were obtained from cross combinations P2xP7, P4xP7 (days to 1st harvest); P4xP5, P3xP5 (fruit length); P3xP6, P2xP4 (fruit diameter); P1xP6, P1xP7 (fruits number per plant); P6xP7, P4xP7 (average fruit weight) and P3xP4, P3xP5, P4xP5, P4xP7 (yield per plant) which may be selected for better commercial hybrids. The predominance of non-additive gene action was recorded in almost all the traits under study. Therefore, the yield and quality traits of bottle gourd can be improved by heterosis breeding by selecting which parents have good specific combining ability for the target trait(s).

Keywords: bottle gourd, combining ability, sca, gca, hybrids, additive, and non-additive gene action.

Author α σ: Olericulture Division, Horticulture Research Centre, Bangladesh Agricultural Research Institute, Gazipur, Bangladesh.

ρ Ѡ: Bangladesh Agricultural Research Council, Farmgate, Dhaka-1207.

I. INTRODUCTION

Bottle gourd [*Lagenaria siceraria* (Mol.) Standl.] is an important winter vegetable crop but it is cultivating year round now a days. But there exists a considerable variability of this crop in Bangladesh, possibilities to develop high yielding varieties through breeding approaches like selection or hybridization. A sound-breeding programme provides the opportunity to produce high yielding varieties of a crop with superior quality. However, the development of a meaningful breeding programme needs information on the nature of gene actions controlling the economic characters and other characters of importance. Knowledge of genetic architecture of the characters under the genetic improvement is essential for adopting appropriate breeding procedure. Such knowledge leads the plant breeder to develop new commercial varieties of the crop. Gardner (1963) stressed that information on variation attributable to genetic differences and also on the relationship among various quantitative traits is fundamentally significant in a crop improvement programme.

London Journal of Research in Science: Natural and Formal

Combining ability studies are more reliable as they provide useful information for the selection of parents in terms of performance of the hybrids and elucidate the nature and magnitude of various types of gene actions involved in the expression of quantitative traits. Diallel cross analysis provides the estimates of genetic parameters regarding combining ability as well as a rapid overall picture of the dominance relationship of the parents studied using the first filial generations (F1) with or without reciprocals. Diallel analysis involving parents give the additional information as presence or absence of epistasis, average degree of dominance, distribution of dominant and recessive genes in the parents. Application of diallel technique in a self-pollinated crop like bottle gourd for this purpose may be appropriate. Genetic information regarding combining ability studies of bottle gourd in Bangladesh is limited. Therefore, the present study was undertaken with the following objectives: to generate information for identification of good general and specific combiners for the improvement of yield and its attributes.

II. MATERIALS AND METHODS

2.1 Experimental site

The experiment was conducted at the Olericulture Division of Horticulture Research Centre, Bangladesh Agricultural Research Institute (BARI) during 2018-19. The experimental field was at 23.9920° N Latitude and 90.4125° E Longitudes having an elevation of 8.2 m from sea level, having agro-ecological zone (AEZ) 28 (Anon., 1995). The experimental site is situated in the sub-tropical climatic zone and characterized by scanty rainfall during the experimental time. The average minimum and maximum temperature were18.37°C and 29.37°C and the average relative humidity varied from 55.55 to 75.70 %. The soil of the experimental field was sandy clay loam in texture having a pH range around 6.0.

2.2 Plant materials

Twenty one cross combinations viz., P1xP2, P1xP3, P1xP4, P1xP5, P1xP6, P1xP7, P2xP3, P2xP4, P2xP5, P2xP6, P2xP7, P3xP4, P3xP5, P3xP6, P3xP7, P4xP5, P4xP6, P4xP7, P5xP6, P5xP7 and P6xP7 along with seven parents viz., P1[code LS14], P2[code LS01], P3 [code LS02], P4[code LS03], P5 [code LS04], [P6 code LS07], P7 [code LS09] of bottle gourd were used in this study. The seeds of these germplasm were sown on the seedbed on 05October, 2018. Twenty days old seedlings were transplanted in the main field on 25October, 2018.

2.3 Experimental design and layout

The experiment was laid out in a Randomized Complete Block design with three replications. The unit plot size was 10.0 x 2.0m maintaining 2.0 x 2.5m spacing and 0.5m drain.

2.4 Land, pit preparation and fertilization

The land was fertilized with organic manure, N, P, K, S, B and Zn @ 3000, 80, 45, 88, 25, 1.8 and 4.5 kg/ha, respectively. Half of organic manure and all of S, Zn and B each of P and K @ 30 kg/ha were applied during final land preparation. Rest of cowdung and P and K @ 15 kg/ha were applied as basal in the pit. Rest of N and K were applied after 20 days of transplanting in 4 equal installments at 20 days interval starting.

2.5 Intercultural operation and plant protection

The soil around the base of each seedling was pulverized after the establishment of seedlings. Necessary intercultural operations were done to ensure normal growth and development of the plants. GI steel sticks were used to support the growing plants and allowed them to grow along string netting along with irrigation was applied to the plants in pits as and when required. Adult red pumpkin beetle was controlled by hand removal daily, whereas fruit fly was controlled at the fruiting stage using poison bait.

2.6 Data recorded

Data were recorded on the following parameters viz., days to 1st harvest, fruit length, fruit diameter, exocarp thickness, TSS, branches per plant, vine length, fruits number per plant, average fruit weight and yield per plant.

2.7 Statistical analysis

Analysis of variance (ANOVA)

All the quantitative data taken were subjected to ANOVA. The total variances of each character were partitioned into block, genotype and error differences. The differences within the classes of effects were tested by F-test, and combining ability analysis of the traits with significant genotypic differences was done according to the Model 1 and Method 2 of Griffing (1956a, b). The fixed effect model was more appropriate in the present case since the parents selected were cross-pollinated lines and the parents, and F_1s were the populations considered. This analysis partitioned the variation due to genotypic differences into general combining ability (GCA) and specific combining ability (SCA) effects.

The mathematical model used in this analysis was as follows:

Yij = m + gi + gj + Sij +

Where,

Yij = is the mean of i x jth genotype over k and l.

ij = l, ...p

k = l, ...b

l = l, ... c

m = population mean

gi = GCA effects of the ith parent.

gj = GCA effect of the jth parent.

eijkl = environmental effects

The significant differences within each of the component effects were tested by F-test. Diallel tables were prepared by computing the averages over the 3 replications of all the parents and F_1s in the appropriate cells. The row sums, column sums, the sum squares of GCA, SCA were all computed from this table.

Analysis of variance of combining ability and expectation of mean squares using Griffing`s (1956) Model I Method 2.

The general combining ability form of ANOVA was as follows:

Source of variation	df	Sum squares	Mean sum squares	F-test	Expected mean squares
GCA	6	SSg	MSg	MSg/Mse	$\sigma^2 e + \frac{(P+2)}{(P-1)} \sum gi^2$
SCA	21	SSs	MSs	MSs/MSe	$\sigma^2 e + \frac{2}{P(p-1)} \sum_I \sum_j Sij^2$
Error	54	Sse	Mse		$\sum^2 e$

GCA and SCA effects

The GCA and SCA effects were estimated according to Sharma et. al. (2002) by the following formula:

$$\text{GCA effects (gi)} = \frac{1}{n+2} \sum_{n} [(Yi. + Yii) - \frac{2}{n} (Y..)] \quad \text{Restricted to } \sum_{i}^{n} gi = 0$$

$$\text{SCA effects (Sij)} = Yij - \frac{1}{n+2}[Yi. - Yii + Yj. + Yjj)] + \left[\frac{2}{(n+1)(n+2)} Yii\right] (i < j)$$

III. RESULTS AND DISCUSSION

The analysis of variance for combining ability (general and specific combining ability) were found highly significant for maximum characters studied except exocarp thickness, TSS, vine length, average fruit weight (Table 1) indicating that both additive and non-additive gene actions played a significant role for the expression of these characters. Dubey and Maurya (2006), Pal *et al.* (2004), Rehana and Sharma (2007), Singh *et al.* (2006) also reported similar result for bottle gourd while Yadav *et al.* (2008), Mohanty (2000), Srivastava *et al.* (2008) reported for bitter gourd, pumpkin, and okra, respectively. GCA variances were higher in magnitude than the SCA variances for all the characters studied, indicating the predominance of the additive gene effects for the characters. Similar findings were reported by Sirohi and Chowdhury (1980), Janakiram and Sirohi (1988), and Choudhury and Kale (1991). Dubey and Maurya (2006), Pal *et al.* (2004) also reported that non-additive gene effects appeared more important than additive gene effects for days to 1st harvest, fruit length, fruits number per plant, yield per plant, days to edible fruit maturity, vine length, Average fruit weight while Rahman (2006) reported similar findings for exocarp thickness, fruits number per plant, average fruit weight, yield per plant in pumpkin.

Table 1: Analysis of variance for combining ability of bottle gourd in bottle gourd

Source of variation	df	Mean sum of square									
		Days to 1st harvest	Fruit length	Fruit diameter	Exocarp thickness	TSS	Branches per plant	Vine length	Fruits number per plant	Average fruit weight	Yield per plant
GCA	6	6.07**	240.00**	13.13**	0.07	0.16	27.47**	1.90	1.71	0.08	23.75**
SCA	21	4.05**	20.20**	1.22	0.03	0.04	27.18**	1.65	2.66**	0.07	20.62**
Error	54	0.72	1.17	0.12	0.01	0.01	0.04	0.00	0.27	0.01	2.20

* *Significant at 1% level of probability;* * *Significant at 5% level of probability*

3.1 General Combining Ability (GCA) Effects

The GCA component is primarily a function of the additive genetic variance. The GCA and SCA variances with each parent play a significant role in the choice of parents. The analysis of variance for combining ability (Table 1) indicated that mean square due to GCA and SCA were highly significant for all the traits. This indicated variation in parents and crosses and significant combination of additive and non additive effects in the expression of the characters. Sit and Sirohi (2002), Dubey and Maurya (2007), and Pandey et al. (2004) had also observed similar findings. A parent with higher positive significant GCA effects is considered as a good general combiner. The magnitude and direction of the significant effects for the seven parents provide meaningful comparisons and would give indications to the future breeding programme. The results of GCA effects for 10 different characters are presented in the Table 2.

In the present study, parent P4 (-0.90**) appeared as the best general combiner followed by P2 (-0.83**) and P5 (-0.62*) for days to 1st harvest as they showed negative significant GCA values (Table 2). Dubey and Maurya (2006) reported a highly significant negative GCA effect for days to 1st harvest under the summer in bottle gourd. Pal *et al.* (2004) also found such effect (-1.80) in bottle gourd. The parent P2 (4.84**) exhibited the highest GCA effect for fruit length,

followed by P1 (4.66**) and P7 (3.40**). Parent P6 showed the highest GCA for fruit diameter (2.32**), followed by P3 (0.94**). Dubey and Maurya (2006), Sharma *et al.* (2002), and Pal *et al.* (2004) reported a significant positive effect in bottle gourd for fruit length and fruit diameter. Yadav *et al.* (2008) reported a significant positive effect (2.59) in bitter gourd. Incase of exocarp thickness highest GCA value was obtained by also P3 (0.14**). Mohanty (2000) mentioned a significant positive GCA effect obtained by PusaVishwas followed by Cuttack Local in bitter gourd. Thus parent P3 was the best general combiner followed by P6 to use in crosses for the improvement of exocarp thickness as indicated by their significant and higher GCA effects. Parent P6 (0.18**) exhibited the highest GCA effect for TSS followed by P1 (0.12**), while parent P1 (2.39**) also exhibited the highest GCA effect for branches per plant followed by P3 (2.28**). The parent PusaSamridhi was reported to have the significant GCA effects for vine length and the number of primary branches by Shinde et al. (2016) in bottle gourd. Dubey and Maurya (2006), Sharma *et al.* (2002), and Pal *et al.* (2004) reported a significant positive effect in bottle gourd. In the case of vine length, the parent P3 (0.78**) showed the highest significant highest value, followed by P6 (0.32**). The one of the most important parameter is fruits number per plant, in which the highest GCA value was obtained by P6 (0.70**) followed by P1 (0.36**), while the parent P6 exhibited the highest positive significant GCA value (0.10**) for average fruit weight followed by P7 (0.09**), P2 (0.06**). P6 showed the highest significant GCA value 1.75**) followed by P1 (1.07**), P2 and P7 (1.06**) for yield per plant. The parent P4 (-2.74**) was however, however a poor combiner for yield per plant. Dubey and Maurya (2006), Quamruzzaman *et al.* (2009) and Pal *et al.* (2004) reported that significant positive GCA effect obtained in summer while Kumar *et al.* (1998) got best GCA effect in bottle gourd for fruits number per plant, average fruit weight and yield per plant. Almost similar trends of additive and non-additive gene actions have been reported previously by other research groups like Gill *et al.* (1984) and Shamanin *et al* (1985).

Table 2: Estimates of general combining ability (GCA) effect and mean of seven bottle gourd parents

Parents	Days to 1st harvest	Fruit length	Fruit diameter	Exocarp thickness	TSS	Branches per plant	Vine length	Fruits number per plant	Average fruit weight	Yield per plant
P1	-0.16 (62.00)	4.66** (41.00)	-0.23 (12.00)	0.01 (2.00)	0.12** (3.50)	2. 39** (29.30)	0.13** (6.90)	0.36** (12.30)	-0.06** (2.35)	1.07* (28.70)
P2	-0.83** (58.30)	4.84** (43.50)	-1.00** (10.80)	-0.13** (2.00)	-0.17** (2.60)	-0.21** (25.50)	0.05** (8.90)	-0.50** (13.00)	0.06** (2.25)	1.06* (29.00)
P3	0.91** (61.00)	-5.18** (20.25)	0.94** (15.80)	0.14** (2.40)	0.02 (3.00)	2.28** (32.70)	0.78** (7.20)	-0.30 (13.50)	0.02 (2.00)	-1.12 (26.50)
P4	-0.90** (57.70)	-0.35 (31.50)	-0.68** (11.30)	-0.03** (2.00)	-0.17** (2.50)	-1.58** (19.00)	-0.27** (7.10)	0.14 (13.00)	-0.28** (1.90)	-2.74** (24.00)
P5	-0.62* (58.00)	1.28** (31.50)	-0.85** (10.70)	-0.05** (2.00)	0.01 (2.70)	-1.80** (32.70)	-0.56** (7.50)	0.25 (13.50)	-0.06** (2.00)	-1.12* (26.50)
P6	0.70* (60.00)	-8.65** (19.50)	2.32** (17.40)	0.07** (2.20)	0.18** (2.50)	0.20** (27.50)	0.32** (7.50)	0.70** (14.00)	0.10** (2.40)	1.75** (34.00)
P7	0.90** (63.00)	3.40** (39.00)	-0.49** (11.70)	0.01 (2.00)	0.02 (3.00)	-1.28** (29.00)	-0.42** (7.20)	-0.13 (13.00)	0.09** (2.20)	1.06* (29.00)
SE (gi)	0.26	0.33	0.11	0.01	0.02	0.06	0.01	0.16	0.02	0.46
SE (gi-gj)	0.40	0.51	0.17	0.02	0.03	0.09	0.01	0.25	0.03	0.70
C.D Value (0.05)	0.59	0.75	0.25	0.02	0.05	0.14	0.02	0.36	0.05	1.04
C.D Value (0.01)	0.82	1.04	0.35	0.03	0.06	0.19	0.03	0.50	0.06	1.45

Figures in the parenthesis are the mean values

* *Significant at 5% level of probability; ** Significant at 1% level of probability*

3.2 Specific Combining Ability (SCA) Effects

The SCA effects signify the role of non-additive gene action in the expression of the characters. It indicates the highly specific combining ability leading to the highest performance of some specific cross combinations. That is why it is related to a particular cross. High SCA effects may arise not only in crosses involving high combiners but also in those involving low combiners. Thus in practice, some of the low combiners should also be accommodated in the hybridization programme. Estimates on SCA effects of the crosses in F1 generation showed that there were a good number of crosses having significant positive or negative SCA effect for different important characters of bottle gourd. None of the hybrids indicated significant positive SCA effects for all the characters. Ram *et al.* (1999), Sharma *et al.* (2001) reported similar results in the case of cucumber and bitter gourd, respectively. The SCA effects of 21 F1 crosses for ten different characters studied are presented in the Table 3.

3.2.1 Days to 1st harvest

Negative SCA effect is preferable for days to 1st harvest. Of the twenty one F1s, thirteen showed negative SCA values (Table 3), indicating that there was considerable heterosis for this character. Out of these crosses, eight crosses showed significant negative SCA values with the larger negative values in crosses P2 x P7 (-3.64**), P4 x P7 (-2.24**), P3 x P5 (-2.20**), P3 x P6 (-2.20**) and P1 x P7 (-2.14**) and was the best specific combiner for the early harvest. The significant SCA effects for days to first harvesting was also reported by Singh et al. (2012) in bottle gourd. Dubey and Maurya (2006), Pal *et al.* (2004), Jayanth et al. (2019), Sharmila et al. (2016) also reported significant SCA effect was obtained for an early harvest in bottle gourd, while Yadav *et al.* (2008) and Quamruzzaman *et al.* (2007) reported similar findings in bitter gourd and eggplant, respectively which were in agreement with the present findings.

3.2.2 Fruit length

More than 50% of the F1s (16 crosses) showed positive SCA values indicating that these hybrids had increasing in fruit length, while the significant positive SCA values were P4 x P5 (6.56**), P1 x P2 (4.91**), P1 x P3 (3.25**), P1 x P7 (3.03**), P4 x P6 (2.44**), P2 x P5 (2.12**) and P2 x P7 (2.00**). Thus these seven combinations showed as the best specific combiner to increase the fruit length. Similar findings were obtained by Janaranjani (2016), Dubey and Maurya (2006); Pal *et al.* (2004); Rani et al. (2017); Sharmila et al. (2016) in bottle gourd and Yadav *et al.* (2008), Mohanty (2000) in bitter gourd and Quamruzzaman et al. (2007) in eggplant.

3.2.3 Fruit diameter

F1s in general had the positive SCA values for fruit diameter while the range was 0.03 to 2.36. Of the F1s, six showed significant positive SCA values indicating that these F1s produced more wider fruits than the means of their parents. The highest SCA value was obtained by P3 x P6 (2.36**) followed by P2 x P4 (0.97**), P1 x P6 (0.86**), P1 x P7 (0.67**), P4 x P7 (0.56*). These combinations may be considered as the best specific combiner to increase the diameter of fruits. Similar findings were reported by Janaranjani (2016), Pal *et al.* (2004); Rani et al. (2017); Sharmila et al. (2016) in bottle gourd, and Yadav *et al.* (2008) in bitter gourd.

3.2.4 Exocarp thickness

Ten F1s showed positive SCA values for the trait (Table 3). This indicates that these F1s produced thicker rind compared to the mean of their parents. Out of these combinations, nine F1's viz., P1 x P5 (0.37**), P3 x P5 (0.26**), P5 x P6 (0.25**), P3 x P4 (0.23**), P3 x P7 (0.19**), P4 x P7 (0.19**), P1 x P2 (0.13**), P3 x P6 (0.13**) showed significant values, which may be the best specific combiner for the improvement of the trait. Similar result was obtained by Janaranjani (2016), while significant positive SCA effect (7.41) was obtained by F1 (1x8) in pumpkin (Mohanty, 2000).

3.2.5 TSS

The range of positive SCA effect was 0.01 to 0.43 for this trait while the significant positive cross combinations were P5 x P7 (0.43**), P2 x P4 (0.34**), P3 x P6 (0.32**), P4 x P7 (0.14**), P3 x P5 (0.13**), P2 x P7 (0.12**), P4 x P5 (0.09**) (Table 3).

3.2.6 Branches per plant

Among the cross combinations, about 11 combinations were significant positive SCA effect while five combinations also showed higher significant positive effect viz., P4 x P6 (6.02**), P2 x P4 (4.01**), P3 x P4 (3.94**), P3 x P6 (2.83**), P6 x P7 (2.72**) play a maximum role to increase branches per plant. The highest SCA effects for a number of branches was also reported by Dubey and Maurya (2006) in bottle gourd. Dubey and Maurya (2006); Sharmila et al. (2016) and Jayanth et al. (2019) reported significant positive effect with the best effect in bottle gourd, while Yadav *et al.* (2008) and Quamruzzaman *et al.* (2007) reported similar findings in bitter gourd and eggplant, respectively which were in agreement with the present findings.

3.2.7 Vine length

The range of significant positive SCA effect was 0.31 to 2.21, while higher values were obtained by P3 x P5 (2.21**), P3 x P4 (1.46**), P6 x P7 (1.04**) P4 x P6 (0.90**), P1 x P3 (0.89**), P3 x P6 (0.86**) indicate that these combinations were very significant in specific combining ability for the improvement of vine length. The highest SCA effects for vine length was also reported by Dubey and Maurya (2006) in bottle gourd. For vine length, the highest positive heterosis was reported in the cross Pusa Naveen×Punjab Komal by Janaranjani et al. (2016) in bottle gourd. Dubey and Maurya (2006) reported similar report with 8 significant SCA effect in the summer while Pal *et al.* (2004); Sharmila et al. (2016) and Jayanth et al. (2019) also reported the best combiner in bottle gourd. In other cucurbitaceous crops like bitter gourd, a similar effect was obtained by Yadav *et al.* (2008) and Mohanty (2000).

3.2.8 Fruits number per plant

Maximum F1s in general had the positive SCA values for fruits number per plant (Table 3). Of the F1s, 7 showed significant positive SCA values indicating that these F1s produced more fruits number per plant than the means of their parents. Seven combinations showing highly significant positive SCA values were P1 x P6 (3.17**), P4 x P6 (3.13**), P1 x P7 (2.62**), P1 x P5 (1.62**), P3 x P4 (1.13**), P2 x P5 (0.86*), P2 x P7 (0.86*). These combinations may be considered as the best specific combiner to increase the fruits number per plant. Similar findings were obtained by Dubey and Maurya (2006) with 8 significant positive SCA values in summer season in bottle gourd while Janaranjani (2016), Moradipour et al (2017), Pal *et al.* (2004); Sharmila et al. (2016) and Rani et al. (2017) reported the same trend in bottle gourd. Similar findings were reported by Yadav *et al.* (2008), Singh *et al.* (2004) in bitter gourd.

3.2.9 Average fruit weight

Among the cross combinations, about 50% F1s showed positive SCA values, of which nine had significant positive values for average fruit weight, and the range was 0.01 to 0.39** (Table 3). This indicates that these F1s produced larger average fruit weight compared to the mean of their parents. Highest significantly positive SCA values was obtained by P6 x P7 (0.39**) followed by P3 x P5 (0.38**), P4 x P7 (0.33**), P3 x P4 (0.30**), P3 x P6 (0.22**), P4 x P5 (0.20**), P2 x P6 (0.10*), P5 x P6 (0.10*) and P2 x P7 (0.09*). The result also in agreement with the findings of Dubey and Maurya (2006), Pal *et al.* (2004); Sharmila et al. (2016) and Rani et al. (2017) in bottle gourd while Yadav *et al.* (2008) and Quamruzzaman *et al.* (2007) reported similar findings in bitter gourd and eggplant, respectively which were in agreement with the present findings.

3.2.10 Yield per plant

Twelve F1s in general had the positive significant SCA values for this trait (Table 37), while highest SCA value was obtained by P3 x P4 (6.90**) followed by other higher SCA values P3 x P5 (5.12**), P4 x P5 (4.22**), P4 x P7 (3.57**), P1 x P7 (3.52**), P1 x P6 (3.40**), P3 x P6 (3.30**), P2 x P7 (3.25**), P2 x P5 (3.21**), P6 x P7 (3.17**), P4 x P6 (2.11*), P2x P3 (1.99*). These combinations may be considered as the best specific combiner to increase the yield per plant. These results were confirming with the result of Janaranjani (2016), Moradipour et al (2017), Sharmila et al. (2016), while Dubey and Maurya (2006) reported best SCA effect was obtained by 7 crosses in summer and Pal *et al.* (2004) reported best combiner was IC-92362 x Pusa Naveen in bottle gourd while Yadav *et al.* (2008) and Quamruzzaman *et al.* (2007) reported similar findings in bitter gourd and eggplant, respectively which were in agreement with the present findings.

Table 3: Estimates of specific combining ability (SCA) effect of 21 crosses for ten characters in bottle gourd

Crosses	Days to 1st harvest	Fruit length	Fruit diameter	Exocarp thickness	TSS	Branches per plant	Vine length	Fruits No. per plant	Av. fruit weight	Yield per plant
P1 x P2	-0.07	4.91**	0.19	0.13**	-0.05	1.80**	-0.17**	-0.50	0.03	-0.56
P1 x P3	-1.83**	3.25**	-1.76**	-0.11**	-0.12**	1.98**	0.89**	-1.33**	-0.01	-2.60**
P1 x P4	-1.18*	1.1	-0.14	-0.04	-0.02	0.83**	-0.74**	-0.77	-0.03	-1.89
P1 x P5	-0.63	1.14	0.03	0.37**	-0.03	0.06	0.65**	1.62**	-0.26**	-0.68
P1 x P6	-1.63**	-2.27**	0.86**	-0.07**	-0.07	-3.94**	-0.24**	3.17**	-0.21**	3.40**
P1 x P7	-2.14**	3.03**	0.67**	-0.01	-0.08*	2.20**	0.70**	2.62**	-0.17**	3.52**
P2 x P3	1.34*	4.07**	-1.14**	-0.17**	-0.06	-5.43**	-1.70**	0.91**	-0.01	1.99*
P2 x P4	0.16	-5.25**	0.97**	-0.01	0.34**	4.01**	-0.47**	-0.03	0.08	0.99
P2 x P5	-1.13	2.12**	-0.03	0.01	0.06	-0.35**	-0.54**	0.86*	0.07	3.21**
P2 x P6	0.54	-0.96	-1.20**	-0.10**	-0.15**	-2.35**	-0.66**	-1.59**	0.10*	-2.56**
P2 x P7	-3.64**	2.00**	0.28	-0.07**	0.12**	2.13**	0.31**	0.86*	0.09*	3.25**
P3 x P4	1.75**	3.27**	-0.31	0.23**	0.01	3.94**	1.46**	1.13**	0.30**	6.90**
P3 x P5	-2.20**	5.64**	-0.97**	0.26**	0.13**	1.83**	2.21**	0.03	0.38**	5.12**
P3 x P6	-2.20**	-1.94**	2.36**	0.13**	0.32**	2.83**	0.86**	0.08	0.22**	3.30**
P3 x P7	1.95**	-0.98	-1.33**	0.19**	-0.09**	-9.35**	-0.70**	0.03	-0.07	-1.19
P4 x P5	0.45	6.56**	0.48*	-0.09**	0.09**	-5.98**	-1.65**	0.58	0.20**	4.22**
P4 x P6	-0.72	2.24**	-2.19**	-0.20**	-0.02	6.02**	0.90**	3.13**	-0.28**	2.11*
P4 x P7	-2.24**	2.20**	0.56*	0.19**	0.14**	-1.17**	-0.60**	-0.42	0.33**	3.57**
P5 x P6	2.67**	0.61	0.32	0.25**	0.03	-7.76**	-1.24**	0.02	0.10*	1.57
P5 x P7	-0.51	0.57	0.13	-0.13**	0.43**	-8.28**	-2.30**	-0.03	0.01	-0.02
P6 x P7	1.32*	3.25**	-0.84**	0.06*	-0.28**	2.72**	1.04**	-0.98*	0.39**	3.17**
SE (sij)	0.65	0.83	0.27	0.03	0.04	0.15	0.01	0.40	0.05	1.13
SE (sii-sjj)	-0.89	1.14	0.37	0.04	0.06	0.20	0.02	0.54	0.06	1.56
CD Value (0.05)	1.14	1.45	0.47	0.05	0.07	0.26	0.04	0.70	0.09	1.98
CD Value (0.01)	1.43	1.83	0.59	0.07	0.09	0.33	0.04	0.88	0.11	2.49

* *Significant at 5% level of probability;* ** *Significant at 1% level of probability*

It is evident that SCA effects of certain crosses were related with the GCA of their parents as the best cross combination for most of the characters involved at least one parent with high or average GCA effects for particular traits. Similar results have been reported by Dubey and Maurya (2006), Maurya *et al.* (1993) in bottle gourd and Mishra *et al.* (1994) in bitter gourd. Sivakami *et al.* (1987), Mishra *et al.* (1994) reported that both additive and non-additive genetic variances were important in the inheritance of total yield. However, Sirohi and Chowdhury (1980), Janakiram and Sirohi (1988), Choudhury and Kale (1991) observed that GCA were dominant over SCA effect for most of the yield related characters. But Dubey and Maurya (2006), Pal *et al.* (2004) reported additive genetic variance was more important than non-additive genetic variance. These differences may be due to the differences in the genetic material studied. Results of the present study were in agreement with those of Sirohi *et al.* (1988). Heterosis (high

SCA) in diallel crosses involving good x good GCA might be due to additive x additive type of interaction which is partially fixable (Pal *et al.* 2004). High SCA effects in the crosses involving poor x poor combining parents were possibly due to intra- and inter allelic interaction.

IV. CONCLUSION

In the present study, high GCA values were found in parents P2 , P4 , P5 (days to 1st harvest); P1, P2, P7 (fruit length); P3, P6 (fruit diameter); P3, P6 (exocarp thickness); P6 , P1 (TSS); P1 , P3 (branches per plant); P3 , P6 (vine length); P1, P6 (fruits number per plant); P2, P6, P7 (average fruit weight); P1, P2, P6, P7 (yield per plant), which are good general combiner for yield and yield contributing characters. Since the yield being the main considerations in the heterosis breeding. So, it is thus concluded that the crosses P2x P7, P4xP7 (days to 1st harvest), P4xP5, P3xP5 (fruit length), P3xP6, P2xP4 (fruit diameter), P3xP5, P5xP6 (fruit exocarp thickness), P2xP4, P3xP6 (TSS), P4xP6, P2xP4 (branches per plant), P3xP5, P3xP4 (vine length), P1xP6, P1xP7 (fruits number per plant), P6xP7, P4xP7 (average fruit weight), P3xP4, P3xP5, P4xP5, P4xP7 (yield per plant) showing high SCA effects for yield and other character could be exploited for hybrid vigor. However, before selecting these combinations for exploitation on a large scale, it requires their further testing. Recurrent and reciprocal recurrent selection procedures should be exploited for the improvement of those characters, where both additives as well as non-additive variances are present.

REFERENCES

1. Anonymous. (1995). Agro- climatatrological data. Agromet Division, Bangladesh Meteorological Department, Joydebpur, Gazipur. pp. 35-65.
2. Choudhury, S.M. and P.N. Kale. (1991). Combining ability studies in bitter gourd. J. Maharashtra Agril. Univ., 16: 34-36.
3. Dubey SK, Maurya IB. (2006). Combining ability studies in bottle gourd [Lagenaria siceraria (Molina) Standl.]. Indian Journal of Horticulture. 63(2):178-181.
4. Dubey SK, Maurya IB. (2007). Combining ability for characters related to yield and earliness in bottle gourd (Lagararia siceraria (Mol.) Standl.). Indian Journal of. Agricultural Research. 41(1):59-62.
5. Gardner, C.O. (1963). Estimation of genetic parameters in cross fertilizing plants and their implications. In: Plant Breeding by W.D. Hanson and F.F. Robinson (eds.), NAS-NRC Pub. Washington. pp.225-252.
6. Griffing, B. (1956a). A generalized treatment of the use of diallel cross in quantitative inheritance. Heredity, 10: 13-50.
7. Griffing, B. (1956b). Concept of general and specific combining ability in relation to diallel crossing systems. Aust. J. Biol. Sci. 9: 463-493.
8. Janakiram, T. and P.S. Sirohi. (1988). Combining ability of quantitative characters in 10x10 diallel cross of round fruited bottle gourd. Ann. Agril. Res. 9: 204-24.
9. Janaranjani, K.G., V. Kanthaswamy and S. Ramesh Kumar (2016) Heterosis, Combining Ability, and Character Association in Bottle Gourd for Yield Attributes, International Journal of Vegetable Science, 22:5, 490-515. DOI: 10.1080/19315260.2015.1084967.
10. Jayanth S, Dr. Makhan Lal, Dr. DS Duhan and Vidya R. (2019). Estimation of heterosis and combining ability for earliness and vegetative traits in bottle gourd [*Lagenaria siceraria* (Molina.) Standl.]. International Journal of Chemical Studies. 7(1): 20-25.
11. Kumar, S., Singh, S. P. and Singh, N. K., (1998). Vegetable Science, 25: 78-80.
12. Kumar, S., S.P. Singh and N.K. Singh. (1998). Line x tester analysis for combining ability and heterosis in bottle gourd [*Lagenaria siceraria* (Mol.) Standl.]. Veg. Sci. 25(1): 78-80.
13. Maurya, I.B., S.P. Singh and N.K. Singh. (1993). Heterosis and combining ability and heterosis in bottle gourd [*Lagenaria siceraria* (Mol.) Standl.]. Veg. Sci. 20: 75-81.
14. Mishra, H.N., R.S. Mishra, S.N. Mishra and G. Parhi. (1994). Heterosis and combining ability

in bitter gourd (*Momordica charantia* L.). Indian J. Agric. Sci. 64 (5): 310-13.
15. Mohanty, B.K. (2000). Combining ability for yield and its components in pumpkin. Indian J. Genet. 60(3): 373-379.
16. Moradipour, F., J.A. Olfati, Y. Hamidoghli, A. Sabouri and B. Zahedi. (2017). General and Specific Combining Ability and Heterosis for Yield in Cucumber Fresh Market Lines, International Journal of Vegetable Science, 23:4, 285-293, DOI: 10.1080/19315260.2016.1262488.
17. Pal, S.N., D. Ram, A.K. Pal and G. Singh. (2004). Combining ability studies for certain metric traits in bottle gourd [*Lagenaria siceraria* (Mol.) Standl.]. Indian J. Hort. 61(1): 46-50.
18. Pandey, S.K., B.P. Srivastava, S.B.L. Srivastava and J.P. Srivastava. (2004). Heterosis and inbreeding depression for fruit characters in bottle gourd [*Lagenaria siceria* (Mol.) Standl.]. Indian J. Hort. 61(2):146-149.
19. Quamruzzaman, A.K.M., M.A. Rashid, S. Ahmad, M.MashiurRahman and N.A. Sultana. (2007). Combining ability estimates in nine eggplant varieties. Pakistan Journal of science and industrial research. 50(1):55-59.
20. Quamruzzaman, A.K.M., M.A. Rashid M.A.T. Masud and M. Nazim Uddin. (2009). Heterosis in bottle gourd. Bangladesh J. Agril. Res. 34(3) : 465-472.
21. Rahman, I.H.M.S. (2006). Genetic diversity, combining ability and interrelationships among yield components in sweet gourd (*Cucurbita moschata*). PhD thesis. Dept. of Horticulture, BAU. pp. 136-147.
22. Ram, D., G. Kalloo and M. Singh. (1999). Combining ability of quantitative characters in bitter gourd (*Cucurbita moschata*). Indian J. Agric. Sci. 69(2): 122-125 .
23. Rani, K.U., and E. Nagabhushana Reddy. (2017). Combining Ability Analysis for Yield and its Components in Bottle Gourd. Int. J. Pure App. Biosci. 5 (4): 809-817. DOI: *http://dx.doi.org/10.18782/2320-7051.5401*.
24. Rehana, N. and S.P. Sharma. (2007). Combining ability studies in bottle gourd. Crop Res. Hisar. 33(1/3): 148-151.
25. Sharma, N., N.K. Sharma, Y.S. Malik and N. Sharma. (2002). Combining ability in long-fruited bottle gourd. Haryana J. Hort. Sc., 31 (1-2): 79-82.
26. Sharmila Shinde, V. S., Supe, M.N., Bhalekar and Gaikwad, S. S. (2016). Combining ability studies in bottle gourd (*Lagenararia siceraria* mol. standl.). Asian journal of science and technology. 07(5): pp.2842-2845.
27. Shinde S, Supe VS, Gaikwad SS. (2016). Combining ability studies for earliness and yield in bottle gourd (*Lagenaria siceraria* L. (Molina) Standl.) in kharif season. Asian Journal of Science and Technology. 7(5):2846-2849.
28. Singh, P. K., kumar, J. C. and Sharma, J. R., (2000). Vegetable Science, 27(2) :162-164.
29. Sinngh, S.K., B. Singh, G.S. Bisht, D. Ram and R. Mathura. (2006). Studies on combining ability in bottle gourd. Veg. Sci. 33(2):194-195.
30. Singh SK, Upadhyay AK, Pandey J, Pandey A K. (2012). Studies on heterosis and combining ability in bottle gourd [Lagenaria siceraria (Molina) Standl.] for yield traits. Annals of Horticulture, 5(2):246-251.
31. Sirohi, P.S. and B. Choudhary. (1980). Inheritance of quantitative fruit characters in bitter gourd (*Momordica charantia* L.). Veg. Sci. 7: 102-07.
32. Sirohi, P.S. and B. Choudhary. (1986). Genetic analysis in long fruited bottle gourd. Indian J. Agric. Sci. 53(10): 880-888.
33. Sit. A.K and P.S. Sirohi. (2002). Exploitation of heterosis in bottle gourd. Hort. J. 15(2): 55-60.
34. Sivakami, N., P.S. Sirohi and B. Choudhury. 1987. Combining ability analysis in long-fruited bottle gourd. Indian J. Hort. 44: (3:4) 213-219.

35. Srivastava, M.K., S. Kumar and A.K. Pal. (2008). Studies on combining ability in okra through diallel analysis. Indian J. Hort. 65(1): 48-51.
36. Yadav, M., R. Chaudhary and D.B. Singh. (2008). Combining ability in bitter gourd. Indian J. Hort. 65(2): 163-166.

This page is intentionally left blank

Investigation of Lipoprotein based MHD Fluid Flow Through an Arterial Channel with Haematocrit

KW Bunonyo & E. Amos

Federal University Otuoke

ABSTRACT

Mathematical models were formulated to investigate lipoprotein based MHD fluid flow through a stenosed arterial channel with hematocrit. The governing nonlinear partial differential equations have been transformed into linear partial differential equations, which are solved analytically. The numerical simulations was done using Mathematica 12, results are presented graphically in the form of velocity and concentration profiles. The effects of various parameters such as the Solutal Grashof number, Schmidt number and other parameters such as Hematocrit parameter, lipoprotein external source parameter on the velocity and concen- tration have been examined with the help of the graphs. The present results have an important bearing on the therapeutic procedure of hyper- thermia, particularly in understanding/ regulating blood flow and lipid profile in the blood.

Keywords: lipoprotein, artery, blood, hematocrit, MHD, fluid and flow.

Classification: FOR Code: 069999

Language: English

London Journals Press

LJP Copyright ID: 925627
Print ISSN: 2631-8490
Online ISSN: 2631-8504

London Journal of Research in Science: Natural and Formal

Volume 20 | Issue 3 | Compilation 1.0

Investigation of Lipoprotein Based MHD Fluid Flow Through an Arterial Channel with Haematocrit

KW Bunono[α] & E. Amos[σ]

ABSTRACT

Mathematical models were formulated to investigate lipoprotein based MHD fluid flow through a stenosed arterial channel with hematocrit has been studied. The governing non-linear partial differential equations are transformed into linear partial differential equations, solved analytically. The numerical simulations was done using Mathematica 12, results are presented graphically in the form of velocity and concentration profiles. The effects of various parameters such as the Solutal Grashof number, Schmidt number and other parameter such as Hematocrit parameter, lipoprotein external source parameter on the velocity and concentration have been examined with the help of the graphs. The present results have an important bearing on the therapeutic procedure of hyperthermia, particularly in understanding/regulating blood flow and lipid profile in the blood.

Keywords: Lipoprotein, Artery, Blood, Hematocrit, Mhd, Fluid and Flow.

Author α: Department of Mathematics & Statistics, Federal University Otuoke, Bayelsa State, Nigeria,
σ Department of Mathematics, Rivers State University, Port Harcourt, Nigeria

INTRODUCTION

The investigation of blood flow through arteries is considerably very important in many cardiovascular diseases. The poor circulation of blood in the body due to occlusion/blockage in arteries is one major health risks. Arteries channels oxygenated blood with nutrients from the heart to the tissues of the body, in the circulatory system of the human body. Blood is a viscous fluid circulating in the artery/vein. It has a strong nourishing effect on the human body and serves as one of the basic substances constituting the human body. Blood is a wonderful fluid which is an important factor of life.

Atherosclerosis is hardening of a blood vessel from a buildup of plaque as a result of excessive cholesterol (lipoprotein) intake. Plaque is made of fatty deposits, cholesterol, and calcium. Plaque buildup causes the artery to narrow and harden which is a serious risk human living.

Plaque buildup can slow and even stop blood flow. This means the tissue supplied by the artery is cut off from its blood supply and as such humans must watch the quantity of cholesterol they consume. It often leads to pain or decreased function. This condition can cause a number of serious health problems. Over the last two decades there has been theoretical and experimental studies of blood flow through the circulatory system of living mammals, has been the subject of scientific research and literatures available such as: characteristics of blood flow through an artery in the presence of multi-stenosis were studied by Chakravarty and Sannigrahi [1] the investigation of basic BFD flow problems attracts interest due to the numerous proposed applications in bioengineering and medical sciences.

Bio-fluids in the presence of a magnetic field with dissipation finds its applications in various upcoming fields like innovative drug targeting, surgical operations, etc. Haik *et al.* [2] reported a 30 percent decrease in blood flow rate when subjected to a high magnetic field of 10 T while Yadav *et al.* [3] found

a similar reduction in blood flow rate but at a much smaller magnetic field of 0.002 T. Sharma *et al.* [4] formulated a mathematical model for the hydro-magnetic bio-fluid flow in the porous medium with Joule effect. A theoretical analysis of blood flow and heat transfer in a permeable vessel in the presence of an external magnetic field was made by Sinha *et al.* [5]. Shit and Roy [6] investigated the effect of induced magnetic field on blood flow through a constricted channel, and demonstrated that increasing the values of the magnetic field reduces the velocity of the blood flow at the center. Rahbari *et al.* [7] carried out an analytical study on blood flow containing nanoparticles through porous blood vessels in the presence of the magnetic field using the Homotopy Perturbation Method (HPM). Blood flow in a large blood vessel has a profound influence on the efficiency of thermal therapy treatment. Electromagnetic heat, such as short waves and microwaves, sends heat up to 2 inches into the tissue and muscles. It works best for injuries in joints, muscles, and tendons. Moreover, hyperthermia treatment is found to be effective during cancer therapy in recent years. Its objective is to raise the temperature of pathological tissues above cytotoxic temperatures (41–450C) without overexposing healthy tissues [8]. Heat and mass transfer of blood flow considering its pulsatile hydro-magnetic rheological nature under the presence of viscous dissipation, Joule heating and a finite heat source was discussed by Sharma *et al.* [9]. Sinha and Shit [10] investigated the combined effects of thermal radiation and MHD heat transfer blood flow through a capillary. Thermal radiation effect on inclined arterial blood flow through a non-Darcian porous medium with magnetic field was discussed by Sharma *et al.* [11]. Bunonyo et al [12] investigated blood flow a stenosed artery with heat in the presence of magnetic field. In their investigation it is observed that magnetic field increase inhibit blood flow as a result of Lorentz force.

In spite of all these studies, the investigation of lipoprotein based MHD blood flow through a stenosed artery with haematocrit was given little attention. Hence, the main object of the present investigation is to study the importance of the haematocrit and external lipoprotein through human daily meals which prevents the body from producing cholesterol.

MATHEMATICAL FORMULATION

We consider a blood flow through an artery by assuming the artery to be a channel, and blood as an incompressible Newtonian fluid, viscous and electrically conducting. The viscous nature of blood is assumed to be due to the percentage of red blood and lipid. The lipoprotein is the protein in the blood which causes some impediment of the flow with an increase in concentration. The flow is caused by the pumping action of the heart. In addition, we assume u to be the velocity of the fluid, C_w & C_∞ as the concentration of lipoprotein at the wall and far field, D_0 as the molecular diffusivity, S is the external lipid source and H is the hematocrit. The governing equation for the flow of the fluid through an artery is stated as coupled partial differential equations as stated below.

$$\rho\frac{\partial u^*}{\partial t^*}=-\frac{\partial P^*}{\partial x^*}+\frac{\partial}{\partial y^*}\left(\mu^*(H)\frac{\partial u^*}{\partial y^*}\right)+\rho g\beta_C\left(C^*-C_\infty\right) \tag{1}$$

$$\frac{\partial C^*}{\partial t^*}=\frac{\partial}{\partial y^*}\left(D^*\frac{\partial C^*}{\partial y^*}\right)+S\left(C^*\right) \tag{2}$$

Subject to the corresponding boundary conditions are:

$$u^*=0\ ,\qquad C^*=C_\infty^* \qquad \text{at}\quad y=0 \tag{9}$$

$$u^*=0\ ,\qquad C^*=C_w^* \qquad \text{at}\quad y^*=R_0 \tag{10}$$

We assumed that the lipoprotein concentration dependent on the fluid viscosity, mass diffusion and external lipoprotein–C source respectively as:

$$\mu^* = \frac{\mu_0}{(1+2.5H)},\ S = Q\left(b_3\left(C^* - C_\infty\right)\right) \text{ and } D^* = D_0, \tag{5}$$

We consider the following dimensionless parameters:

$$\left.\begin{aligned} y = \frac{y^*}{R_0}, x = \frac{x^*}{R_0}, u = \frac{u^* R_0}{\upsilon}, t = \frac{\upsilon t^*}{R_0^2}, \mu = \frac{\mu^*}{\mu_0}, \phi = \frac{C^* - C_\infty}{C_w - C_\infty} \\ P = \frac{P^* R_0^2}{\rho \upsilon^2}, Gc = \frac{g R_0^3 \beta_C \left(C_w - C_\infty\right)}{\upsilon^2}, Sc = \frac{\upsilon}{D_0}, \upsilon = \frac{\mu_0}{\rho}, \lambda = \frac{Q b_3 R_0^2}{\upsilon} \end{aligned}\right\} \tag{6}$$

Transforming equation (1) and (2) using equation (6), we obtain the following:

$$(1+2.5H)\frac{\partial u}{\partial t} = -(1+2.5H)\frac{\partial P}{\partial x} + \frac{\partial^2 u}{\partial y^2} + Gc(1+2.5H)\phi \tag{7}$$

$$\frac{\partial \phi}{\partial t} = \frac{1}{Sc}\frac{\partial^2 \phi}{\partial y^2} + \lambda\phi \tag{8}$$

Subject to the corresponding boundary conditions are:

$$u = 0,\quad \phi = 0 \quad \text{at } y = 0 \tag{9}$$

$$u = 0,\quad \phi = 1 \quad \text{at } y = h \tag{10}$$

METHOD OF SOLUTION

In order solve equation (7) and equation (8) subject the boundary conditions in equation (9) – (10), we have to consider the solution in the following form:

$$\left.\begin{aligned} u = u_0 e^{i\omega t} \\ \phi = \phi_0 e^{i\omega t} \end{aligned}\right\} \tag{11}$$

We substitute equation (11) into equation (7) – (8), we obtain the following:

$$\frac{\partial^2 u_0}{\partial y^2} - (1+2.5H) i\omega u_0 = (1+2.5H) P_0 - Gc(1+2.5H)\phi_0 \tag{12}$$

$$\frac{\partial^2 \phi_0}{\partial y^2} + (\lambda - i\omega) Sc\,\phi_0 = 0 \tag{13}$$

Subject to the corresponding boundary conditions are:

$$u_0 = 0,\quad \phi_0 = 0 \quad \text{at } y = 0 \tag{14}$$

$$u_0 = 0,\quad \phi_0 = e^{-i\omega t} \quad \text{at } y = h \tag{15}$$

Let $\chi_1 = (1+2.5H) i\omega$, $\chi_2 = (\lambda - i\omega) Sc$, $P = (1+2.5H) P_0$ and $G_1 = Gc(1+2.5H)$ so that equation (12) to (13) can be transformed to:

$$\frac{\partial^2 u_0}{\partial y^2} - \chi_1 u_0 = P - G_1 \phi_0 \tag{16}$$

$$\frac{\partial^2 \phi_0}{\partial y^2} + \chi_2 \phi_0 = 0 \tag{17}$$

Equation (16) and (17) are ordinary differential equations, we have to solve them subject to the boundary conditions in equation (14) – (15).
Solving equation (17) which has the general solutions as:

$$\phi_0(y) = Asin\sqrt{\chi_2}y + Bcos\sqrt{\chi_2}y \tag{18}$$

We determine the coefficients in equation (18) using the boundary conditions in equation (14) and (15) as:

$$A = \frac{e^{-i\omega t}}{sin\sqrt{\chi_2}h}, B = 0 \tag{19}$$

Substitute the values in equation (19) into equation (18), we obtain the following:

$$\phi_0(y) = \left(\frac{e^{-i\omega t}}{sin\sqrt{\chi_2}h}\right) sin\sqrt{\chi_2}y \tag{20}$$

Now, substitute equation (20) into equation (11), we obtain the following:

$$\phi(y) = \left(\frac{sin\sqrt{\chi_2}y}{sin\sqrt{\chi_2}h}\right) \tag{21}$$

To solve the non-homogenous ordinary differential equation, we substitute equation (21) into equation (16) as follows:

$$\frac{\partial^2 u_0}{\partial y^2} - \chi_1 u_0 = P - G_1\left(\frac{e^{-i\omega t}}{sin\sqrt{\chi_2}h}\right) sin\sqrt{\chi_2}y \tag{22}$$

Solving for equation (22), we have to first obtain the complementary before the particular solution. So, the homogenous solution takes the general form:

$$u_{0c}(y) = A_1 sinh\sqrt{\chi_1}y + B_1 cosh\sqrt{\chi_1}y \tag{23}$$

The particular solution takes the form:

$$u_{0p}(y) = A_3 + A_4 sin\sqrt{\chi_2}y + B_4 cos\sqrt{\chi_2}y \tag{24}$$

Differentiate according to the order of the differential equation (22), we obtain:

$$A_4 = \left(\frac{G_1 e^{-i\omega t}}{(\chi_2 + \chi_1) sin\sqrt{\chi_2}h}\right), B_4 = 0, A_3 = -\frac{P}{\chi_1} \tag{25}$$

Substituting the values in equation (25) into equation (24), we obtain the following:

$$u_{0p}(y) = -\frac{P}{\chi_1} + \left(\frac{G_1 e^{-i\omega t}}{(\chi_2 + \chi_1) sin\sqrt{\chi_2}h}\right) sin\sqrt{\chi_2}y \tag{26}$$

The general solution to the momentum equation (22), we have the following:

$$u_0(y) = A_1 sinh\sqrt{\chi_1}y + B_1 cosh\sqrt{\chi_1}y - \frac{P}{\chi_1} + \left(\frac{G_1 e^{-i\omega t}}{(\chi_2 + \chi_1) sin\sqrt{\chi_2}h}\right) sin\sqrt{\chi_2}y \tag{27}$$

We can solve for the constant coefficients in (27) using the boundary condition in equations (14) and (15), we obtain the following:

$$A_1 = \left[\frac{P}{\chi_1} - \left(\frac{P}{\chi_1}\right)\frac{cosh\sqrt{\chi_1}h}{sinh\sqrt{\chi_1}h} - \left(\frac{G_1 e^{-i\omega t}}{(\chi_2 + \chi_1) sin\sqrt{\chi_2}h}\right)\frac{sin\sqrt{\chi_2}h}{sinh\sqrt{\chi_1}h}\right], B_1 = \frac{P}{\chi_1} \tag{28}$$

Then the general solution for the velocity profile is:

$$u(y)=\left[\begin{array}{l}\left[\frac{P}{\chi_1}\left(1-\frac{\cosh\sqrt{\chi_1}h}{\sinh\sqrt{\chi_1}h}\right)-\left(\frac{G_1e^{-i\omega t}}{(\chi_2+\chi_1)\sinh\sqrt{\chi_1}h}\right)\right]\sinh\sqrt{\chi_1}y \\ +\left(\frac{P}{\chi_1}\right)\left(\cosh\sqrt{\chi_1}y-1\right)+\left(\frac{G_1e^{-i\omega t}}{(\chi_2+\chi_1)\sin\sqrt{\chi_2}h}\right)\sin\sqrt{\chi_2}y\end{array}\right]e^{i\omega t} \quad (29)$$

RESULTS PRESENTATION

In this section, numerical simulation is carried out for equation (21) and (29) using the following parameter values to investigate the effect of haematocrit, oscillatory parameter, mass lipoprotein source parameter and Schmidt number on the velocity and concentration functions respectively. We considered variable parameters such as: $H=3$, $Gc=10$, $Sc=0.22$, $\omega=2$ and $t=1$. The graphical results presented as follows:

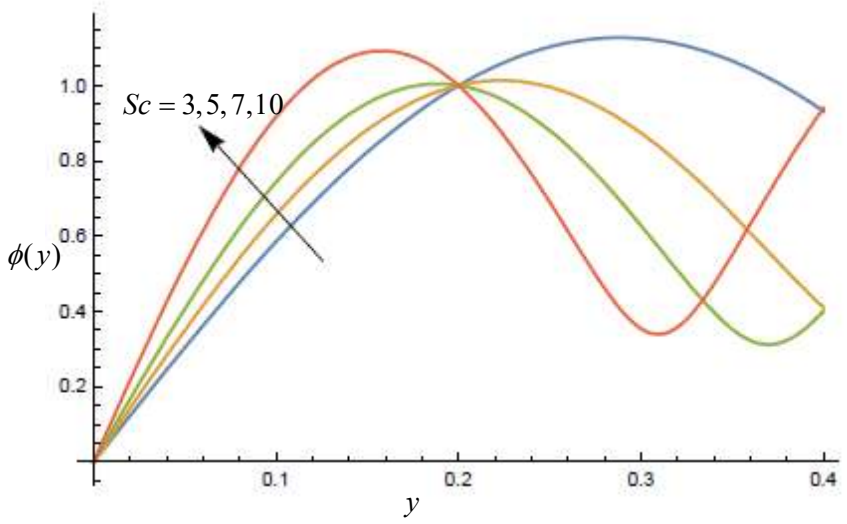

Fig 1 influence of Sc on concentration profile

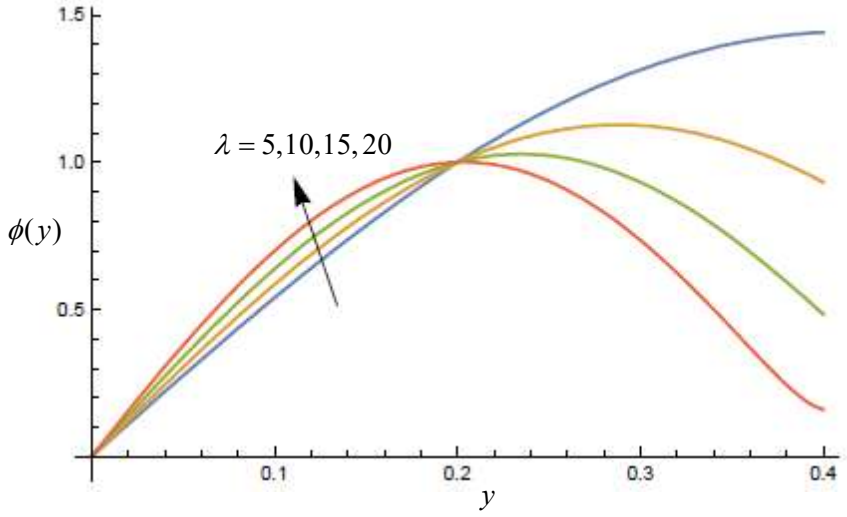

Fig 2 influence of λ on concentration profile

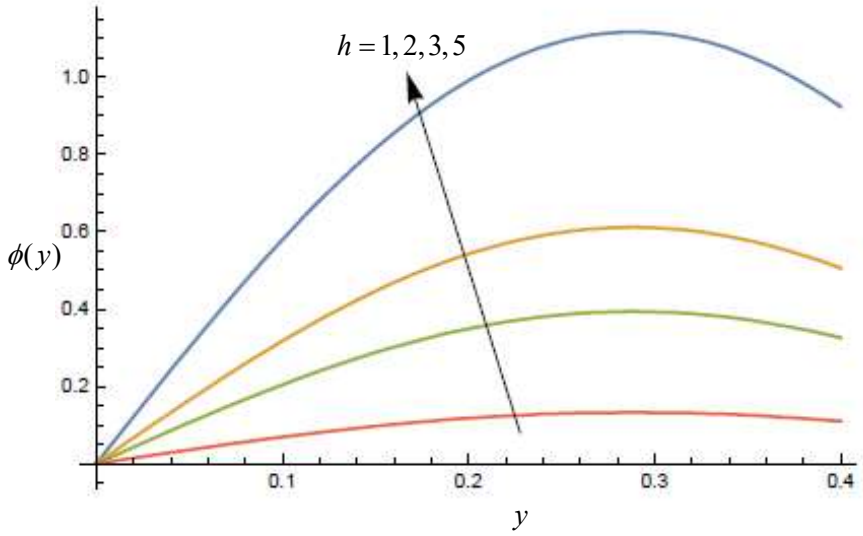

Fig 3 influence of h on concentration profile

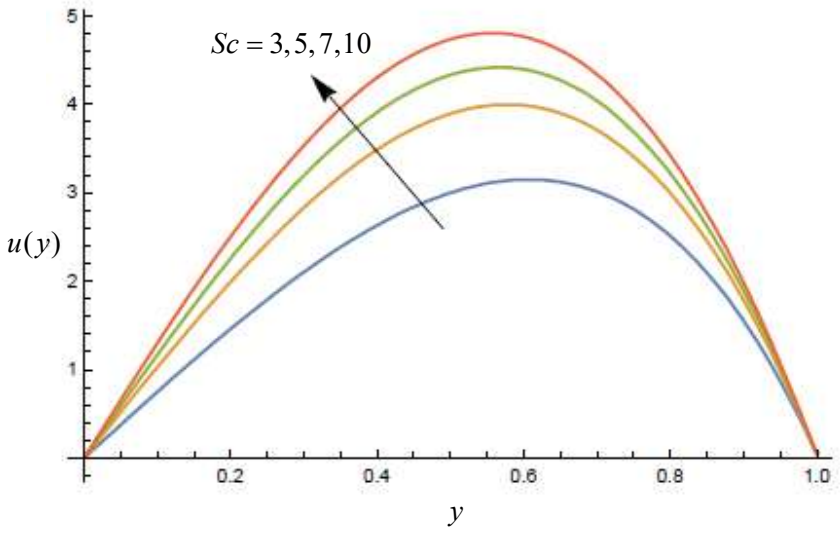

Fig 4 influence of Sc on concentration profile

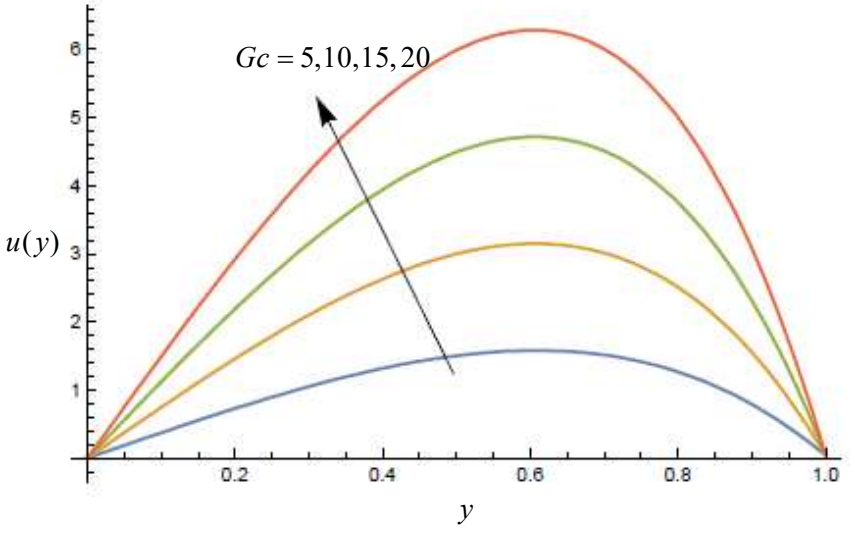

Fig 5 influence of Gc on velocity profile

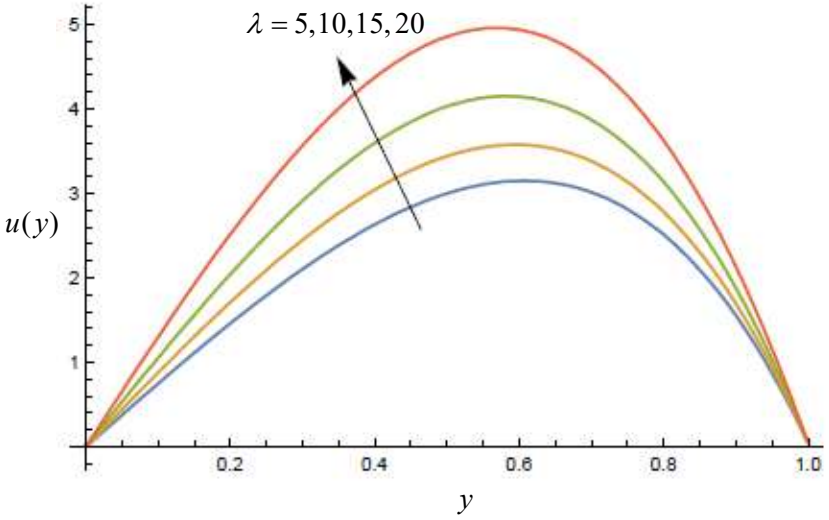

Fig 6 influence of λ on velocity profile

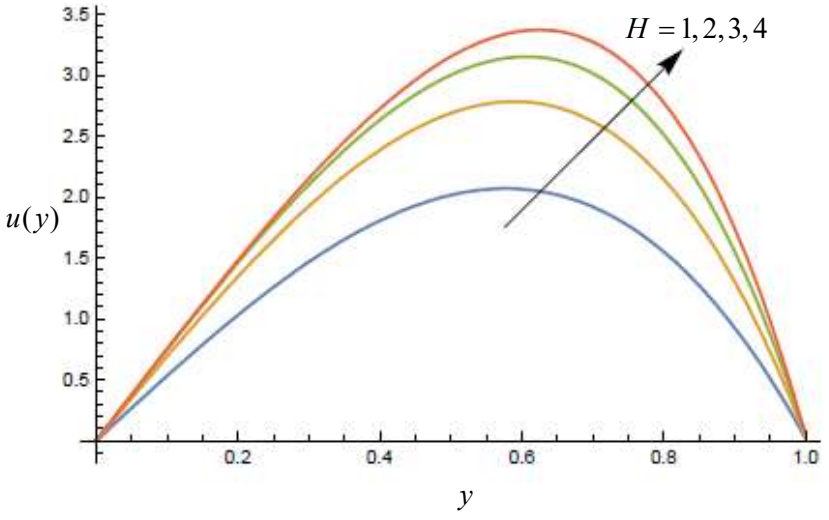

Fig 7 influence of H on velocity profile

DISCUSSION

The Schmidt number clearly influenced the concentration profile as can seen in **Fig 1**. This however converged at a point for different values of Schmidt number increase before the concentration profile diverged.

As we can see in **Fig 2**, the increasing level of lipoprotein from a source can actually increase the level of the concentration profile on the downstream as indicated in the figure. However, we observed some level of divergence in concentration profile as the boundary layer is increased.

Fig 3 illustrates the influence of the height of stenosis on concentration profile through an artery while other valuable parameters are kept as the same. We noticed that as h increased from 1 to 4 units, there is a corresponding increase in flow concentration profile. It clearly seen that $R > R_0$ which is a reduction in stenosis.

In **Fig 4** we noticed an increase in velocity profile as the value of the Schmidt number increases from 0.22 to 0.9. It clear shows that the porosity remained constant while the dynamic viscosity of the fluid is improved. However, the flow attained different peaks for different values of the Schmidt number before decelerating to zero, which is an indication that for us to maintain some level of flow is have to consider the dynamic viscosity of the fluid as it relates to the molecular diffusivity.

Fig 5 depicts a clear case of an improved flow as the concentration Grashof number is increased from 5 to 20. This researched result is of the opinion that the concentration difference between the wall and that of the far field is greater that dynamic viscosity of the fluid can actually improve the flow field due

Often times high level of cholesterol actually increase the viscosity of the fluid because it adds to the protein level in the blood plasma fluid thereby causing some sought of slow movement of the fluid towards the downstream and causing the heart rate to increase as seen in **Fig 6.** But as indicated in the figure, we can say that flow gets a peak for different values of λ before decelerating to zero in an unimaginable fashion.

Haematocrit as earlier stated is the percentage of red blood cells in the blood volume, which means it has quite a substantial amount of hemoglobin in the bloodstream. However, we noticed in **Fig 7** that as the haematocrit level is increased from 1 to 4 through a supplement there is increase in the general blood flow but different level of H results to decrease in due to an increased viscosity.

CONCLUSION

In this paper, investigation of lipoprotein based MHD fluid flow through an arterial channel with haematocrit is analyzed. The conclusions of the present analysis are as follows:

1. The velocity profile was raised for the increasing values of Solutal Grashof number, Schmidt number.
2. An increase in Schmidt number increases the concentration profile
3. With increasing values of the hematocrit initially increased the velocity to a peak before it decelerated to zero.
4. Lipoprotein source parameter also influences the flow profile to increase to a peak before decelerating to zero as clearly seen.

REFERENCES

1. Chakravarty S. and Sannigrahi A. (1999): *A nonlinear mathematical model of blood flow in a constricted artery experiencing body acceleration*. – Math. Comput. Model, vol.29, pp.9-25.
2. Haik Y., Pai V. and Chen C.-J. (2001): *Apparent viscosity of human blood in a high static magnetic field*. –J. Magn. Magn. Mater., vol.225, No.1–2, pp.180-186.
3. Yadav R.P., Harminder S. and Bhoopal S. (2008): *Experimental studies on blood flow in stenosis arteries in presence of magnetic field*. – Ultra Sci., vol.20, No.3, pp.499-504.
4. Sharma B.K., Mishra A. and Gupta S. (2013): *Heat and mass transfer in magneto-biofluid flow through a non- Darcian porous medium with Joule effect*. – J. Eng. Phys. and Thermo Phy., vol.86, No.4, pp.716-725.
5. Sinha A., Mishra J.C. and Shit G.C. (2016): *Effect of heat transfer on unsteady MHD flow of blood in a permeable vessel in the presence of non-uniform heat source*. – Alexandria Engineering Journal, vol.55, No.3, pp.2023-2033.
6. Shit G.C. and Roy M. (2016): *Effect of induced magnetic field on blood flow through a constricted channel. An analytical approach*. – Journal of Mechanics in Medicine and Biology, vol.16, No.03, pp.1650030.
7. Rahbari A., Fakour M., Hamzeh Nejad A., Vakilabadi M.A. and Ganji D.D. (2017): Heat transfer and fluid flow of blood with nanoparticles through porous vessels in a magnetic field: A quasi-one dimensional analytical approach. – Mathematical Biosciences, vol.283, pp.38-47.
8. Levin W., Sherar M.D., Cooper B., Hill R.P., Hunt J.W. and Liu F.-F. (1994): Effect of vascular occlusion on tumour temperatures during superficial hyperthermia. – International Journal of Hyperthermia, vol.10, No.4, pp.495-505.
9. Sharma B.K., Sharma M., Gaur R.K. and Mishra A. (2015): Mathematical modeling of magneto pulsatile blood flow through a porous medium with a heat source. – International Journal of Applied Mechanics and Engineering, vol.20, No.2, pp.385-396.
10. Sinha A. and Shit G.C. (2015): Electromagnetohydrodynamic flow of blood and heat transfer in a capillary with thermal radiation. –Journal of Magnetism and Magnetic Materials, vol.378, pp.143-151.
11. Sharma B.K., Sharma M. and Gaur R.K. (2015): Thermal radiation effect on inclined arterial blood flow through a non-Darcian porous medium with magnetic field. – Proceeding: First Thermal and Fluids Engineering Summer Conference, ASTFE Digital Library, vol.17, pp.2159-2168, DOI: 10.1615/TFESC1.bio.013147.
12. Bunonyo, K. W., Israel-Cookey, C., & Amos, E. (2018). Modeling of Blood Flow through Stenosed Artery with Heat in the Presence of Magnetic Field. *Asian Research Journal of Mathematics*, 1-14.